



HAL
open science

Crystal growth physics in dry snow metamorphism : characterisation and modeling of kinetic effects

Rémi Granger

► **To cite this version:**

Rémi Granger. Crystal growth physics in dry snow metamorphism : characterisation and modeling of kinetic effects. Glaciology. Université Grenoble Alpes, 2019. English. NNT : 2019GREAI072 . tel-03092266

HAL Id: tel-03092266

<https://theses.hal.science/tel-03092266>

Submitted on 2 Jan 2021

HAL is a multi-disciplinary open access archive for the deposit and dissemination of scientific research documents, whether they are published or not. The documents may come from teaching and research institutions in France or abroad, or from public or private research centers.

L'archive ouverte pluridisciplinaire **HAL**, est destinée au dépôt et à la diffusion de documents scientifiques de niveau recherche, publiés ou non, émanant des établissements d'enseignement et de recherche français ou étrangers, des laboratoires publics ou privés.

THÈSE

Pour obtenir le grade de

DOCTEUR DE LA COMMUNAUTE UNIVERSITE GRENOBLE ALPES

Spécialité: **2MGE: Matériaux, Mécanique, Génie civil,
Electrochimie**

Arrêté ministériel: 25 mai 2016

Présentée par

Rémi GRANGER

Thèse dirigée par **Christian GEINDREAU, Professeur UGA**, et
codirigée par **Frédéric FLIN, CR MTES, Météo-France**

préparée au sein du **Laboratoire Sols, Solides, Structures et
Risques** et du **CNRM/Centre d'Études de la Neige**
dans l'**École Doctorale I-MEP2 – Ingénierie – Matériaux,
Mécanique, Environnement, Énergétique, Procédés,
Production**

**Physique de la croissance cristalline pour
les métamorphoses de neige sèche:
caractérisation et modélisation des effets
cinétiques**

**Crystal growth physics in dry snow
metamorphism: characterisation and
modeling of kinetics effects**

Thèse soutenue publiquement le **17 décembre 2019**,
devant le jury composé de:

Monsieur Luc SALVO

Professeur, Grenoble INP, Président

Monsieur Ian BAKER

Professeur, Thayer School of Engineering, Dartmouth College, USA,
Rapporteur

Monsieur Etsuro YOKOYAMA

Professeur, Computer Center, Gakushuin University, Japan, Rapporteur

Monsieur Wolfgang LUDWIG

Directeur de Recherche, INSA Lyon, Examineur

Monsieur Christian GEINDREAU

Professeur, Université Grenoble Alpes, Directeur de thèse

Monsieur Frédéric FLIN

Chargé de Recherche, CNRM/CEN, Co-Directeur de thèse



Résumé

L'objectif principal de la thèse est d'améliorer la compréhension des phénomènes de facettage observables lors des métamorphoses de la neige sèche. La thèse se concentre sur les couplages entre la cinétique de croissance cristalline et la diffusion de la vapeur et de la chaleur. Pour la première fois, la tomographie par contraste de diffraction (DCT) a été utilisée pour suivre l'évolution d'un échantillon de neige sous gradient de température contrôlé. La technique permet de mesurer l'orientation cristalline des grains constituant la microstructure de l'échantillon. Les relations entre l'orientation cristalline et les échanges de matière ont été analysés. L'étude montre que les différences de cinétique entre les faces basales et prismatiques des cristaux de glace influencent les flux de matière à l'interface air/glace. Sur le plan de la simulation numérique, une forte anisotropie du coefficient cinétique a été prise en compte dans l'évolution de l'interface air/glace. Le modèle développé utilise la méthode du champ de phase et couple le changement de phase à la diffusion de la vapeur et de la chaleur. Le modèle a été comparé d'une part à une expérience de migration d'une cavité d'air dans un monocristal de glace sous gradient de température, observée par microtomographie à rayons X et d'autre part, à la croissance d'un cristal négatif de glace lors d'une expérience de pompage suivie par microscopie optique. L'anisotropie prise en compte permet de reproduire le facettage observé. Enfin, le potentiel du modèle numérique proposé pour décrire les métamorphoses de la neige est mis en évidence.

Mots-clé: Neige, métamorphoses, croissance cristalline, coefficient cinétique, orientation cristalline, champs de phase, tomographie RX, DCT

Abstract

The main objective of the thesis is to improve our understanding of faceting occurring during dry snow metamorphism. The thesis focuses on the interplay between heat and mass diffusion, and kinetic effects in the context of snow. For the first time, Diffraction Contrast Tomography has been performed to monitor an experiment of temperature gradient metamorphism. The technique permits us retrieval of the crystalline orientation of the grains constituting the microstructure of the sample. Links between orientation of crystals and mass fluxes were analysed. The study shows that kinetic differences between basal and prismatic faces have effects on phase change fluxes at the ice/air interface. From a numerical modeling point of view, a highly anisotropic kinetic coefficient has been taken into account for the evolution of the ice/air interface. The model uses the phase-field approach and couples phase changes to heat and water vapor diffusion. The model was compared to an experiment of air cavity migration under a temperature gradient in a monocrystalline ice block monitored with X-ray microtomography, and to the growth of a negative crystal during a pumping experiment followed with optical microscopy. Such anisotropy permits us reproduction of the observed faceting. Finally, the potential of the proposed model to describe snow metamorphism is highlighted.

Keywords: Snow, metamorphism, crystal growth, kinetic coefficient, phase-field, crystalline orientation, X-rays tomography, DCT

Contents

1	Physics of snow metamorphism	3
1	Generalities	3
2	Physics of dry snow metamorphism - grains scale/layer scale	8
2.1	Water vapor at saturation: the controlling quantity	8
2.2	Weak gradient metamorphism	10
2.3	Temperature gradient metamorphism	12
2.4	Control factors and conditions	14
2.5	Concluding remarks	15
3	Ice physics - molecular scale	15
3.1	Generalities on crystal growth	16
3.2	Surface states	19
3.3	Measurements of kinetic coefficients	21
3.4	Surface tension anisotropy	22
3.5	Links with snow metamorphisms	22
3.6	Concluding remarks	24
4	Main objective of the thesis	25
5	Experimental techniques	26
6	Microstructural Modeling	27
6.1	Motivations and problem	27
6.2	Phase-field modeling	29
7	Structure of the manuscript	35
2	Orientation selective grain activity in snow under temperature gradient metamorphism observed with Diffraction Contrast Tomography	37
2.1	Introduction	37
2.2	Methods	39

2.2.1	Sample and sample environnement	39
2.2.2	Diffraction Contrast Tomography: Experimental Setup	40
2.2.3	Data processing	43
2.3	Results	43
2.3.1	Images time series	43
2.3.2	Density	46
2.3.3	Specific Surface Area	47
2.3.4	Orientation tensor	47
2.3.5	Pore size distribution	50
2.3.6	Relation between flux and grain orientation	50
2.3.7	Example of evolution inside a small subvolume	55
2.4	Discussion	56
2.4.1	Fluxes and dependence on orientation	56
2.4.2	Independence on orientation for deposition	57
2.4.3	Uncertainties due to processing	57
2.4.4	Representativity	58
2.5	Conclusions	58
3	Kinetic faceting with phase-field model for snow metamorphism: validation on air cavity migration experiment.	63
3.1	Introduction	63
3.2	Phase-field model	66
3.2.1	Isotropic model	66
3.2.2	Anisotropic kinetic coefficient	70
3.3	Experiment	72
3.4	Simulations	78
3.4.1	Isotropic model	78
3.4.2	Anisotropic model	82
3.5	Discussion	84
3.5.1	Kinetic coefficient values	84
3.5.2	Computational cost	85
3.6	Conclusion	86
4	Adjusting phase-field simulations to an experiment of negative crystal growth at -10°C	89
4.1	Introduction	89
4.2	Model summary	91
4.3	Case of a simple ice/air system: negative crystal growth	95
4.3.1	Experiment	95
4.3.2	Simulation	99
4.4	Discussion	103
4.5	Conclusion	106

5	Towards modeling of temperature gradient metamorphism	109
5.1	2D axisymmetric simulation of temperature gradient metamorphism of a grain	109
5.1.1	Method	109
5.1.2	Results	110
5.1.3	Concluding remarks	112
5.2	3D simulation of anisotropy	114
5.2.1	Method	114
5.2.2	Results	116
5.2.3	Discussion	116
5.2.4	Concluding remarks	118
5.3	Conclusion	118
6	Conclusion and perspectives	119
6.1	Experiment of temperature gradient metamorphism observed with Diffraction Contrast Tomography	119
6.2	Modeling of kinetic faceting	120
	Bibliography	127



General Introduction

Snow on the ground is a porous medium made of air containing water vapor, ice and eventually liquid water. From the time of its deposition, it never stops evolving due to the action of processes generically called *snow metamorphism*. As a result, different shapes may be created in the microstructure, which correspond to different types of snow with really different physical properties. Being able to predict the evolution of these properties is important for many societal issues like snow avalanche risk management, weather forecasting or climatic projections. Thus, a good understanding of snow metamorphism is required.

Particularly, faceted grains may appear in the microstructure at a sufficiently high temperature gradient. The appearance and development of these facets can critically affect the snow properties, particularly the mechanical behavior. The facets are directly linked to the crystalline nature of ice, and result from the growth of ice crystals. Formation of these facets has been studied both experimentally and theoretically. At the macroscopic scale several controlling quantities have been identified. The most important are the temperature gradient and the density. However, descriptions of the growth conditions of these facets remains inaccurate. At the ice/air interface scale, it is understood that these facets correspond to the expression of the *attachment kinetics*, the mechanisms by which new molecules are incorporated into a crystal. However, the conditions for this expression and the implications of the kinetic effects are poorly understood.

In the present work, we measured crystalline orientation in an in-situ experiment, using, for the first times the technique of Diffraction Contrast Tomography to monitor temperature gradient metamorphism of snow. This permits the correlation of the local evolution of the microstructure to the underlying crystalline lattice. The results particularly highlight the effects of kinetics in snow metamorphism. Selective activity of the crystals depending on their orientation is observed.

Additionally, modeling crystal growth for snow metamorphism directly from kinetics laws would permit the application of theoretical answers to these questions, but currently this kind of model does not exist. In consequence, we present a phase-field model for snow metamorphism that, for the first time, takes into account strong kinetic anisotropy. We show that this model reproduces faceting consistently with experiments on snow metamorphism.

Physics of snow metamorphism

The first section of this chapter is intended to give a broad picture of snow physics, both in the sky and on the ground, its implications in the Earth system, and the main societal issues. It describes the interest in studying snow.

The focus of the present thesis is introduced and described in more details in section 2. The current knowledge on snow metamorphism, and particularly temperature gradient metamorphism is presented. The importance of crystal growth physics of ice in its understanding is highlighted. Section 3 introduces the most important knowledge of ice physics that is required for the understanding of the present work. Section 4 presents objective of the thesis.

Finally, sections 5 and 6 review respectively experimental and numerical techniques to characterize and model snow metamorphism.

1 Generalities

Snowflakes are ice crystals formed in clouds by deposition of water vapor and/or liquid droplets. When they fall on the ground and accumulate, they form the snowpack. The result consists of a layered porous geomaterial made of ice, air containing water vapor and possibly liquid water if its temperature is close to 0 °C.

Snowpack interacts with various part of the environmental system. As it constitutes a good thermal insulator, since it traps air in the pores and has high albedo, its presence plays an important role in ground-atmosphere interactions. Additionally, it has particular effects on hydrological systems, as it can act as a reservoir of water.

Both snowflakes and snow on the ground come in a large variety of types, differing by the shapes of the crystals. First evidence of this variety was shown by the photographer Wilson Bentley who was fascinated by the beauty and variety of snowflakes [*Bentley and Humphries, 1931*]. Later, Nakaya thoroughly experimented on the growth conditions of snowflakes and discovered that the temperature and

the water supersaturation are the most important factors for shape determination [Nakaya, 1954]. The supersaturation is a measure of the water vapor content of the air. It is defined as the difference between the water vapor density and the water vapor density at saturation. His findings are summarized by the Nakaya’s diagram (Figure 1.1). Later still, Kobayashi [1961] and Magono and Lee [1966] elaborated on these observations.

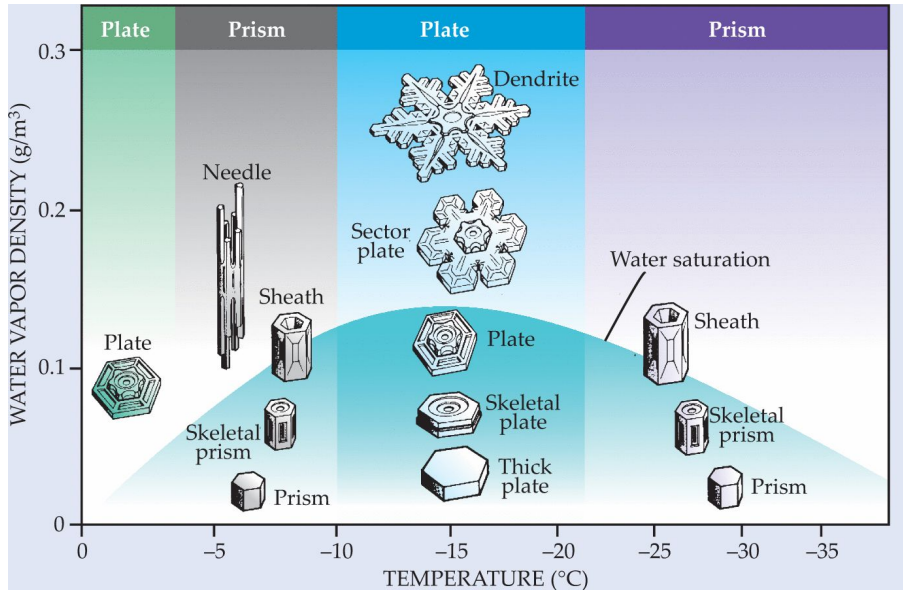


Figure 1.1: Morphological dependence of snowflakes on temperature and water vapor density. From Furukawa and Wettlaufer [2007]

Snowflakes are found to be of two main types: plates or columns. Plates are snowflakes which extend along one dimension much less than in the two other dimensions. On the contrary, columns are crystals which extend along one dimension much more than the two other dimensions. Plates grow specifically in the temperature ranges $[0\text{ }^{\circ}\text{C to }-4\text{ }^{\circ}\text{C}]$ and $[-10\text{ }^{\circ}\text{C to }-22\text{ }^{\circ}\text{C}]$. Columns grow specifically in the range $[-4\text{ }^{\circ}\text{C, }-10\text{ }^{\circ}\text{C}]$. Below $-22\text{ }^{\circ}\text{C}$, disparities exist in the literature: some authors report that crystals are only of the columns types [Kobayashi, 1961; Furukawa and Wettlaufer, 2007; Furukawa, 2015], while some others mention both columns and plates [Nakaya, 1955; Magono and Lee, 1966; Libbrecht, 2005, 2017]. The detailed crystal shape depends on the supersaturation. When supersaturation is low, crystals formed are fully dense, with flat faces. When increasing supersaturation, the crystals become more and more hollow, and, if the supersaturation is very high, and the growth rapid, dendritic structures occur, leading to the classically known shape of star-like snowflakes with six branches. These empirical relationships are partly understood. The six-fold symmetry is always present in all crystals. This is due to the crystalline structure of ice which is hexagonal at atmosphere pressure and in this range of temperatures (Ice Ih, see e.g. Choukroun and Grasset [2007]). Faces of an ice crystal are then of two types: basal or prismatic (figure 1.2). The crystallographic

axes are the c-axis, normal to the basal plane, and the a-axis, in the basal plane. The principal features are explained considering kinetics, the processes by which water molecules are integrated in the crystalline lattice. More detailed overview of the involved phenomena are presented in section 3.

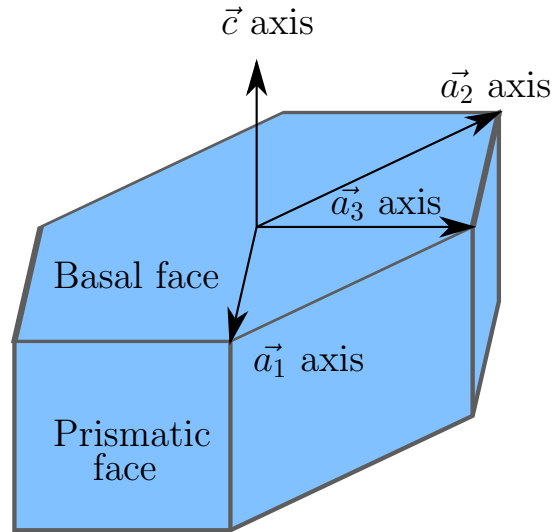
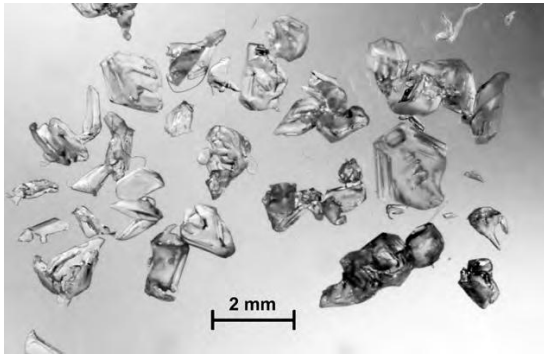


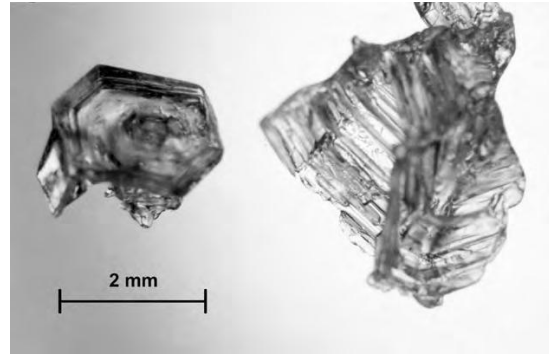
Figure 1.2: Nomenclature for the faces and axes of the hexagonal crystalline structure of ice.

On the ground, snow can also be observed in diverse shapes (see e.g. *Seligman* [1936]). Those types are described by the International Classification for Seasonal Snow on the Ground (ICSG, *Fierz et al.* [2009] and are directly linked to meteorological history of the snow [*Colbeck*, 1982]. Fresh snows or precipitation particles (PP) refers to snow that has not evolved since its fall, and correspond to an assembly of snowflakes as presented previously. Decomposing and fragmented particles (DF), refers to snow that has just been slightly crushed mechanically, by wind for example, or has evolved slightly so that the initial type of snowflakes can be recognized. The morphology inside a snowlayer will depend on the humidity and temperature conditions it meets, as this defines the type of metamorphism. When snow contains liquid water, wet snow metamorphism occurs leading to large (of the order of 1 mm or more), well-rounded grains called melt forms (MF). When the snow is dry, snow will evolve according to one of two dry snow metamorphisms: weak gradient metamorphism or temperature gradient metamorphism.

As indicated by their name, the macroscopic temperature gradient is the main quantity which drives the evolution of dry snow. In a snowpack, the temperature at the bottom is generally $0\text{ }^\circ\text{C}$ as it is due to the heat flux coming from earth and surface temperature is fixed by interactions with the atmosphere. The temperature gradient is then given by the surface temperature, conductivity and thickness of snow layers constituting the snowpack. When the macroscopic temperature gradient is low typically under $5\text{ }^\circ\text{C m}^{-1}$, fresh snow or precipitation particles are small



(a) faceted crystals



(b) Depth hoar crystals

Figure 1.3: Examples of crystals obtain by temperature gradient metamorphism. The characteristic feature is the flat faces observable on thoses crystals. Taken from *Fierz et al.* [2009].

(about 0.1 mm) and well rounded, referred as rounded grains (RG). The associated mechanism is called weak-gradient, isothermal, or curvature-driven metamorphism. When temperature gradient is stronger than $5\text{ }^{\circ}\text{C m}^{-1}$, the microstructure shows grains with facets, called faceted crystals (see Figure 1.3a). The morphology of these grains recalls those of snowflakes, with the possibility of observing both hexagonal plates or columns. Globally, under the strongest gradients, larger than $20\text{ }^{\circ}\text{C m}^{-1}$, so-called depth hoar (DH) appears. These grains are also faceted and typically have a pyramidal cup shape, with the open part towards the warmer side of the snow, while the other side is rounded (see Figure 1.3b). Faceting following the 6-fold symmetry of the depth-hoar and faceted crystals is a characteristic of temperature gradient metamorphism. A summary of the relations between the different types of snow metamorphism and snow types is illustrated in Figure 1.4. More detailed descriptions of the different types of snow metamorphism are given in section 2.

The properties of a snow layer depends on the type of snow. In particular, the mechanical behavior differs greatly from one type to another. Fresh snow is in general pulverulent, with low density. If accumulation is significant on high slopes, it can create powder snow avalanches. Those avalanches consists of a fluid made up of air and snow particles in suspension, which flow downslope at high speeds. Rounded grains sinter quickly and in general constitute cohesive layers. Faceted crystals and depth hoar crystals are in general really poorly cohesive with low shear stress resistance. Typically, those grains constitute weak layers that play an important role in slab avalanches mechanisms, which require a cohesive layer overtopping a weak layer.

Forecasting snowpack properties has many interests for the human society as it represents a water ressource, an economic ressource thanks to ski tourism but also a natural hazard both for infrastructure and people because of avalanches. In that perspective, snowpack models like CROCUS [*Brun et al.*, 1992, 1989; *Vionnet*

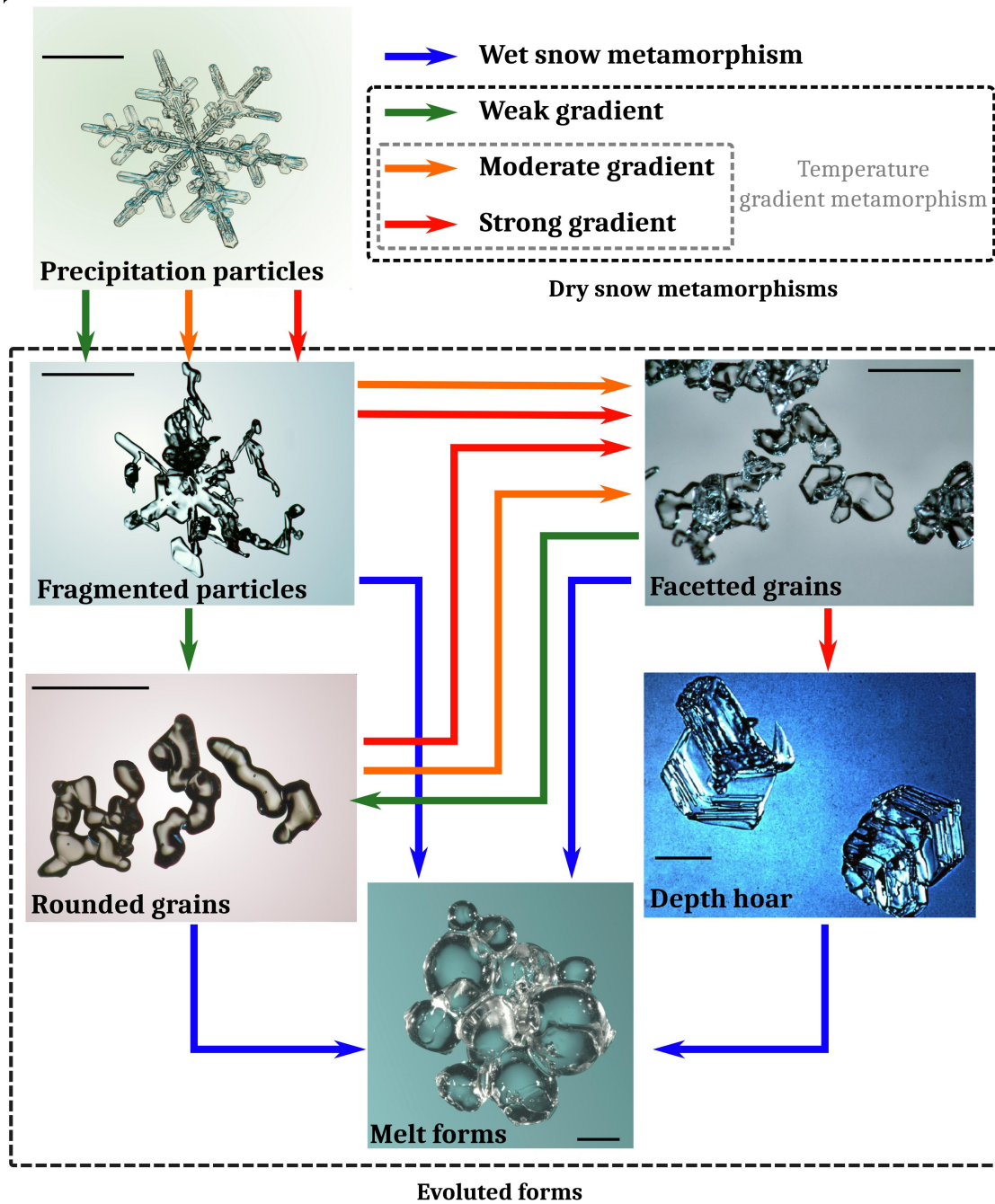


Figure 1.4: Summary scheme of relations between the different kinds of metamorphism and snow types in a snowpack. Horizontal black scale bar is 1 mm in length on all images.

et al., 2012] or SNOWPACK [Lehning *et al.*, 2002b; Bartelt and Lehning, 2002; Lehning *et al.*, 2002a, 2006] have been developed to predict the evolution of layers and properties, like mechanical, optical or microstructural. To do so, all those models rely on the prediction of the snow type, and so on an accurate understanding of metamorphism. A summary of the current knowledge on dry snow metamorphism is presented in the next section.

2 Physics of dry snow metamorphism - grains scale/layer scale

In that thesis, we will focus on the dry snow metamorphism, particularly on the origin and impact of faceting of the microstructure. For that reason, current description of dry snow metamorphism is presented in that section. We do not consider wet snow metamorphism.

2.1 Water vapor at saturation: the controlling quantity

In the absence of liquid water, mass transfers through the vapor phase. The prevailing phase changes are thus sublimation and deposition. At a given point of the interface, the local growth and decay is then described by the Hertz-Knudsen equation [Libbrecht, 2005]

$$v_n = \alpha v_{kin} \sigma(T, K) \quad (1.1)$$

where σ is the local supersaturation, depending on the temperature T and the mean curvature K of the interface at that point. v_{kin} is a function of the kinematic velocity of water vapor molecules due to thermal agitation. v_n is the normal velocity of the interface with the normal directed from the solid phase to the air phase. α is the condensation coefficient, this coefficient represents the efficiency of the physical mechanisms, named *attachment kinetics*, by which vapor molecules are integrated into the crystalline lattice of the solid phase. By definition, $\alpha \leq 1$, with equality when all molecules hitting the surface are integrated into it. This coefficient is a simple parametrisation at the grain scale of the underlying attachment kinetics mechanisms at the interface scale. A major focus will be brought to that coefficient in section 3 as those mechanisms are responsible for the appearance of facets on crystals [Libbrecht, 2005]. v_{kin} and σ are expressed as

$$v_{kin} = \frac{\rho_{vs}(T, K)}{\rho_i} \sqrt{\frac{k_B T}{2\pi m}} \quad (1.2)$$

$$\sigma(T, K) = \frac{\rho_v - \rho_{vs}(T, K)}{\rho_{vs}(T, K)} \quad (1.3)$$

where m is the mass of a water molecule, k_B is the Boltzmann constant, ρ_i is the density of ice (917 kg m^{-3} at $-10 \text{ }^\circ\text{C}$), ρ_v is the local water vapor density, $\rho_{vs}(T, K)$ is the water vapor density at saturation. The Hertz-Knudsen relation (1.1) can sometimes be found in terms of kinetic coefficient β :

$$v_n = \beta \sigma \quad (1.4)$$

which thus defines $\beta = \alpha v_{kin}$. However, this definition may differ in the literature. This is the convention taken e.g. by *Yokoyama and Kuroda* [1990], but sometimes the name kinetic coefficient refers to the quantity $1/\alpha v_{kin}$, that is to say the reciprocal

(e.g. *Kaempfer and Plapp* [2009]). For the rest of this work, we choose to call kinetic coefficient the parameter β as defined by equation (1.4) and reciprocal kinetic coefficient the quantity $\mu = \frac{1}{\beta} = \frac{1}{\alpha v_{kin}}$. When $\sigma > 0$, the air is said to be *oversaturated* and the excess of water vapor then deposits ($v_n > 0$). When $\sigma < 0$, the air is said to be *undersaturated* and the ice sublimates ($v_n < 0$).

The Clausius-Clapeyron equation gives the expression $\rho_{vs}(T, K = 0)$ for the water vapor density at saturation over a flat surface:

$$\rho_{vs}(T, K = 0) = \rho_{vs}^{ref}(T^{ref}) \exp \left[\frac{Lm}{\rho_i k_B T} \left(\frac{T}{T^{ref}} - 1 \right) \right] \quad (1.5)$$

Taking into account the Gibbs-Thomson relation:

$$\frac{\rho_{vs}(T, K)}{\rho_{vs}(T, K = 0)} = e^{d_0 K} \quad (1.6)$$

we have

$$\rho_{vs}(T, K) = \rho_{vs}^{ref}(T^{ref}) \exp \left[\frac{Lm}{\rho_i k_B T} \left(\frac{T}{T^{ref}} - 1 \right) \right] e^{d_0 K} \quad (1.7)$$

where L is the latent heat of sublimation of ice, d_0 is the capillary length, and ρ_{vs}^{ref} is a reference value of water vapor density at saturation at the reference temperature T^{ref} . d_0 can be evaluated to be $1.3 \cdot 10^{-9}$ m [*Kaempfer and Plapp*, 2009] and the curvature of snow grains is typically of the order of 10^4 m $^{-1}$. Thus, $d_0 K \approx 10^{-5} \ll 1$. Thus, the exponential term of (1.6) can be linearized. Leading to the final expression:

$$\rho_{vs}(T, K) = \rho_{vs}^{ref}(T^{ref}) \exp \left[\frac{Lm}{\rho_i k_B T} \left(\frac{T}{T^{ref}} - 1 \right) \right] (1 + d_0 K) \quad (1.8)$$

A summary of notations and the corresponding values of physical parameters can be found in table 1.1.

In the context of dry snow metamorphism mass transfers occur via the gas phase, i.e. by advection and/or diffusion. Advection/convection mechanisms may actually occur in some specific cases [*Calonne et al.*, 2014b]. However, they are not considered in that thesis. Considering diffusion only, the water vapor diffuses along gradients of ρ_v . Because T and K are, in the general case, not uniform, ρ_{vs} varies spatially. On the one hand, at each point of the interface, the thermodynamics of the interface tends to reach the equilibrium with the ambient vapor phase, and so tends to reach $\rho_v = \rho_{vs}(T, K)$ following (1.1). on the other hand, diffusion will tend to homogenize the vapor density. As a result, the water vapor flows from high to low values of $\rho_{vs}(T, K)$ and the actual water vapor density field is determined by the balance between attachment kinetics and diffusion.

The transfer of vapor is thus driven by the variability of T and K over the ice/air interface. Basically, the type of metamorphism will then depend on which of those two parameters is predominant.

When temperature gradients are macroscopically low, differences of T are small and the variations of water vapor density at saturation follow almost uniquely the

Table 1.1: Notation and typical values of the physical parameters involved in dry snow metamorphism.

Symbol	Description	Values	References
α	Condensation coefficient	$[10^{-3}, 1]$	[<i>Libbrecht, 2006</i>]
β	Kinetic coefficient	10^{-4} to 10^{-7}	[<i>Kaempfer and Plapp, 2009</i>]
Γ	Ice air interface		
κ_a	Thermal conductivity of air	$2 \times 10^{-2} \text{ Wm}^{-1}\text{K}^{-1}$	[<i>Kaempfer and Plapp, 2009</i>]
κ_i	Thermal conductivity of ice	$2.29 \text{ Wm}^{-1}\text{K}^{-1}$	[<i>Kaempfer and Plapp, 2009</i>]
Ω_a	Air domain		
Ω_i	Ice domain		
μ	Reciprocal kinetic coefficient	10^5	
ρ_i	Density of ice	917 kg m^{-3}	
ρ_v	Water vapor density		
ρ_{vs}	Water vapor density at saturation	10^{-3} to $10^{-2} \text{ kg m}^{-3}$	[<i>Kaempfer and Plapp, 2009</i>]
ρ_{vs}^{ref}	water vapor density at saturation at reference temperature T^{ref}	$4.85 \times 10^{-3} \text{ kg m}^{-3}$	
σ	Dimensionless supersaturation		
C_a	Heat capacity of air	$1.4 \times 10^{-3} \text{ Jm}^{-3}\text{K}^{-1}$	[<i>Kaempfer and Plapp, 2009</i>]
C_i	Heat capacity of ice	$1.8 \times 10^{-6} \text{ Jm}^{-3}\text{K}^{-1}$	[<i>Kaempfer and Plapp, 2009</i>]
d_0	Capillary length	$1.3 \times 10^{-9} \text{ m}$	[<i>Kaempfer and Plapp, 2009</i>]
D_v	Diffusion coefficient of water vapor in air		
k_B	Boltzmann's constant	$1.38 \times 10^{-23} \text{ J K}^{-1}$	
K	Mean curvature	10^{-4} to 10^{-4} m^{-1}	
L	Latent heat of sublimation of ice per volume	$2.60 \times 10^9 \text{ J m}^{-3}$	[<i>Kaempfer and Plapp, 2009</i>]
m	Mass of a water molecule	$2.99 \times 10^{-26} \text{ kg}$	
T^{ref}	Reference temperature (triple point)	273.16 K	
v_n	Normal interface velocity	$\sim 10^{-9} \text{ m s}^{-1}$	

variations of K : this is weak gradient metamorphism. For increasing temperature gradient, the variations of ρ_{vs} are first affected by both local variations of K and T , when they are similar. They finally reach a regime where the variations of ρ_{vs} follow almost uniquely the variations of T : this is temperature gradient metamorphism.

2.2 Weak gradient metamorphism

Basically, without a significant temperature gradient (typically $\lesssim 5 \text{ }^\circ\text{Cm}^{-1}$), evolution of snow can be seen as a sintering process. That is, for grains in contact with each others, mass is transferred to the contact points, forming bonds and increasing the cohesion of the structure. Several processes of mass transport to the bonds have

appeared to be relevant for ice. The most important are: diffusion through the vapor phase, with evaporation/condensation at the interface [Hobbs and Mason, 1964], surface diffusion [Kingery, 1960], lattice diffusion [Kuroiwa, 1961], and boundary diffusion [Maeno and Ebinuma, 1983]. Most of the experiments on ice sintering treat the problem by modeling the problem of two ice spheres in contact for an assumed process. From this, a power law of time can be deduced for the evolution of the grains and bond radius. The exponent appears to be dependent on the considered process, so comparison with experiment would, in principle, enable identification of the predominant one. Although the problem may appear to be simple by its geometry, the experiments remain complex with many uncertainties and knowing which process dominates remains an open question. (see e.g. Blackford [2007] for a review). However, it appears that diffusion, with evaporation/condensation is predominant [Hobbs and Mason, 1964; Maeno and Ebinuma, 1983; Blackford, 2007]. For this reason, the other processes would not be considered in this thesis and only the vapour diffusion process will be considered and modeled to describe snow metamorphism.

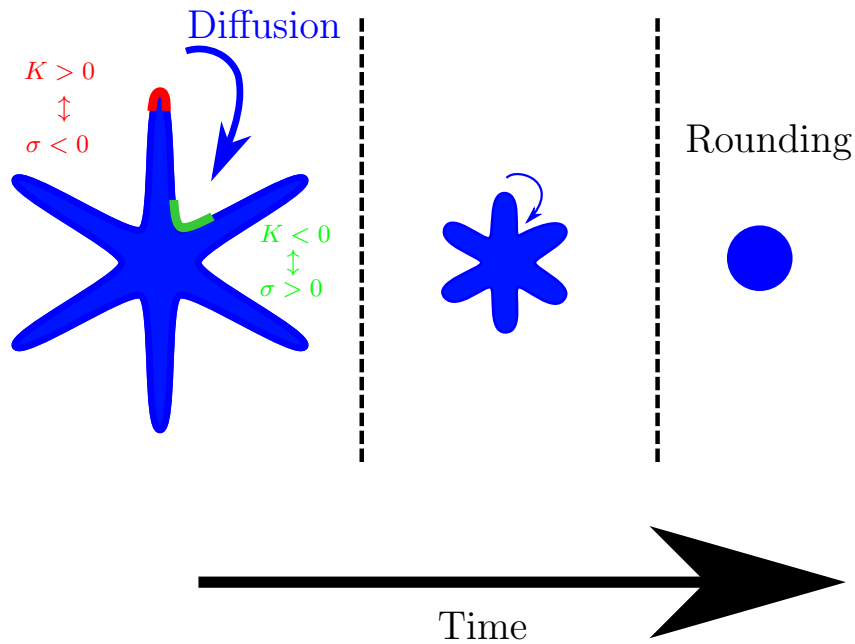


Figure 1.5: Representation of the Kelvin effect. The ice sublimates from convex areas and vapor deposit in concavities, resulting in a rounding of the shapes.

From equation (1.8) high values of ρ_{vs} correspond to high mean curvature, i.e. strong convexities, while low values correspond to concavities (negative mean curvature). Air is then undersaturated close to the convexities, which then sublimate. This creates a source of water vapor that diffuses through the pore space and then condensates at concavities as the air is oversaturated in their vicinity.

Considering for example, a precipitation particle, as illustrated in Figure 1.5, in which, mass is transferred from the apexes of the branches to their bases. And those transfers stop when curvature is homogeneous over the surface, i.e. when the crystal is well rounded. That effect is named the *Kelvin effect* and explains why weak gradient metamorphism leads to rounded grains. In addition, this tends to consolidate necks between grains and, thus, creates a well sintered microstructure.

With rounding, the Specific Surface Area (SSA), the area per unit mass of snow decreases [Flin *et al.*, 2003, 2004]. Legagneux *et al.* [2004] and Legagneux and Domine [2005] have shown that this decrease is well fitted by a logarithmic law, which is well interpreted by an Ostwald ripening process with mean-field diffusive interactions between ideally-spherical particle. Here, diffusion with evaporation/condensation is assumed to be the dominant process with the rate limited by diffusion. Ostwald ripening can then be interpreted thermodynamically as an evolution by minimisation of the surface energy. Flin *et al.* [2003] described weak gradient metamorphism by a mean-field approach, but by assuming evaporation/condensation as the rate limiting step. They applied the resulting model to real 3D microstructure geometries obtained from x-ray tomography, and showed that can be used to explain the observed evolution. Similarly, Kaempfer and Schneebeli [2007] observed a decrease of the SSA and an increase of density and trabecular thickness. Their data were well interpreted by a sintering processes. However, sublimation-condensation was not systematically the only process during sintering. Instead, boundary diffusion was also expected to occur.

2.3 Temperature gradient metamorphism

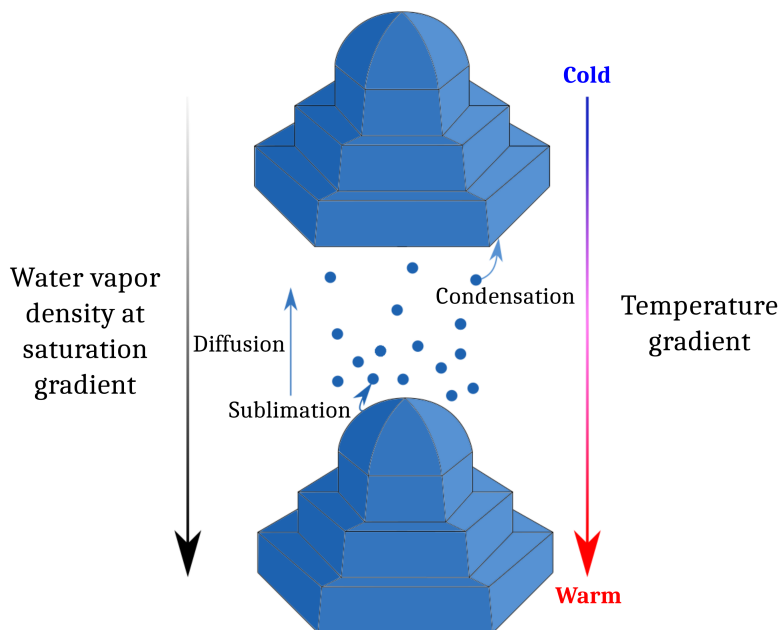


Figure 1.6: Scheme of principle of temperature gradient metamorphism.

If the temperature gradient applied over a snow layer is sufficiently large ($\gtrsim 5 \text{ }^\circ\text{C m}^{-1}$), the local variations of ρ_{vs} mainly follow local variations of T . Thus, warmer regions of interfaces are undersaturated and sublimate producing a source of water vapor that diffuses across the pore to finally condense at colder regions that are oversaturated.

Consider two grains separated by a pore like on Figure 1.6 and impose a vertical temperature gradient over it with the warm side on the bottom. The top surface of the bottom grain is then warmer than the bottom surface of the top grain. In consequence, the water vapor flows from the bottom to the top. This is the hand-to-hand delivery process so called by *Yosida et al.* [1955]. This deposition at the bottom while sublimation at the top leads to complete recrystallization and an apparent migration toward the bottom of the ice structure. *Pinzer et al.* [2012] used X-ray tomography to follow the formation of depth hoar in snow with density in the range 250 kg m^{-3} - 312 kg m^{-3} under $50 \text{ }^\circ\text{C m}^{-1}$ at $-15 \text{ }^\circ\text{C}$ and showed that the grains actually recrystallize completely after 2-3 days of metamorphism. Under a temperature gradient, variations of ρ_{vs} are more important than in weak gradient conditions.

Let us evaluate the order of magnitude of the variations of ρ_{vs} for i) typical variations due to curvature differences and ii) typical variations due to temperature. Let us consider two points A and B on interfaces of the same pore, separated by 0.5 mm, which is the order of magnitude of the pore size in snow. Let K^A and K^B be the curvature at A and B, respectively, and T^A and T^B be the temperature at A and B, respectively, with $\rho_{vs}^A = \rho_{vs}(T^A, K^A)$ and $\rho_{vs}^B = \rho_{vs}(T^B, K^B)$.

- First, let $T^A = T^B = -10 \text{ }^\circ\text{C}$, $K^A = -K^B = 5 \times 10^4 \text{ m}^{-1}$, which are the order of magnitude of the temperature and extremal values of curvatures found for example by *Flin et al.* [2004] in fresh snow samples. Then, the thermodynamic disequilibrium can be measured by $\frac{\rho_{vs}^A - \rho_{vs}^B}{\rho_{vs}(-10 \text{ }^\circ\text{C}, 0)} = 1 \times 10^{-2} \%$.
- Second, let $T^A = -9.97 \text{ }^\circ\text{C}$ and $T^B = -10.03 \text{ }^\circ\text{C}$ and $K^A = K^B = 0$, which corresponds to a temperature gradient of $60 \text{ }^\circ\text{C m}^{-1}$, which is a rather small local gradient due to gradient amplification [*De Quervain*, 1973], and flat facets so that curvature effects are not considered. Then, we have $\frac{\rho_{vs}^A - \rho_{vs}^B}{\rho_{vs}(-10 \text{ }^\circ\text{C}, 0)} = 1.1 \times 10^{-1} \%$

Thus, local thermodynamic disequilibria could be more important under a temperature gradient, and, thus, faceted crystals appear. They are the signature of kinetic growth, and, thus, are also called "kinetic forms" [*Colbeck*, 1983a] in opposition to equilibrium forms that refer to rounded grains.

The attachment kinetics are important in the growth dynamics of snow crystals, There are a wide variety of processes, which depend directly on the state of the crystals surfaces. A more detailed description of these processes is out of the scope

of this section but will be presented in section 3 as the principal objective of this work is to develop an understanding on the growth of kinetic forms.

2.4 Control factors and conditions

The previously presented processes are asymptotic cases of evolution. As explained, they result from the major dominance of some processes over others. But in practice, all intermediates combinations of the presented processes are, of course, possible. In addition, the complex microstructure of a snow layer is so that these different processes can act simultaneously on different parts of the microstructure, leading to different grain types in the snow. Macroscopic snowpack models, like Crocus or Snowpack, include metamorphism laws for the evolution, and, thus, require a good understanding of the transition between the different kind of metamorphism at the layer scale. While the physical processes are rather well understood at the grain scale, the control factors and conditions are still poorly understood.

It is relatively clear that the temperature gradient and density drive the type of metamorphism. Authors report a temperature gradient transition from weak gradient metamorphism to faceted grains in the range $5\text{ }^{\circ}\text{Cm}^{-1}$ - $15\text{ }^{\circ}\text{Cm}^{-1}$ [Armstrong, 1981; Colbeck, 1983a; Sommerfeld, 1983; Flin and Brzoska, 2008] with the transition temperature gradient increasing with increasing snow density. The transition from faceted crystals to depth hoar was studied by Akitaya [1974] and Marbouty [1980] who found a value of about $25\text{ }^{\circ}\text{C m}^{-1}$ for 200 and 320 kg m^{-3} , respectively with fine grains of snow, with again a higher transition temperature gradient for denser snow.

Akitaya [1974] also found that at high density, and high temperature gradient, a really cohesive type of depth hoar may form, called hard depth hoar. Here he reports a temperature gradient for transition decreasing with increasing density. Typically conditions were a temperature gradient about $40\text{ }^{\circ}\text{C m}^{-1}$ or higher for a density of 400 kg m^{-3} or higher. Pfeffer and Mrugala [2002] found that hard depth hoar consists of faceted crystals joined by necks, forming at a temperature gradient of $20\text{ }^{\circ}\text{Cm}^{-1}$ and higher, for a density of 400 kg m^{-3} and higher, with elongation in the vertical direction forming chains. Chains of depth hoar crystals are also observed to form in low-density snow under large temperature gradients [Staron *et al.*, 2014]. In that case the resulting microstructure is really fragile and the effective thermal conductivity is highly anisotropic.

In all those studies, it was observed that the bigger faceted crystals, and, in particular depth hoar, were found in a large air space or low density snow. They concluded that faceted grain growth requires an air space to occur. Those experimental observations are reinforced by the theoretical work of Colbeck [1983a]. Marbouty [1980] and Akitaya [1974] observed that the shapes of depth hoar crystals follow the crystal habits of Nakaya's diagram for snowflakes growing in the atmosphere with striated hexagonal cups from $-2\text{ }^{\circ}\text{C}$ to $-5\text{ }^{\circ}\text{C}$ and from $-10\text{ }^{\circ}\text{C}$ to $-25\text{ }^{\circ}\text{C}$ and column-like crystals between $-6\text{ }^{\circ}\text{C}$ and $-10\text{ }^{\circ}\text{C}$.

However, this classical vision classifying metamorphism based on the temperature gradient amplitude seems imperfect. *Pinzer and Schneebeli* [2009] conducted experiments of metamorphism under alternating temperature gradient. This led to rounded grains, even with temperature gradient as large as $100\text{ }^{\circ}\text{C m}^{-1}$ and snow densities as low as 127 kg m^{-3} . Thus, it seems that the stability of temperature gradient also plays a role in the picture. In contrast, faceted grains have been reported to grow under weak temperature gradients of 3 Km^{-1} [*Brzoska et al.*, 2007; *Flin and Brzoska*, 2008]. *Colbeck* [1985] and *Arons and Colbeck* [1995] observed growth of single faceted crystals under weak temperature gradient for temperatures below $-11\text{ }^{\circ}\text{C}$.

2.5 Concluding remarks

In summary, the density (pore size), the temperature gradient, and the temperature are the quantities that most affect dry snow metamorphism. However, currently, the onset transitions between the different regimes are poorly defined. The classical vision is that transition between the different snow types occurs at given temperature gradient that depends on the density and the temperature. Basically, the transition from rounded grains to faceted crystals is known to occur in the range $10 - 20\text{ }^{\circ}\text{C m}^{-1}$, and the transition from faceted crystals to depth hoar in the range $20 - 25\text{ }^{\circ}\text{C m}^{-1}$. However these transitions suffer from large uncertainties and are not well understood due to the really high complexity of snow microstructural geometry. Moreover, recent experiments do not match to this picture. Specific forms of depth hoar exist. Hard depth hoar, which are cohesive depth hoar crystals, form in high density snow ($\approx 350\text{ kg m}^{-3}$ and higher) with a high temperature gradient ($\approx 20\text{ }^{\circ}\text{C m}^{-1}$ and higher). Chains of depth hoar, which are really fragile, form at low density and a high temperature gradient.

Part of this uncertainty can be attached to the high degree of complexity of the microstructure. Indeed, as the temperature gradient increases, interactions between two growing crystals become more and more local and heterogeneous. This requires a large set of morphological parameters to more accurately characterize the conditions.

Additionally, the transitions are assigned to the onsets of some kinetics effects. However, as it will be explained, those processes are various and complex and their impact on snow metamorphism is unclear. Thus, in addition to the geometrical complexity, answers to these uncertainties may lay in ice crystal growth physics.

3 Ice physics - molecular scale

As explained, in dry snow metamorphism, a broad picture of transition between rounded and faceted crystals is known, principally seen as a critical temperature gradient amplitude. However the exact criterion remains unclear. What triggers faceting? What controls the transition between faceted crystals and depth hoar? Further, why do striations appear on depth hoar?

As mentioned previously, these transitions are expected to be due to the onset of some kinetic effects. Thus, in the quest to understand in a finer manner those transitions, it is necessary to understand which mechanisms are indeed involved and when they can be predominant and expressed at the grain scale.

This section aims at introducing notions of crystal growth and attachment kinetics, particularly for ice. We will present current understandings in the link with dry metamorphism of snow.

3.1 Generalities on crystal growth

Crystals are a periodic assembly of atoms or molecules, like in the case of ice, bounded together by any kind of bonds, ranging from covalent to Van Der Waals.

In snow, the crystal surface is the limit between the crystal domain, where molecules are well arranged and the pore space, where vapor molecules move freely in the 3D space. At each instant, some molecules at the interface escape from the interaction potential created by the lattice due to thermal agitation and join the water vapor phase. At the same time, some molecules from the water vapor phase hit the surface and are trapped in its potential, i.e. are integrated in the crystals. When those fluxes of matter are equal, the surface is said to be at thermodynamic equilibrium, otherwise the crystal is growing (deposition) or decaying (sublimation).

Thus, the crystal growth is highly dependent of the interaction potential at the surface, which is created by the individual contributions of each molecule close to the surface: the growth is highly dependent on the arrangement of molecules at the interface, i.e. on the surface state.

Thus the bondings between surface molecules and vapor molecules rule attachment kinetics. A general way of thinking about such bonding effects is with the Terrace Step Kink (TSK) model. This model was introduced by *Kossel* [1927] and *Stranski* [1928]. The molecules are represented by unit cubes, and the crystal is a packing of those cubes, bonded together by their 6 faces. The surface of the crystal, is composed typically of flat surfaces called terraces, separated by steps of one molecule high in which some kinks may be present (see Figure 1.7). When molecules are adsorbed on the surface, they are called admolecules. Since the strength of a bonding of a molecule to the crystal increases with the number of its neighbors, bonds in kink sites are stronger than step sites and these step sites are themselves stronger than terrace sites. When a molecule is adsorbed on the surface, it creates a step, where another molecule can more easily attach. Similarly, when a molecule integrates a step, it creates a kink and new molecules attach easily. By successive attachments, kinks can propagate along steps and steps propagate on surfaces.

3.1.1 Growth of a singular face

2D Nucleation Let us consider an ideally totally flat surface without any defects nor steps. The adsorption of at least one molecule is necessary for growth of a

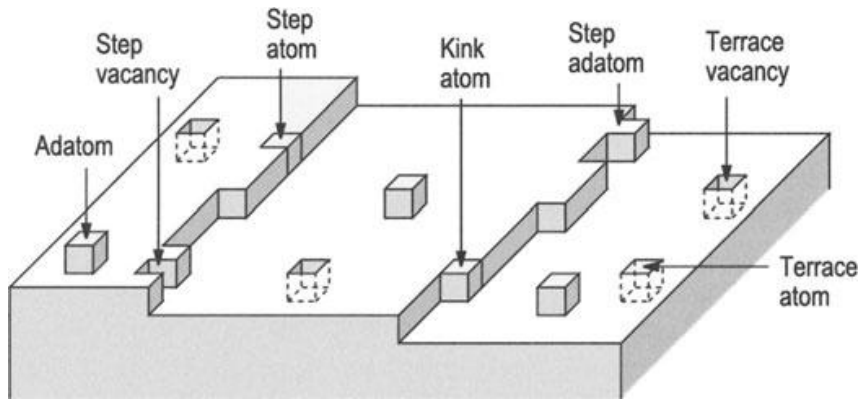


Figure 1.7: Idealized crystal surface following Terrace-Surface-Kink (TSK) model. From *Oura et al.* [2003]

crystal layer. However, propagation from a single molecule is pretty unlikely as it can sublime really easily. Instead, growth under that conditions would require nucleation of an adsorbed cluster, comprising several adatoms as represented in Figure 1.8. The nucleation of such adsorbed islands requires high supersaturations in order to be sufficiently probable. Modeling of such mechanism leads to a condensation coefficient of the form [Libbrecht, 2005]

$$\alpha \approx A(T) \exp\left(-\frac{\sigma_{crit}}{\sigma}\right) \quad (1.9)$$

where A accounts principally for step velocity and σ_{crit} is a critical supersaturation. For $\sigma < \sigma_{crit}$, contribution to crystal growth due to that mechanism is really small as almost no clusters are formed. Thus, this mechanism introduced a threshold on σ for growth.

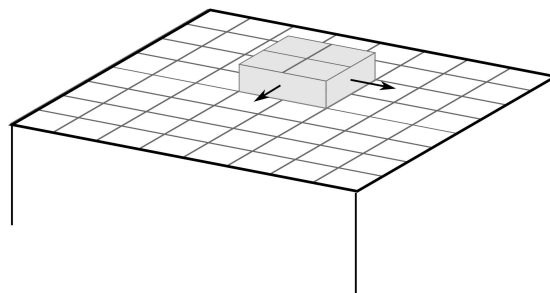


Figure 1.8: Representation of 2D nucleation growth mechanism. Under sufficiently high supersaturations, molecules may be adsorbed in islands (in grey) over the crystal surface. Then the steps can propagate forming a new crystal layer.

Growth from defects Under that critical threshold, nucleation can be aided by various defects at the surface like impurities or dislocations which play the role of step generators. This idea was introduced and formalised by *Burton et al.* [1951] who gave a thorough mathematical treatment of this process which has then be

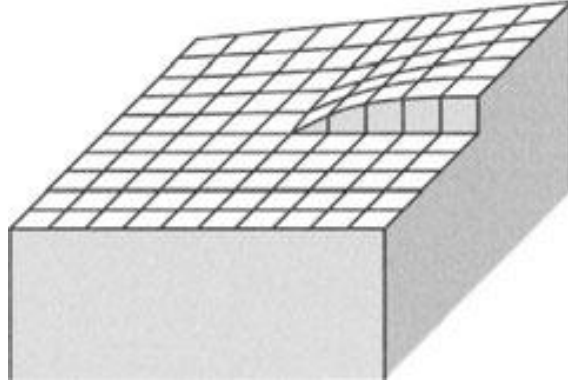


Figure 1.9: Representation of a screw dislocation. From *Oura et al.* [2003]

called the BCF theory. Screw dislocations are a step source that propagates in a helicoidal manner, with new layers created at each turn (figure 1.9). Thus screw dislocations can represent a really efficient nucleation site which can dominate at low supersaturation on flat faces. BCF theory predicts two regimes of screw dislocation depending on the ratio between diffusion length of admolecules along the step and the length of one spiral turn. In practice, the relevant regime of growth of snow crystals is for small diffusion length of admolecules, leading to a parabolic relation between growth rate and supersaturation [Libbrecht, 2005]:

$$v_n \sim \sigma^2 \Leftrightarrow \alpha \sim \sigma \quad (1.10)$$

3.1.2 Growth of vicinal faces, kinetic anisotropy

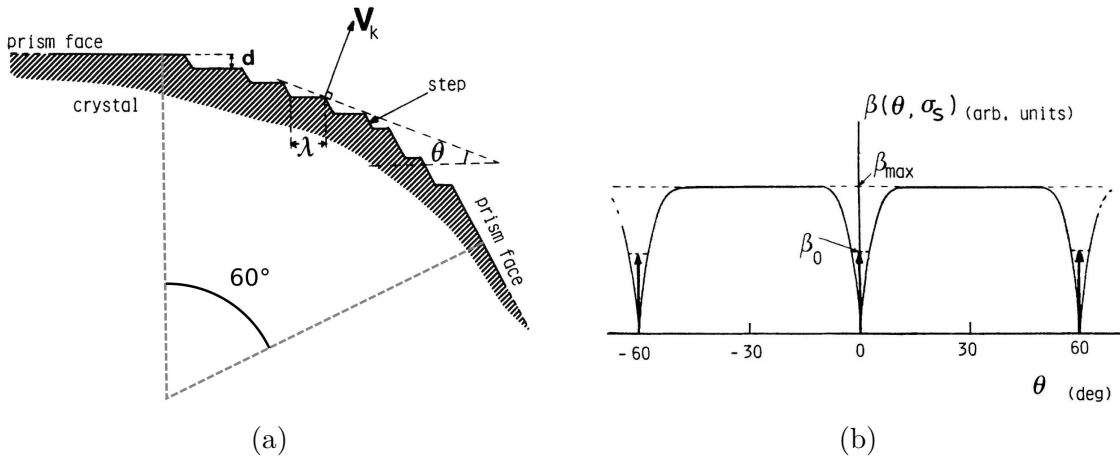


Figure 1.10: Relationship between the face orientation relative to singular orientation and step density (a) and resulting kinetic coefficient anisotropy as a function of orientation (b). The solid line corresponds to no growth of singular faces. Modified from *Yokoyama and Kuroda* [1990]

Now let us consider the so-called vicinal faces, which are high index faces whose orientation are given by the average plane through a set of steps and terraces, as represented in Figure 1.10a. Let λ be the length of terrace and d be the height of the steps. The steps density is higher when $\frac{d}{\lambda} \rightarrow 1$. And, if assuming as a first approximation a perfect singular face, with no defects, without considering 2D nucleation, the velocity of the singular face would be 0. It can be shown [Chernov, 1974; Yokoyama and Kuroda, 1990], that the kinetic coefficient will be of the form:

$$\beta(s) = \beta_{max} \frac{s}{s_1} \tanh\left(\frac{s_1}{s}\right) \quad (1.11)$$

where $s = \tan \theta = \frac{d}{\lambda}$, and s_1 is a parameter depending on the diffusion of adsorbed molecules. The kinetic coefficient then is highly anisotropic, with a sharp minimum in the singular direction while it will be less affected by the orientation in other directions (see Figure 1.10b, solid line). Now, if we consider any process of growth of the singular faces, step sources from (screw) dislocations or 2D nucleation presented before, it would modify the minimum. Typically for $d \ll \lambda$, the step density due to a screw dislocation will be much greater than the one due to the slightly inclined vicinal faces. So for small θ , i) β will be independent of the orientation and ii) will be nonzero, noted β_0 on Figure 1.10b. In that case, as explained in section 3.1.1, the kinetic coefficient at $\theta = 0$ is temperature and/or supersaturation dependent as dictated by the growth mechanism of singular face.

3.2 Surface states

Temperature roughening At low temperatures, thermal agitation is weak and surfaces are regular, with surface molecules aligned in a plane, thus forming a smooth surface. But as the temperature increases, the thermal agitation may break that regularity and the surface becomes molecularly rough.

This transition is called temperature roughening. This process may be of importance for kinetics as a vapor molecule hitting such a rough surface is really likely to bond with any molecule standing out of the surface. Thus, a condensation coefficient of $\alpha \approx 1$ is expected on rough surfaces. Particularly, it would then have no link between growth and underlying crystalline structure. Thus kinetic faceting would not occur with rough surfaces. However, details of the transition are not well known. Usually, it is seen as a first order transition occurring at a given temperature called roughening temperature [Burton *et al.*, 1951; Chernov, 1993]. Colbeck [1985] observed a transition in the equilibrium forms of single snow crystals from fully-rounded particles to disk-like plates at -2 °C and then to hexagonal plates at -10 °C. Later, Elbaum [1991] measured a roughening transition for ice and observed no roughening on basal faces and a transition temperature of -2 °C for prismatic faces, which is consistent with Colbeck's observation in that the basal faces are less subject to temperature-dependent roughening, but not in temperature. Recent studies [Libbrecht and Rickerby, 2013; Libbrecht, 2017] corroborate the idea that

basal faces are not subjected to temperature roughening and that prismatic faces are indeed affected in the temperature range between $-10\text{ }^{\circ}\text{C}$ and $0\text{ }^{\circ}\text{C}$, without a sharp transition.

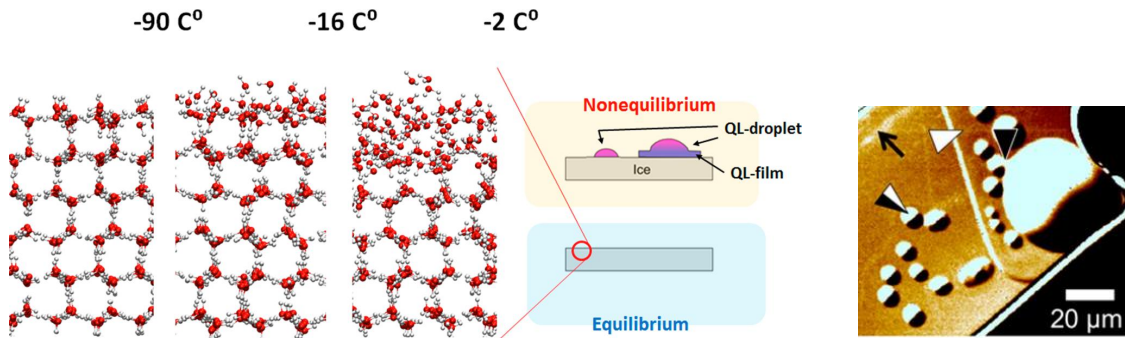


Figure 1.11: Left: results of molecular dynamics simulations showing state of prismatic faces at equilibrium for three temperature ranges, with progressive disordering corresponding to equilibrium quasi-liquid layer. Middle: summary scheme of the three quasi liquid layers. Right: observations of nonequilibrium quasiliquid layers with LCM-DIM. White arrowhead indicates a QLL-film, black arrowhead indicates QLL-droplet laying on a QLL-film, black and white indicates arrowhead QLL-droplet on bare-ice and black arrow a molecular step. From *Nagata et al.* [2019]

Quasi-liquid-layer / Surface premelting Its well known that ice crystals can be covered by a layer of disorderd mobile water molecules in the from of a liquid. This is called a Quasi-liquid-layer (QLL) since it has the structure of a liquid but is sufficiently thin to behave differently due to interaction with the bulk and vapor phase.

Following *Nagata et al.* [2019], three types of QLL actually exist: the premelted disorderd layers, QLL-films and QLL-droplets.

The first corresponds to the QLL mentioned classically [*Libbrecht, 2005; Furukawa, 2015*]. It arises from the fact that molecules close to the surface are not as strongly bonded together as in the bulk, thus the surface starts to melt before the melting point and the thickness increases with temperature until it diverges and extends to the complete crystal at melting point. This kind of QLL is homogeneously distributed over the ice surface. However, its thickness-versus-temperature dependence, its physical properties, and the impact of impurities are still highly debated as both experimental and theoretical studies do not lead to unified conclusions [*Bartels-Rausch et al., 2014*].

The two other types, QLL-droplets and QLL-films where observed only recently by *Sasaki et al.* [2012] and *Asakawa et al.* [2016] using an advanced microscopy technique. The QLL-films are thin films of 9 nm thick of water molecules partially wetting the ice surface. QLL-droplets are little droplets standing on bare ice or QLL-films. Both are heterogenously distributed and both appear on prismatic and basal

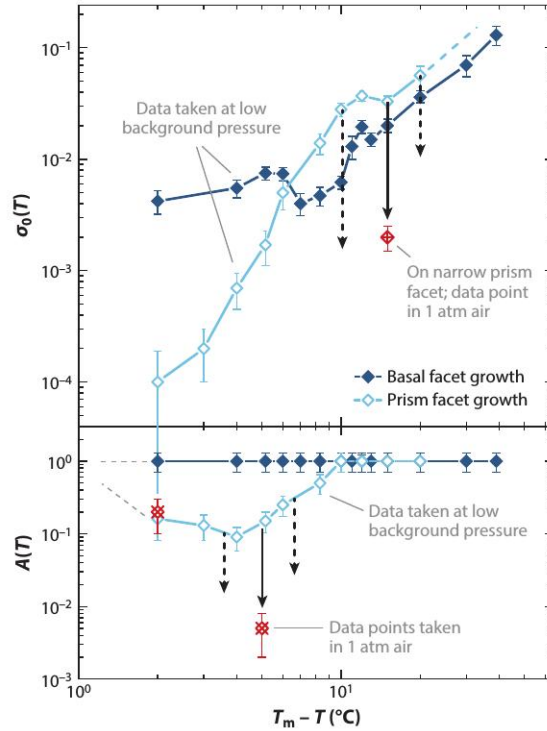


Figure 1.12: Measurements of α parametrised as $\alpha = A(T) \exp(-\sigma_0(T)/\sigma)$ for basal (dark blue points) and prismatic (light blue) faces at low background pressure. Red data points are isolated measurements, at atmospheric pressure for 2 of the 3 points. From *Libbrecht* [2017].

faces for temperatures above -2 °C and for high super- or under-saturation. Thus, those types of QLL are metastable phases appearing kinetically, in a non-equilibrium manner.

3.3 Measurements of kinetic coefficients

The condensation coefficient is difficult to measure. This is because one should have a well characterized ice crystal and have a good knowledge of both temperature and supersaturation at the interface while measuring with high accuracy its velocity. This difficulty results in a large variety of measurements, differing greatly in their conclusions and approaches (see e.g. *Cho and Hallett* [1984a, b]; *Sei and Gonda* [1989]; *Nelson and Knight* [1998]; *Libbrecht and Yu* [2001]; *Knight* [2012]; *Libbrecht and Rickerby* [2013]). The most recent measurements we are aware of are from *Libbrecht and Rickerby* [2013]; *Libbrecht* [2016] and *Libbrecht* [2017] and are presented in Figure 1.12. For this reason, we refer to this data when necessary, but one needs to keep in mind that it comes with large uncertainty and it needs to be confirmed and extended. Particularly, the data obtained are for low background pressure. This would need to be extended to atmospheric pressure for accurate parametrisation for snow metamorphism.

3.4 Surface tension anisotropy

The surface tension, or surface energy, may in principle, also be responsible for some faceting of the crystals. This is demonstrated by the Wulff construction [Wulff, 1901] when the surface tension γ depends strongly on the orientation of the facet. Some simulations of snowflakes growth have been performed accounting for surface energy anisotropy [Barrett *et al.*, 2012; Demange *et al.*, 2017]

Libbrecht [2012] discussed that possibility. Measurements of surface tension are difficult and we currently don't have accurate surface tension values. Anyway it appears that ice's anisotropy would not be more than a few percent, and that the Wulff shape or equilibrium shape of the crystal would be only slightly faceted, particularly at few degrees below the melting point. Note that, although the anisotropy is small, the value of the surface tension is important as it defines dihedral angles at the grains' joints [Ketcham and Hobbs, 1968; Blackford, 2007].

3.5 Links with snow metamorphisms

As introduced in section 2, the biggest uncertainties in the snow metamorphism picture remains on the transitions and particularly on the criteria of faceting. These come basically from two difficulties: the snowflakes morphology diagram is not accurately explained and the effect of the complex microstructure of snow on the ground are poorly understood.

Kuroda and Lacmann [1982] built a model based on available knowledge of crystal growth to explain the crystal habits of Nakaya diagram (figure 1.1). The model takes 3 surface states met successively when increasing temperature: i) smooth at low temperature where growth occurs through 2D nucleation leading to a kinetic coefficient β_{smooth} , ii) rough surface with kinetic coefficient of β_{rough} and iii) presence of a QLL near the melting point, leading to a kinetic coefficient β_{QLL} . The modeled kinetic coefficient follows $\beta_{rough} > \beta_{QLL} > \beta_{smooth}$ and the transition temperature between those surface states differs between surface and basal states (figure 1.13). The result is that prismatic faces grow more efficiently than basal ones over the ranges $[0, -4 \text{ }^\circ\text{C}]$ and $[-10 \text{ }^\circ\text{C}, -22 \text{ }^\circ\text{C}]$, with the reverse relation at other temperatures [Furukawa, 2015]. However, Libbrecht [2005] pointed out that this model predicts large differences in critical supersaturation between basal and prismatic faces which are not observed experimentally. Also the mechanism of growth in presence of a QLL is not well understood and quantified, particularly at high temperature where metastable QLL may be present [Nagata *et al.*, 2019].

More interestingly in case of metamorphism, is the origin of facets and hollow crystals like depth hoar and their observable striations?

As said before, anisotropy of surface energy may explain why equilibrium forms are rounded. This is reinforced by the presence of quasi liquid layer near equilibrium conditions over all faces [Colbeck, 1982]. However, when a critical supersaturation

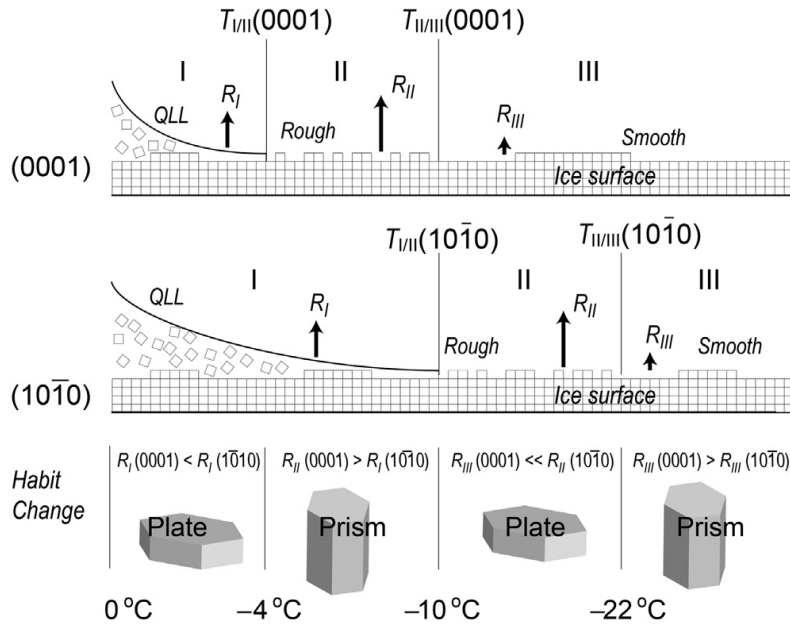


Figure 1.13: Representation of the Kuroda and Lacmann model for explaining Kuroda and Lacmann model. Face (0001) is basal face, (10 $\bar{1}0$) is prismatic face. From *Furukawa* [2015].

is reached faceted growth occurs. This was measured to be about 5×10^{10} g/cc [Colbeck, 1983b]. Colbeck [1982] mentioned a (screw) dislocation-aided growth to be the mechanism of facet growth. Miller and Adams [2009] implemented that mechanism of growth in their model. On the other hand, recent condensation coefficient measurements [Libbrecht, 2016] strongly suggest that 2D nucleation is always predominant in practice and, in addition, it is known that ice crystals contain few dislocations [Furukawa, 2015].

A general interpretation for the formation of hollow crystals like depth hoar or hollow snowflakes is the following [Libbrecht, 2005; Chernov, 1974]. The basic effect behind these shapes is the Mullins-Sekerka instability [Mullins and Sekerka, 1964]. In the vicinity of a faceted crystal, the vapor density is higher near the corners than at the faces centers. In consequence, the faces growth rate is higher closer to the corners than at the center, which leads to hollow faces. This instability is purely a diffusion effect. Taking into account kinetics and surface state into account, the picture can be improved. In addition to the fact that vapor concentration is higher at the corners, the crystal surface tends to be disordered close to the edge and this implies a higher probability of nucleation. So, steps propagate from the corners to the faces centers. However as they get closer to the center, step velocity decreases because of a reduced water vapor concentration. In consequence, the facets get slightly concave and the step density increases from the edges to the centers. In consequence, the kinetic coefficient is higher at faces centers. Thus, the kinetic coefficient profile counterbalances the supersaturation profile along the facets, and the facet grows mainly macroscopically parallel to itself. However, as

the crystal grows, the supersaturation differences between corners and faces centers increases, and so does the kinetic coefficient at the faces centers. At a critical size, the kinetic coefficient at the face center then reaches its maximum value and the kinetic coefficient profile does not counterbalance the supersaturation profile anymore. Then, the evolution is similar to the purely diffusive Mullins-Sekerka instability and the crystal becomes hollow.

Although this explains the pyramidal shapes of depth hoar, it does not explain the macroscopic striations often seen on depth hoar. Little information is available about the striations. Following *Libbrecht*^a, as the steps propagate toward the center of faces, surface diffusion effects lead to what is called step bunching. The monomolecular steps, due to complex interaction, actually stack together to form macrosteps, visible with a simple magnifier. *Chernov* [1974] explains that, in general over different materials, striated hollow crystals with flat bottom are the consequences of steps bunching or kinematic waves, that are due to adsorbed impurities on the surfaces or quasiepitaxial layers.

Desarnaud et al. [2018] produced hollow crystals of salt from solute. They observed formation of chains of hollow crystals for very high supersaturations, above a defined value. Their experiments shows involved a dendritic growth, which multiplies the surface area and allows more excess solute to be captured. This appears to be thermodynamically favorable, as it permits to go much faster towards equilibrium. Remarkably, this last interpretation is similar to the conclusions *Staron et al.* [2012, 2014]. Those authors grew depth hoar chains in low density snow and at very high temperature gradient: they showed that this process shortens the equilibrium re-establishment as the formed chains increase the thermal conductivity in the vertical direction and, thus, decrease the temperature gradient by increasing the heat flux.

3.6 Concluding remarks

From this review, three points can be made regarding snow metamorphism.

- The stepped structure of the crystal surface implies an anisotropy of the kinetic coefficient. This anisotropy may be responsible for the faceting. Anisotropy of surface energy is thought to be small, and is *a priori* not responsible for faceting. However, the evidence is scarce and this possibility is not totally ruled out.
- 2D nucleation appears to be the more plausible mechanism of growth [*Nelson and Knight*, 1998; *Knight*, 2012; *Libbrecht*, 2017], but dislocational growth is not completely ruled out. However, they lead to different responses of the surface to thermodynamic disequilibrium: dislocation-aided growth leads to

^a<http://www.snowcrystals.com/science/contents/DiffusionLimited.pdf>

$v_n \sim \sigma^2$, while 2D nucleation introduces a threshold on supersaturation σ , with $v_n \sim \sigma$ for $\sigma > \sigma_{crit}$.

- Surface state phenomena like roughening or quasi-liquid layers have strong effect on kinetics. They are temperature and supersaturation dependant, with again some treshold values on supersaturation for the existence of QLL-films and QLL-droplets.

These different kinetic mechanisms may be responsible for faceting, formation of hollow crystal, and the striations observed in kinetic forms of snow metamorphism. However, the exact mechanism is unknown and their actual effects on snow metamorphism need to be clarified.

4 Main objective of the thesis

The main objective of the thesis is to increase the understanding of the effects of attachment kinetics on snow metamorphism. In particular, we focus on the faceting of grains under temperature gradient metamorphism and on the impact of crystal habit on growth competition. These two aspects are respectively adressed through experiment and modeling.

Experiments To study kinetics effects, one should have a good knowledge of the crystalline orientation of the grains in snow. The objective is to obtain measurements of crystalline orientation during temperature gradient metamorphism along with microstructural evolution. In addition, this would permit exploration of the connections between grain activity and their orientation relative to the macroscopic temperature gradient.

Modeling The objective is to develop a realistic model for faceting in snow metamorphism from the current knowledge of ice crystal growth physics. This would permit us to have a better understanding of the control factors and the conditions of growth of the different types of snow. The model will need to fulfill two conditions. First, it should permit a realistic implementation of the kinetics in order to evaluate how the different mechanisms may explain the experiments. In particular, it should be capable of reproducing the balance between the weak gradient and the temperature gradient metamorphism. Secondly, the complex geometry of the microstructure plays an important role. Thus, the model should take into account the realistic geometry in order to get a deeper insight into the interplay between geometry and kinetics.

In the next sections, the experimental techniques and differents models available to reach these objectives are presented.

5 Experimental techniques

Imaging is an important aspect of snow experiments and several techniques have been developed with time, with increasing accuracy and sophistication. The following overview is not intended to be exhaustive but describes the main techniques of interest for the present work.

This includes using optical microscopes to look at single crystals [*Bentley and Humphries, 1931; Nakaya, 1954; Akitaya, 1974; Marbouty, 1980*], or using thin sections of samples, after the pore space has been filled with a liquid solidifying at negative temperature, these give 2D images [*Brzoska et al., 1998; Pfeffer and Mrugala, 2002*]. However, detailed description of metamorphisms must take into consideration 3D mechanisms. Thus, 3D imaging techniques are required. By doing successive thin sectioning of a cast sample, it is possible to obtain a 3D microstructure from the obtained stack of 2D images [*Good, 1987; Brzoska et al., 1999b*]. However, this is a destructive technique and it is not possible to follow the evolution at the grain scale with this approach. Currently, X-ray microtomography has become a standard method to observe snow microstructure [*Brzoska et al., 1999a; Flin and Brzoska, 2008; Pinzer and Schneebeli, 2009; Srivastava et al., 2010; Calonne, 2014; Wang and Baker, 2014; Krol and Löwe, 2016*]. This consists in building a 3D image from a set of 2D radiographs while the sample is rotated. An example is given in Figure 1.14a. This not only permits observations of 3D microstructure at few microns resolution, but also permits quantitative measurements using image analysis in a non-destructive manner. This is particularly interesting for in-situ study where the local evolution can be followed. This has been made relatively powerful and accessible with the development of cold-room capable tomographs and cryogenic cells that permit control of sample temperatures [*Schneebeli and Sokratov, 2004; Calonne et al., 2015; Wiese and Schneebeli, 2017*]. From 3D time-series images one can compute: interface velocity (and so phase change fluxes), density, specific surface area (SSA), pore size distributions, correlation lengths, etc. Using numerical modeling, it is possible to compute effective properties like effective thermal conductivity or diffusivity coefficient. Additionally, high resolution images have been obtained using electron microscopy techniques [*Dominé et al., 2003; Erbe et al., 2003; Wang and Baker, 2013*]. This technique permits the observation of the ice crystals surfaces in details.

Optical imaging techniques have been also employed to observe the crystalline orientation of the snow grains. The Automatic Ice Texture Analyser (AITA) [*Wilson et al., 2007; Riche et al., 2013; Calonne et al., 2017*] uses polarized light to observe the *c*-axis of crystals in a thin section (figure 1.14b). Diffraction Contrast Tomography (DCT) uses the diffraction of X-rays by the crystalline lattice to obtain a 3D image containing crystalline orientation information [*Ludwig et al., 2009b, a; Reischig et al., 2013*]. This technique has been employed in snow to study the deformation process

under compression [Rolland du Roscoat *et al.*, 2011]. It is an appealing technique as it is non-destructive and permits the study of mechanisms related to the crystalline structure along with microstructural change in an in-situ configuration (Figure 1.14c). This technique permits the measurements of quantities like orientation tensors. In addition, if one has prior knowledge of the crystalline orientations of the grains, the diffraction patterns bring information on the distances between crystallographic planes, which allow inference of the strain states of grains.

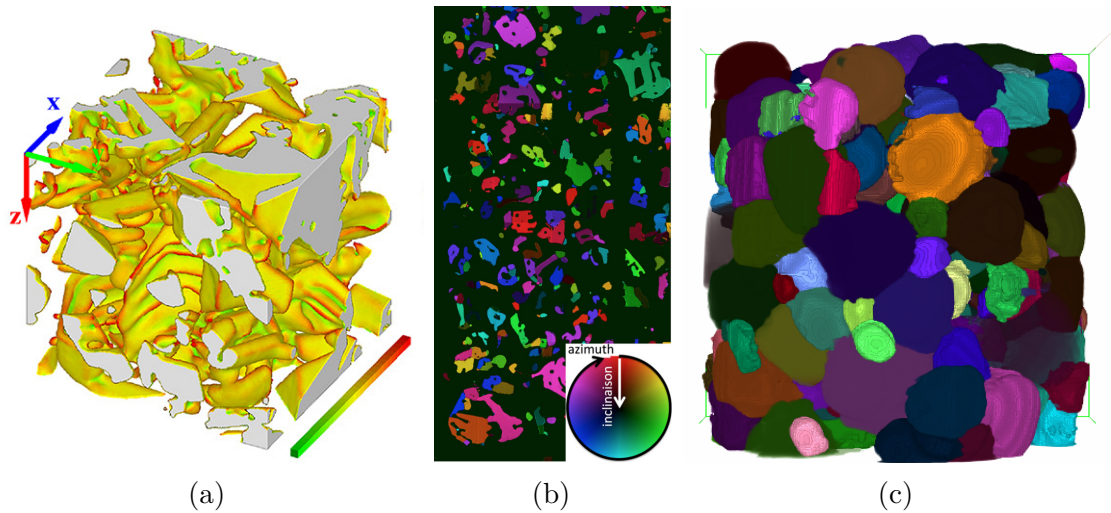


Figure 1.14: Example of results of snow imaging with different techniques. (a): absorption contrast X-ray microtomography, from *Calonne et al.* [2014a]. (b): 2D images of snow microstructure and orientations obtained with AITA, from *Calonne et al.* [2017]. (c): 3D image of snow microstructure with colours giving crystalline orientation obtained with DCT [Rolland du Roscoat *et al.*, 2011].

6 Microstructural Modeling

6.1 Motivations and problem

Several models exist for snow on the ground and snow metamorphism which can be classified in different categories depending on their objectives and scales.

1. Snowpack models, like CROCUS [Vionnet *et al.*, 2012] or SNOWPACK [Lehning *et al.*, 2006] are typically 1D models representing snowpacks as a stack of homogeneous layers. Properties of layers of interest are properties like heat conductivity, grain size, and specific surface area. Those properties can be computed using a number of parametrizations based on variable like density or grain type [Calonne *et al.*, 2011, 2012, 2014a, b]. This requires metamorphism laws that enable prediction of the evolution of the grain types.
2. Microstructural models with idealized geometry model the key processes of interaction at the grain scale. Parametrizations occur at the grain scale:

assumptions are made on the grain shape and the governing processes.[*Colbeck, 1983a; Legagneux and Domine, 2005; Miller et al., 2003; Miller and Adams, 2009*]. These models enable theoretical metamorphism laws to be developed at the layer scale taking into account identified mechanisms at the grain scale. Their predictions, along with experiments often serve as input for the previous 1D models (category 1).

3. Real geometry models [*Flin et al., 2003; Flin and Brzoska, 2008; Kaempfer and Plapp, 2009; Bretin et al., 2015; Demange et al., 2017*], even finer than the preceding models, use the real 3D geometry of snow microstructure. They basically allow identification of processes acting at the grain scale, giving a deep insight into the interactions. This brings complementary information to the experiments. In particular, the complex geometry of the snow microstructure is expected to explain an important part of the variability in the conditions of metamorphism. These models enable deep investigation of the effects of this complexity when considering some selected mechanisms like Kelvin effects. They allow fundamental understanding of snow metamorphism, necessary for designing models of category 1 and 2.

The most advanced model of category 2 [*Miller and Adams, 2009*] takes into account a large spectrum of microstructural processes. It considers rounded grains bounded by necks, and mass and heat fluxes are computed assuming equilibrium of heat and mass equation. Grains are considered to grow kinetically when the growth of a grain is positive. For kinetically growing grains, a hollow crystal geometry is assumed (see Figure 1.15). The kinetic growth mechanism is assumed to be due to screw dislocations. The model is built to accomodate both weak gradient and temperature gradient conditions, in a continuous manner. The model works really

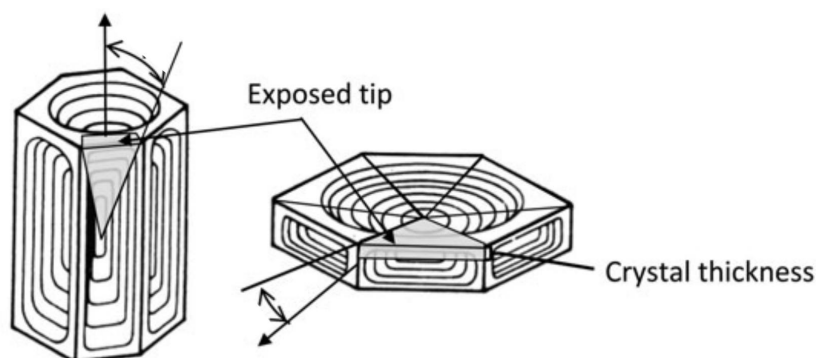


Figure 1.15: Geometry of kinetics forms of snow grains implemented in *Miller and Adams* [2009]

well in isothermal conditions,so that the transition temperature gradient is consistent with the relatively accurate empirically defined ones. However, the behavior in kinetic growth condition is valid for short times only. The kinetic forms expected by

the model are only hollow. Thus, faceted crystals are not considered and neither is the transition between faceted crystals to depth hoar, partly due to a lack of fundamental understanding of these transitions. In particular, faceting is assumed to start as soon as the growth begins everywhere on the grains. While this could actually be the case with dislocation-aided growth, it seems that dislocations are scarce in ice and it may be possible that growth of vicinal faces occurs mainly with 2D nucleation [Libbrecht, 2005; Furukawa, 2015; Libbrecht, 2017]. In that case, the supersaturation would need to overtop the threshold σ_{crit} for faceting to start. Then the velocity would go as $v_n \sim \sigma$, which is really different from the $v_n \sim \sigma^2$ in the case of dislocation-aided growth. Additionally, as being a model of category 2, this requires a physically representative geometry to be assumed and implemented. However, refining the geometry description of this model would require a better fundamental understanding of geometrical controlling factors.

In that perspective, real geometry models could help. The most advanced is the one of *Kaempfer and Plapp* [2009]. This is a phase-field model, which couples phase change to heat and water vapor diffusion taking into account curvature effects. It can conceptually be applied to any snow geometry. Particularly interesting is that model permit visualization of the heat and vapor fields and also do not make assumptions of diffusion limited or kinetic limited evolution.

However, it does not include any kinetic mechanism or faceting abilities. Thus, fundamental investigations on faceting are not permitted.

Barrett et al. [2012]; *Demange et al.* [2017] reproduced snowflake patterns, assuming strong surface tension anisotropy to be responsible for faceting. Interestingly, those patterns exhibited stepped surface anisotropies as it costs less energy under anisotropic surface energy.

The modeling part of this thesis proposes an extension of the *Kaempfer and Plapp* [2009] model, taking into account kinetic coefficient anisotropy as outlined in section 3.1.2 and exploring the fundamental consequences of the coupling of such anisotropy with diffusion of heat and water vapor for ice/air systems.

6.2 Phase-field modeling

6.2.1 Stefan problem

Let us consider a domain of dry snow as represented in Figure 1.16. Space domain filled with dry snow can be seen as the union of two domains: the pore space Ω_a filled with air and the ice phase Ω_i . The ice/air interface between the two domains is denoted Γ .

The temperature field T is defined on both Ω_a and Ω_i . The water vapor density field ρ_v is defined over Ω_a only and a normal interface velocity field v_n is defined on Γ .

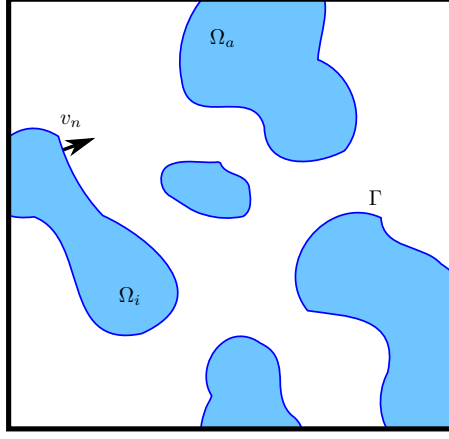


Figure 1.16: Schematic of dry snow with parametrisation

Considering heat diffusion only as an energy transport process, energy conservation leads to the heat equation over the 3D domains:

$$C_a \frac{\partial T}{\partial t} = \kappa_a \Delta T \quad \text{on } \Omega_a \quad (1.12)$$

$$C_i \frac{\partial T}{\partial t} = \kappa_i \Delta T \quad \text{on } \Omega_i \quad (1.13)$$

assuming heat conductivities κ_a and κ_i to be independent of temperature or water vapor density. C_a and C_i are heat capacities of air and ice respectively. On the interface, energy conservation gives:

$$T|_a = T|i \quad \text{on } \Gamma \quad (1.14)$$

$$\nabla T|_a + Lv_n = T|i \quad \text{on } \Gamma \quad (1.15)$$

The term Lv_n in equation (1.15) accounts for heat flux coming from latent heat release due to a phase change. Assuming mass transport occurring only through diffusion, mass conservation gives:

$$\frac{\partial \rho_v}{\partial t} = D_v \Delta \rho_v \quad \text{on } \Omega_i \quad (1.16)$$

$$D_v \nabla \rho_v = \rho_i v_n \quad \text{on } \Gamma \quad (1.17)$$

where D_v is the diffusion coefficient of water vapor through the air phase which is assumed to be independent of both T and ρ_v . The local velocity is prescribed by the Hertz-Knudsen relation (equation (1.1)). Using linearized expression (1.8) for ρ_{vs} , replacing in σ (equation 1.3), and rearranging terms leads to [Kaempfer and Plapp, 2009]:

$$\frac{\rho_v - \rho_{vs}(T^{ref}, 0)}{\rho_i} = \frac{\rho_{vs}(T, 0) - \rho_{vs}(T^{ref}, 0)}{\rho_i} + \frac{1}{\alpha} \frac{\rho_i}{\rho_{vs}(T, 0)} \sqrt{\frac{2\pi m}{k_B T}} v_n + d_0 K \quad (1.18)$$

of the form

$$u = u_{eq}(T) + \mu v_n + d_0 K \quad (1.19)$$

where $u = \frac{\rho_v - \rho_{vs}(T^{ref}, 0)}{\rho_i}$ is the dimensionless water vapor density and $u_{eq}(T) = \frac{\rho_{vs}(T, 0) - \rho_{vs}(T^{ref}, 0)}{\rho_i}$ is a dimensionless water vapor density at saturation. The system of equations (1.12) to (1.19) forms a particular kind of boundary value problem called a Stefan problem, with two diffusion fields. The unknowns of this system are the fields T , ρ_v and v_n . That kind of mathematical problem is particularly current in solidification of alloys. It is not a trivial problem to solve as the domains of definition of the above equations are both complex and evolving with time, with evolution prescribed by the system itself. This creates an highly non linear problem. Several numerical methods have been developed by the solidification community. They can be classified in two main types: explicit and implicit boundary methods. Explicit boundary methods move an explicit boundary depending on the computed velocity. An example is the boundary element methods used by *Yokoyama and Kuroda* [1990]. The main disadvantage of explicit methods is that handling topological changes like grains or bonds disappearing is difficult. The other category of methods uses an implicitly defined interface between the phases. This are of two kinds: level-set or phase-field method. The level-set method uses a distance field to the interface to define the interface as the 0 level-set of that function. The field is then advected following interface velocity field computed from equation (1.1). A disadvantage, of this method is that the distance field may get distorted, so that a re-initialisation step is required to guarantee the level-set function to be a distance field, and the mass flux can be erroneous.

Another implicit method is the phase-field method, in which the phases are represented by an indicator function taking distinct definite values in the different phase domains, with a smooth transition, representing the interface between the domains. This method is usually chosen by the solidification community. The most recent developments for snowflakes [*Demange et al.*, 2017] or snow metamorphism [*Kaempfer and Plapp*, 2009] use that method.

6.2.2 Principles of phase-field modeling

The main principle of phase-field modeling is to replace the two evolving domains Ω_a and Ω_i by an indicator function ϕ called the phase-field, that evolves between -1 in one domain to 1 in another (Figure 1.17). The evolution, instead of being prescribed by an explicit normal velocity v_n is prescribed by a differential equation for ϕ , called the phase-field equation. The phase-field equation must have some properties: i) ϕ should always vary between -1 and 1 ii) the variations should be concentrated in a thin region along the iso-0 iii) the equation should be coupled to heat and mass equation so that the velocity field v_n , computed as the velocity field of the iso-0, ρ_v and T are solutions of the Stefan problem presented above.

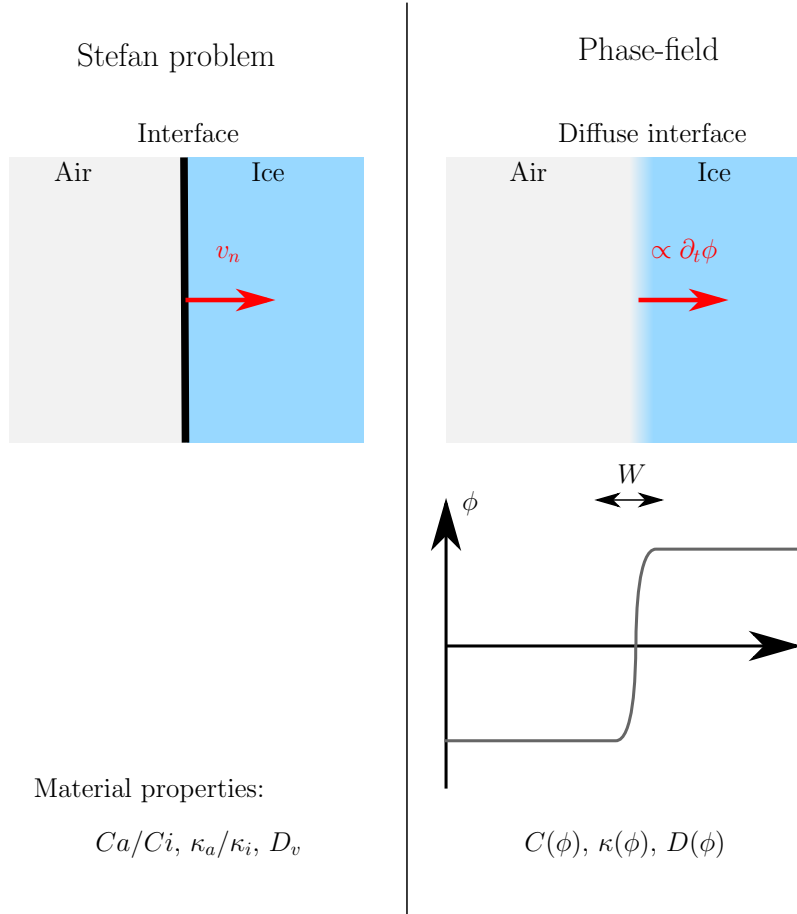


Figure 1.17: Representation of the phase-field approach.

In the following, we just give the spirit of the match asymptotics analysis that permits us to set up the phase-field model and understand its functioning. For a detailed demonstration we refer to *Karma and Rappel* [1998]; *Almgren* [1999] and *Plapp* [2012].

The phase-field system can be written as:

$$\tau \frac{\partial \phi}{\partial t} = W^2 \Delta \phi - \frac{\partial}{\partial \phi} f(\phi) + \lambda g'(\phi)(u - u_{eq}(T)) \quad (1.20)$$

$$\frac{\partial u}{\partial t} = \nabla D(\phi) \nabla u - \frac{1}{2} \frac{\partial \phi}{\partial t} \quad (1.21)$$

$$C(\phi) \frac{\partial T}{\partial t} = \nabla \kappa(\phi) \nabla T + L \frac{1}{2} \frac{\partial \phi}{\partial t} \quad (1.22)$$

where τ and λ and W are some model parameters. D , C and κ are respectively the water vapor diffusivity, heat capacity and thermal conductivity functions that depend on ϕ in the phase-field simulation.

Equation (1.20) is the phase-field equation, in the form of a Allen-Cahn equation because the field ϕ , in our case, is a non conserved quantity. Sometimes, a Cahn-Hilliard equation is found in phase-field litterature, because it is usefull to model

physical problems where typically the volume of each phase is conserved, as for example in two phase flow. The function f is a double-well potential generally taken as $f(\phi) = -\phi^2/2 + \phi^4/4$. This would ensure that the phase-field will relax towards values of -1 or 1 far from the interface. The Laplacian term guarantees that no variations occur in the bulk, and is balanced by the double-well potential term in the diffuse interface. It is precisely the balance between those two terms that creates the diffuse interface, and W is in fact the thickness of that interface. The last term in the right hand side of the equation is the coupling term that permits coupling with the diffusive fields. The diffusion equations (1.21) and (1.22) are analogous to the classical diffusion equations. The differences rely on the fact that the material properties which physically depend on the phases, will depend here on the phase-field, where the value in the diffuse interface is interpolated by some function between the value in the phases. The last term is a source term accounting for phase change in the diffusion fields, typically it ensures interface jumps like (1.15) and (1.17) are fulfilled.

Then an asymptotic analysis needs to be performed to show that the system (1.20)-(1.22) is equivalent to the Stefan problem and to get the expressions of λ and τ .

In an asymptotic analysis, one should estimate the order of magnitudes of the different spatial derivative terms that are present. A complexity here is that the problem is intrinsically multi-scale: variations of ϕ occur in a restricted region (the diffuse interface of thickness W) while it is almost not varying elsewhere. In consequence, one unique order of magnitude cannot be given to terms like $W^2\Delta\phi$. To overcome this problem, the strategy consists in i) developing asymptotically the equations in the bulk on the one hand and on the diffuse interface in the other hand ii) matching solutions order by order and by matching solutions in the diffusion region to the solution in the bulk.

Such an analysis was performed by *Almgren* [1999] up to the second order for the case of unequal diffusivity. It typically shows that the solution of the phase-field system is a solution of the Stefan problem up to a $\mathcal{O}(W)$ term. Namely, this gives relations of the form:

$$[D\nabla_n u]_\Gamma = v_n + \underbrace{W\left[\frac{1}{2}(H_+ - H_-)K_0V_0 - (J_+ - J_-)D\Delta_s u_0\right]}_{\mathcal{O}(W)} \quad (1.23)$$

where H_+ and H_- , J_+ and J_- are integrals computed from interpolation function and coupling function g , K_0 is the interface curvature at first order, V_0 is the velocity at first order, u_0 is u at first order and Δ_s is surface Laplacian on the interface. $[D\nabla_n u]_\Gamma$ is the jump of flux at the interface, which should meet the Stefan condition $[D\nabla_n u]_\Gamma = v_n$ (equation 1.17 for u), which is, thus, satisfied if the $\mathcal{O}(W)$ term is small enough. From the inspection of the structure of this term, there are basically two ways of doing this. One can choose to take W small enough, i.e. a really

small interface thickness, which is called the *sharp-interface limit*. Or one can choose to make that term vanish by choosing the right interpolation and coupling functions so that the differences between the integrals vanish, which is referred as the *thin-interface limit*.

The first solution works and doesn't require much further analysis and development. However, when solving numerically the system, this requires fine grids in the interface region which makes quantitative simulations computationally heavy. The second possibility requires deeper mathematical analysis but permits the use of W of the scale of the microstructure.

6.2.3 Advantage of phase-field method for solving Stefan problems

The phase-field formulation has several advantages:

- It is an implicit method: topological changes can be easily handled. This is an important property for snow metamorphism as we expect some grains and bonds to disappear.
- The rigorous mathematical analysis ensures a good convergence of the formulation to the Stefan problem and links model parameters to physical parameters. This is maybe the strongest advantage of phase-field as it makes the approach very robust. It is interesting when one want to quantify the theoretical effects of a phenomenon as it can be proven that the approximation made is good.
- It leads to a reaction-diffusion equation which is more stable to solve numerically in comparison to advection equation as it can be used in level set method.
- *Slavov and Dimova* [2006] compared phase-field and level-set methods for 2D dendritic growth and concluded that the phase-field method is more adapted to solve dendrite interaction. This seems important in snow metamorphism as we expect the interaction between growing grains to have a central role.

However, the bottleneck of phase-field method is the scale separation between the diffuse interface scale and the microstructure scale, which can be several orders of magnitude. This is particularly true in the sharp interface limit as the interface thickness W has to be really small. In consequence, the computational time can be really high as it requires a really fine grid at the interface. However solutions have been developed to reduce this problem. The first one is to use the thin-interface limit [*Karma and Rappel*, 1998]. The second is to use an efficient adaptative mesh refinement method (e.g. *Greenwood et al.* [2018]). Indeed, fine mesh is really necessary only in the diffuse interface. Thus, adaptive-mesh refinement can significantly reduce the computational cost.

6.2.4 Overview of phase-field models of interest – similarity with snow

In addition to the common difficulties linked to the phase-field approach, the problem presented in section 6.2.1 for snow presents specific difficulties. The first is that the vapor field diffuses in the air phase but does not in the ice. Thus, the value of the diffusivity field vanishes at the interface. In the phase-field literature this is named a one-sided problem. As a consequence, as depicted by *Kaempfer and Plapp* [2009], the phase-field formulation generate anomalies: erroneous conservations at curved interfaces (*interface stretching*) which is the K_0V_0 term in equation (1.23), a surface diffusion term (Δ_s term in equation (1.23)), and a magnified temperature/vapor density jump also referred as *solute trapping*.

Those anomalies are all negligible in the sharp-interface limit. However, that creates additional anomalies to the classical anomalies for equal diffusivities when W is increased. As shown by *Almgren* [1999], it is not possible to correct efficiently all those anomalies in the thin-interface limit by a choice of interpolation functions. This requires the addition of an anti-trapping current [*Karma and Rappel*, 1998; *Echebarria et al.*, 2004] to add more degrees of freedom for corrections.

A second complexity arises from the fact that two diffusive fields are coupled to the phase change (heat and mass). That kind of problem was solved for alloy solidification by *Ramirez et al.* [2004] for the case of unequal diffusivities. While it does not introduce more conceptual complexity, it increases the number of degree of freedoms and the computational cost. *Kaempfer and Plapp* [2009] use that study to derived a phase-field model for snow metamorphism in the sharp interface limit.

In addition, it is necessary to take into account faceting to study snow metamorphism in generalized conditions. In alloy solidification, most of faceting is attributed to surface tension anisotropy [*Kobayashi*, 1993; *Karma and Rappel*, 1998; *Eggleston et al.*, 2001]. That kind of anisotropy was recently used by *Demange et al.* [2017] using the phase-field approach to simulate snowflakes patterns. However, as in snow metamorphism that surface tension is supposed to be isotropic and faceting is supposed to be due to kinetic effects, it would be interesting to use instead an anisotropic kinetic coefficient. Studies on kinetic faceting in the phase-field method are more rare. *Uehara and Sekerka* [2003] reported kinetic faceting using a highly anisotropic kinetic coefficient in a phase-field model with singular narrow minima. It uses a kinetic coefficient of the same kind as that presented by *Yokoyama and Kuroda* [1990] in their boundary element simulations.

7 Structure of the manuscript

As presented previously, the thesis focus on manifestations of attachment kinetics on snow microstructure evolution. The next part of the manuscript is divided in four chapters.

Chapter 2 Kinetic differences between basal and prismatic faces may play a role in competitions between grains. At a given temperature, a current hypothesis is that grains with their most active faces oriented towards the vapor flux will be favorably oriented to grow at the expense of others. *Riche et al.* [2013] and *Calonne et al.* [2017] report evolution of the fabric due to temperature gradients. Their observations confirm the hypothesis at the macroscopic scale. However, the method used does not allow linking of the local growth to the crystalline orientation. Thus, observations at the grain scale are desirable complementary information to bring to the picture.

This chapter reports for the first time an experiment of time-lapse Diffraction Contrast Tomography (DCT) performed at the European Synchrotron Radiation Facility (ESRF) on snow under a temperature gradient. This unique approach permits us to obtain the 3D geometry of the microstructure and the crystalline orientation during the evolution of the sample in a non-destructive manner. From these data, the relationship between the local growth velocity and the orientation of the crystal is investigated and kinetics effects are highlighted.

Chapter 3 The phase-field model of *Kaempfer and Plapp* [2009] is extended with anisotropy for the kinetic coefficient to reproduce faceting. The model is solved using the Finite Element code COMSOL Multiphysics. We compare simulations in the sharp-interface limit, accepting the associated constraints, with experimental observations. The experiment under consideration concerns an air cavity migration and faceting in a monocrystalline ice block under temperature gradient metamorphism. The experiment is monitored using X-ray microtomography.

Chapter 4 We then present additional simulations, always in the sharp-interface limit, modifying the kinetic coefficient ratio between the basal and prismatic faces to reproduce the snow crystal habit. Numerical results are compared with ones obtained during an experiment of negative crystal growth monitored with optical microscopy.

Chapter 5 We present some preliminary results from ongoing work on numerical investigations of temperature gradient metamorphism. This shows predictions of evolution of an isolated grain, under axisymmetry assumption. In particular, the dependence of the shape evolution upon grain size, temperature and temperature gradient is shown. Finally, the potential of proposed modeling to describe the 3D faceting is illustrated through qualitative simulations.

Note that chapters 2, 3 and 4 have been written in the perspective to be published separately. In consequence, it may appear that some aspects are repeated.

Orientation selective grain activity in snow under temperature gradient metamorphism observed with Diffraction Contrast Tomography

Abstract

In this study we investigate the hypothesis that there exists during temperature gradient metamorphism a favorable crystalline orientation relative to the temperature gradient. We apply in situ time-lapse Diffraction Contrast Tomography on a snow sample with density of 476 kg m^{-3} subject to a temperature gradient of $52 \text{ }^\circ\text{C m}^{-1}$ at mean temperature in the range of $-4 \text{ }^\circ\text{C}$, $-2 \text{ }^\circ\text{C}$ for three days. The orientations of about 900 grains along with their microstructural evolution are followed. Faceted crystals appear during the evolution and from the analyses of the fluxes, we indeed observe more activity for grains with their *c*-axis in the horizontal plane at the beginning of the metamorphism. This remains to the end of the experiment for the sublimation while it becomes equal for all orientations for deposition. That latter fact is explained in terms of geometrical interactions between grains.

2.1 Introduction

A snowpack is a porous media made of ice crystals, air and sometimes liquid water. The microstructure of this material is in constant evolution and the original fresh snow is transformed as an effect of various mechanisms called snow metamorphisms. In particular, a temperature gradient in a snow layer implies a gradient of water vapor density, which creates a vapor flux in the pore. Under these circumstances, ice crystals interfaces may be significantly out of equilibrium with the vapor phase if the macroscopic temperature gradient is typically higher than $10\text{-}20 \text{ }^\circ\text{C m}^{-1}$. Growth and decay under those conditions depend strongly on kinetics, so that kinetic forms (faceted crystals and depth hoar) of snow crystals appear [Colbeck, 1983a]. An important aspect of temperature gradient metamorphism is that the grain size increases while the density remains constant [Marbouty, 1980; Schneebeli

and Sokratov, 2004; Srivastava *et al.*, 2010; Pinzer *et al.*, 2012; Calonne, 2014]. Some grains are growing at the expense of others [Akitaya, 1974; Pinzer *et al.*, 2012]. In addition, the kinetic coefficient is not equal on the prismatic and basal faces of ice [Libbrecht, 2005; Furukawa, 2015]. In consequence, growth and decay of a crystal in a vapor gradient depends on the orientation of the crystalline structure relative to the thermal (and also water vapor at saturation) gradient, with higher sublimation and deposition when the more active faces efficiently catch and release the flux.

In that context, Adams and Miller [2003] and later Miller and Adams [2009] conjectured that, in temperature gradient metamorphism, favorably-oriented crystals might grow at the expense of others as they grow more quickly towards the common vapor source. Because of that selective growth of crystals, the distribution of crystallographic orientation, called the fabric, is expected to evolve towards an anisotropic fabric. However, few studies report data on the subject. Takahashi and Fujino [1976] and de Quervain [1983] measured crystal orientation but the data are too scarce to draw conclusions. Since then, this aspect has not been studied until two recent works.

Riche *et al.* [2013] measured the fabric evolution over natural and sieved samples under a $50\text{ }^{\circ}\text{C m}^{-1}$ temperature gradient for 12.5 weeks, at a mean temperature of $-20\text{ }^{\circ}\text{C}$. They used the Automatic Ice Texture Analyser (AITA) [Wilson *et al.*, 2007] that enables measurement of crystallographic orientations of thin sections. They observed an evolution of the fabric from strong cluster-type (with *c*-axis of ice crystals mainly in one direction) to weak girdle-type (with *c*-axis mainly in a plane) for the natural samples, while no evolution for the denser sieved sample was observed. Calonne *et al.* [2017] analysed snow-firn profiles from Antarctica in terms of i) microstructure using microcomputed tomography and ii) fabric using AITA. They showed that the snow fabric is correlated with its microstructure, with the more isotropic fabric being found in the denser snow with smaller SSA. This suggests that metamorphism affects the fabric. While AITA is an efficient instrument to obtain statistical data on fabric and on different samples, it requires thin sectioning of the sample. Consequently, it is not possible to follow the evolution of individual grains and observe the role of orientation in the mechanism at the grain scale.

To bring such complementary understanding to the picture, we present here a 3 days long experiment of temperature gradient metamorphism, monitored by conventional tomography and Diffraction Contrast Tomography (DCT). DCT is a tomography modality that uses contrast due to diffraction of the incident beam by the sample crystals. By measuring the position of the associated diffraction spots, it is possible to reconstruct the crystals orientation [Reischig *et al.*, 2013]. This technique is non destructive and permits in-situ observations and has already been used for snow to follow deformation under compression [Rolland du Roscoat *et al.*, 2011].

In the first section, we describe the sample preparation, the experimental setup

and the core image processing. In the second section, we present time series images, sample characterisation and analyses of the relation between grain orientation and fluxes. Finally, we discuss the observed trends, the representativity of the experiment, as well as the main technical difficulties met with the imaging technique.

2.2 Methods

2.2.1 Sample and sample environnement

To impose controlled temperature conditions on the sample, we used a modified version of the cryogenic cell CellDyM [*Calonne et al.*, 2015]: the sample is inserted in a sample holder placed between two copper columns, at the extremities of which temperature is controlled using Peltier modules. The sample holder and the copper columns are placed in a vacuum chamber for thermal insulation from room temperature (see Figure 2.1). However, to be usable in a DCT experiment, the cell had to be modified. First, The original aluminium sample holder, with crystalline grains can create parasitic diffraction spots and has been replaced by a system of three components:

- a 6 mm thick polymethyl methacrylate (PMMA) holder of inner diameter 10 mm
- a 3 mm thick graphite cylinder of inner diameter of 4 mm
- a thin polypropylene (PP) tube inside the graphite cylinder.

The PMMA holder ensures a vacuum-tight assembly. The graphite of thermal conductivity $95 \text{ W m}^{-1} \text{ K}^{-1}$ with crystalline grain size of $\approx 5 \text{ }\mu\text{m}$ ensures good thermal conductivity between the two copper columns and, thus, good control of the temperature gradient without problematic parasitic diffraction spots. Finally, the PP cylinder avoids the diffusion of water vapor inside the porous graphite, and transport of its dust into snow. The vacuum in the chamber is produced by a system of two pumps: a primary scroll pump (Anest-Iwata ISP-90) produces a pressure of about 500 Pa, which permits to a turbomolecular pump (Pfeiffer Vacuum HiPace 30), directly mounted on the turntable, to reach the final pressure of 0.009 Pa.

The sample consists of a cylinder of a rounded grains snow of 4 mm in diameter and 4 mm height, with 3 mm thick ice lenses on the top and bottom. In order to minimise parasitic diffraction spots, ice lenses were machined from monocrystals using a specific core drill. The sample was made in cold room at CEN and consists in fresh snow picked up at the upper station of La Grave cable car and stored at $-20 \text{ }^\circ\text{C}$ for 7 months. This snow was then metamorphised at $-5 \text{ }^\circ\text{C}$ in equilibrium conditions for 3 days. A specimen was then cored in a homogeneous zone, and assembled on the bottom copper column with the bottom ice lens. The top ice lens was then stuck to the top copper column, which was hence placed at the upper part of the sample.

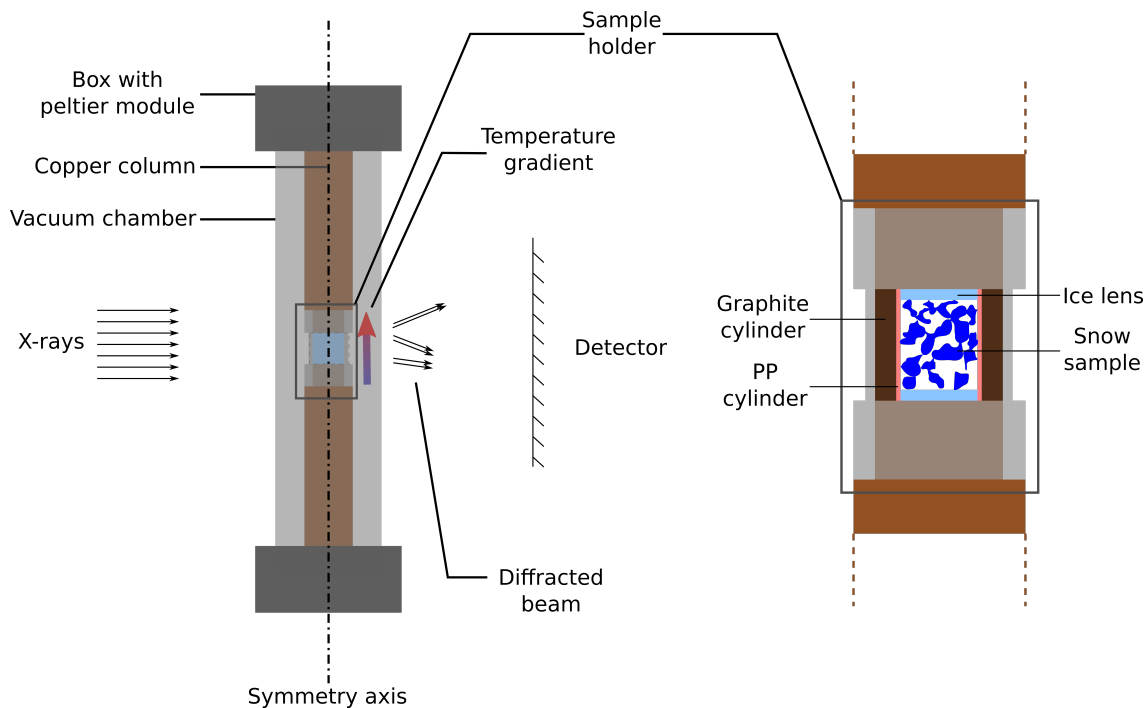


Figure 2.1: Scheme of the cryogenic cell.

The assembly was then stored in a specific copper handling tube, preserving the sample from possible temperature gradients during storage. The whole assembly was then transported to ESRF within a carriable freezer and inserted in the cell at -20 °C.

As soon as the cell was closed, pumping the air out from the vacuum chamber started, and the peltier regulation was progressively set to -2.1 °C. It took 27 min to reach the pressure of 0.046 Pa and less than 7 h to reach the stable pressure of 0.009 Pa. The value of -2.1 °C was reached in about 1 hour and the sample stayed in equilibrium conditions for 21 additionnal hours. Then, the proper temperature gradient experiment began: this corresponds to the instant $t=0$ in this paper.

Thermal conditions of the experiment are then given by Figure 2.2. This consists in three phases that we will now refer as phase 1, phase 2 and phase 3. Mean temperature and temperature gradients were respectively set to -2.1 °C and 17 °C m^{-1} during phase 1, -2.1 °C and 52 °C m^{-1} during phase 2 and -4.1 °C and 52 °C m^{-1} during phase 3. These conditions on snow sample are determined from temperature measurements at the Peltier modules location using numerical simulation of the cell, using COMSOL Multiphysics, as presented by *Calonne et al.* [2015].

2.2.2 Diffraction Contrast Tomography: Experimental Setup

The experiment was performed at ID19 beamline of the European Synchrotron Radiation Facility (ESRF). We used a beam energy of 40 keV with a silicon double crystal monochromator in Laue-Laue setting produced by the 4 bunch mode of the storage ring. Detection was performed using a 200 μ m LuAG screen coupled with

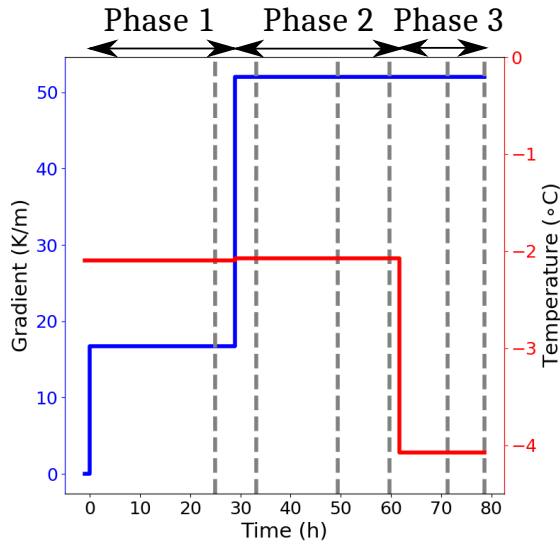


Figure 2.2: Evolution of the temperature conditions imposed over the sample: mean temperature and temperature gradient.

visible light optics to a sCMOS camera. The distance between rotation axis and the detector was 60 mm. The resulting pixel size was 6.5 μm .

DCT scans lasted for about 1 hour and produced 7200 images, with an angular resolution of 0.05° . Absorption scans lasted 10 min and produced 900 images for an angular resolution of 0.4° . DCT and absorption scans were performed alternatively so that there was systematically an absorption scan performed in the 20 minutes before a DCT scan.

Reconstruction was performed following the workflow presented by *Reischig et al.* [2013]. Here is a brief outline of the processing route:

1. Preprocessing: distortion and constant background correction are applied to the images stack.
2. Segmentation of diffraction spots: double soft thresholding.
3. Matching Friedel pairs: when a crystalline plane meets the Bragg's condition and leads to a diffraction spot for a position ω of the rotation stage, then the Bragg conditions is met again at $\omega + 180^\circ$ and the two associated diffraction spots are called a Friedel pair. Over 360° , a crystallographic plane in one grain can meet the Bragg conditions up to four times and so leads to two Friedel pairs. From the raw images, segmented spots are then associated by Friedel pairs, based on position on detector, intensity and shapes.
4. Indexing grains: the position and orientation of grains are computed from Friedel pairs and by grouping diffraction spots corresponding to the same grain.
5. Selection of diffraction spots.

6. Reconstruction of grain shapes: performed from selected spots for each grain using the SIRT algorithm [Palenstijn *et al.*, 2013, 2015].
7. Assembly of the grains map: the reconstructed grains are assembled to form the full sample volume.
8. Masked dilation: morphological dilation of the reconstructed grains map constrained in the domain of ice in the segmented volume from the absorption scans.

The last step was added for this experiment in comparison to the description given in Reischig *et al.* [2013]. Indeed, ice crystals in snow are nearly perfect which leads to dynamic diffraction: the beam diffracted by one crystallographic plane meets the Brag condition a second time before getting out of the ice grain, and so, a part of its intensity is diffracted back in the original incident direction. As a consequence, diffracted spots on the detector are inhomogeneous in intensity. The segmentation may thus lead to holes or overlaps in the segmented spots, which in turn gives partial reconstruction of the resulting grains. The localisation of ice phase can be easily obtained from the absorption scans, the dilation enable us to correct the partially reconstructed grains. Figure 2.3 shows the effect of this correction on a horizontal slice of the sample. While this enables recovery of the correct information for most of the voxels, this may lead to wrong orientation for voxels in the vicinity of the grain boundaries. This point will be discussed in section 2.4 in the light of the obtained results.

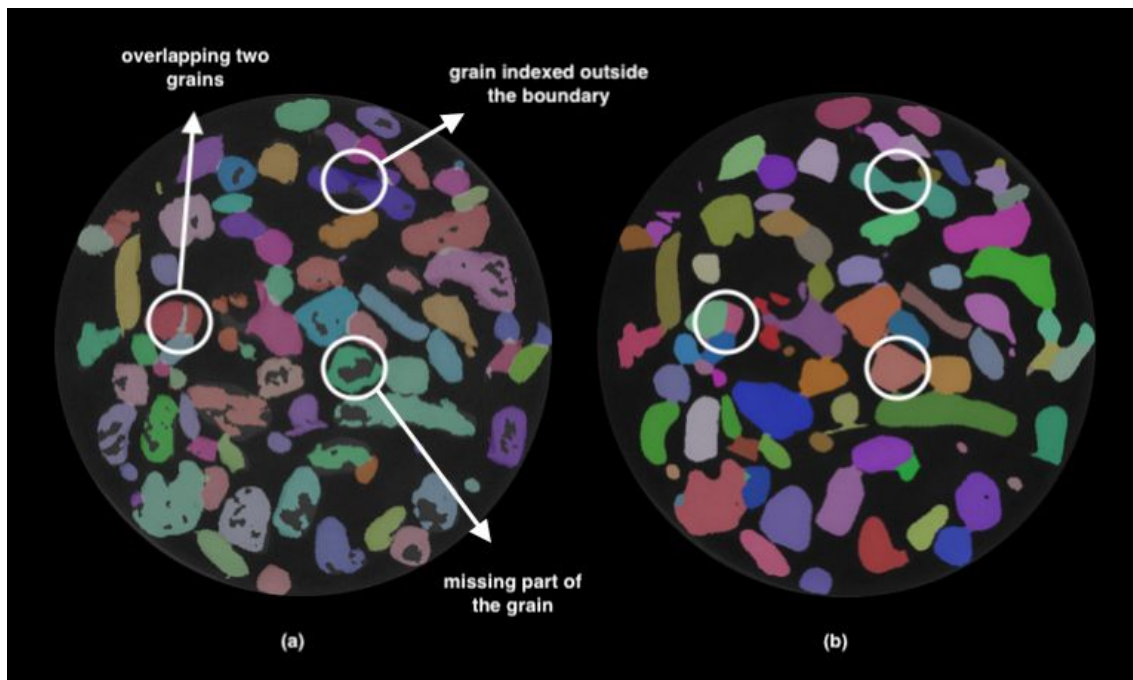


Figure 2.3: Effect of step 8 to improve the reconstruction quality. (a) Before correction (b) after correction.

2.2.3 Data processing

Reconstruction of the absorption scans were performed using filtered back projection (FBP) algorithm. Ring artefact were corrected.

Because some movements of the stages and detector may occur during data acquisition, it is necessary to register the time series of the reconstructed volumes. To simplify that step, grooves were made on the exterior side of the PP cylinder following both the axis and the circumference. First, all absorption volumes were registered on a reference volume (taken at $t=27\text{h } 32\text{min}$, at the beginning of phase 2). Registration was performed using the SimpleITK library and consists of:

- smoothing the image with a gaussian filter with kernel size of 2 voxels,
- finding the optimal translation in the horizontal plane,
- finding the optimal vertical translation,
- applying the total transform to the not smoothed reconstructed volumes with linear interpolation.

Optimal was defined by maximising the correlation computed in a hand selected ROI focusing on the grooves. Registered volumes were then segmented using energy based segmentation algorithm [*Hagenmuller et al.*, 2013].

Some grains may be missing during the DCT reconstruction because the diffracted beam may not hit the detector or the quality and quantity of grouped diffraction spots are not sufficient for reconstruction. To correct, requires manual monitoring and processing through out the sample volume. For that reason, only a selected subset of the DCT scan was processed in that study. Times at which a processed volume is available are represented by grey dotted lines on Figure 2.2. The correction consists of comparing the reconstructed absorption and DCT scans in order to detect missing grains, and then by comparing the former and latter volumes in the time series to get the orientation of the grains which remain fix during the experiment as no rearrangement occurs. After that, because absorption scans were always performed shortly before the DCT scans, DCT scans were directly registered on the closest absorption volume by finding the optimal translation in space that maximise correlation between the two volumes, without ROI selection.

2.3 Results

2.3.1 Images time series

Figure 2.4 shows images of the microstructure at $t = 25.1\text{ h}$ and $t = 78.6\text{ h}$ of a cubic subsample of edge length 2.34 mm in the center of the sample. The colors represent the mean curvature computed with an algorithm developed by *Flin et al.* [2005], and ranges from -46 mm to 46 mm. First, we can see that the initial microstructure of

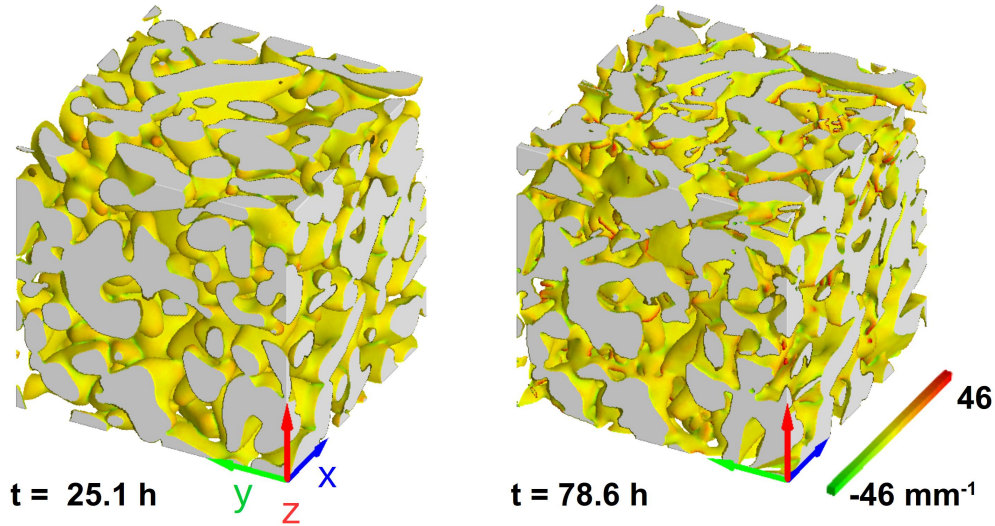


Figure 2.4: Time series of the evolution of the microstructure in a cube of 2.34 mm edge length cropped out of the center of the specimen. The Interfaces are coloured based on the local mean curvature.

the snow consists of small well rounded grains. The global evolution is small as full recrystallization of the grains is not observable. However, gradient metamorphism occurs as we can observe a global migration towards the bottom. We do not see any grain rearrangement.

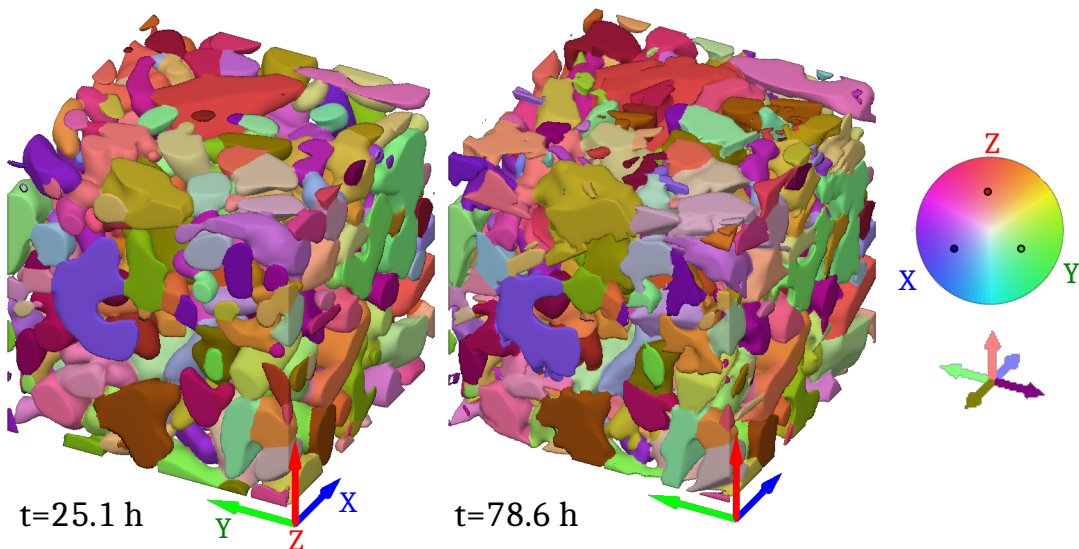


Figure 2.5: Grain map. Each colour represents a single crystalline orientation. The meaning of the colors is given by the color wheel, representing colors in a pole figure representation centered on a vector $\mathbf{x} + \mathbf{y} + \mathbf{z}$. The axes under the color wheel show the color corresponding to the main directions.

In Figure 2.5, we present the result of the DCT acquisition obtained after

processing route presented in section 2.2.3. We represent the orientation of the c-axis by a unit vector \mathbf{c} whose direction is the c-axis and, by convention, has positive vertical component. On the figure, the direction of c-axis is represented by a color given by the color wheel.

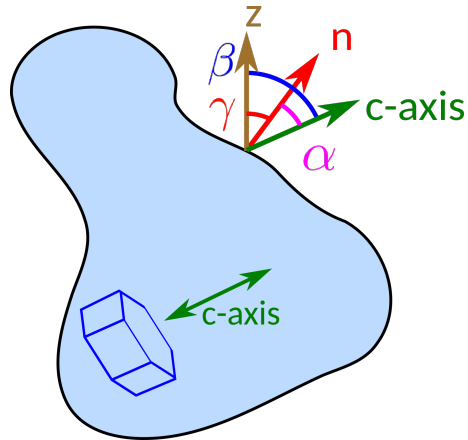


Figure 2.6: Parametrization of the different vectors and angles. \mathbf{z} is the vertical unit vector, \mathbf{n} is the local normal outgoing from the ice and \mathbf{c} is a vector with positive vertical component representing the c-axis direction.

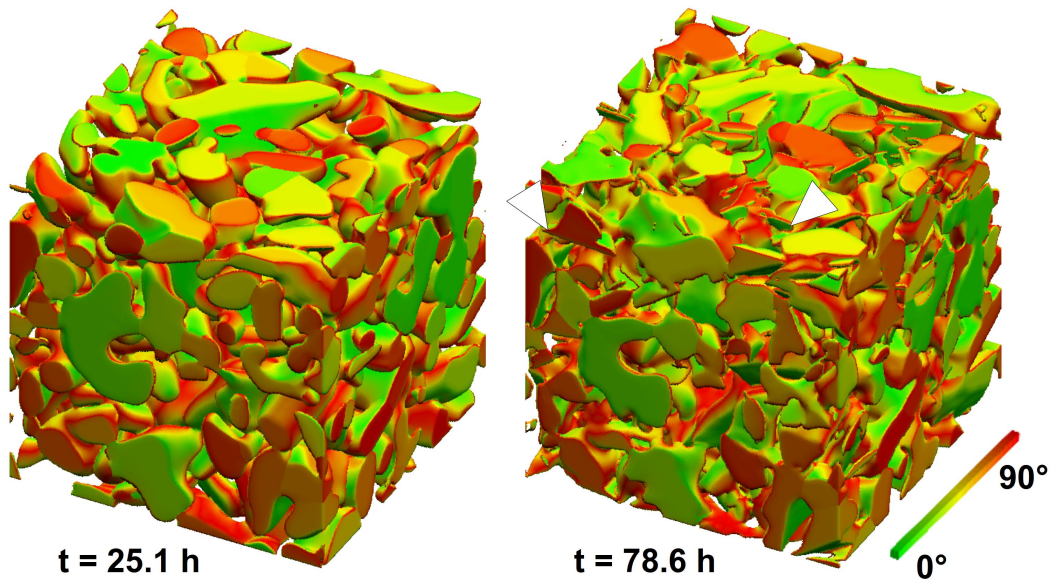


Figure 2.7: Times serie of the microstructural evolution. The colours represent the angle between the c-axis obtained from the DCT information and the normal to the interface: green represents basal faces, and red represents the surface parrallel to the c-axis. White arrowheads point out plate-like crystals formed at the end of the experiment, where consistency between orientation and morphology can be checked.

For further analysis, we introduce the parametrization represented in Figure 2.6. At a given point of the surface three vectors have importance in the physics: the vertical direction given by \mathbf{z} pointing upward which is the direction of the global

temperature gradient and of the macroscopic vapor flux, the normal at the interface \mathbf{n} taken here as pointing into the pore space, and the c-axis given by \mathbf{c} . We can then define three angles: $\alpha = (\mathbf{c}, \mathbf{n})$, $\beta = (\mathbf{z}, \mathbf{c})$ and $\gamma = (\mathbf{z}, \mathbf{n})$. Because we are only interested in the direction of \mathbf{c} , values range is $[0,90^\circ]$ for α and β , and $[0,180^\circ]$ for γ .

Figure 2.7 represents the microstructure with the interface colored by the angle α so that the basal faces ($\alpha = 0^\circ$) are green and the prismatic faces ($\alpha = 90^\circ$) are red. By looking particularly at the plates formed during the metamorphism we can observe that the orientation of the c-axis is consistent with their morphology.

2.3.2 Density

Representative Elementary Volume (REV) analysis for density was performed on absorption volumes at different times of the experiment, using cubic centered subvolumes of increasing sizes. The results are depicted on Figure 2.8.a, and show that the density reaches a constant value for cubes of edge about 2.34 mm. In order to complement the characterisation of the homogeneity, we computed the density of horizontal discs of the sample, centered on the vertical axis of the sample with diameter of 3.2 mm (so that it corresponds to the cubic REV of 2.34 mm edge) and one voxel (6.5 μm) high. This enables one to obtain a vertical density profile. The results are shown in Figure 2.8b. The high values on top and bottom correspond to

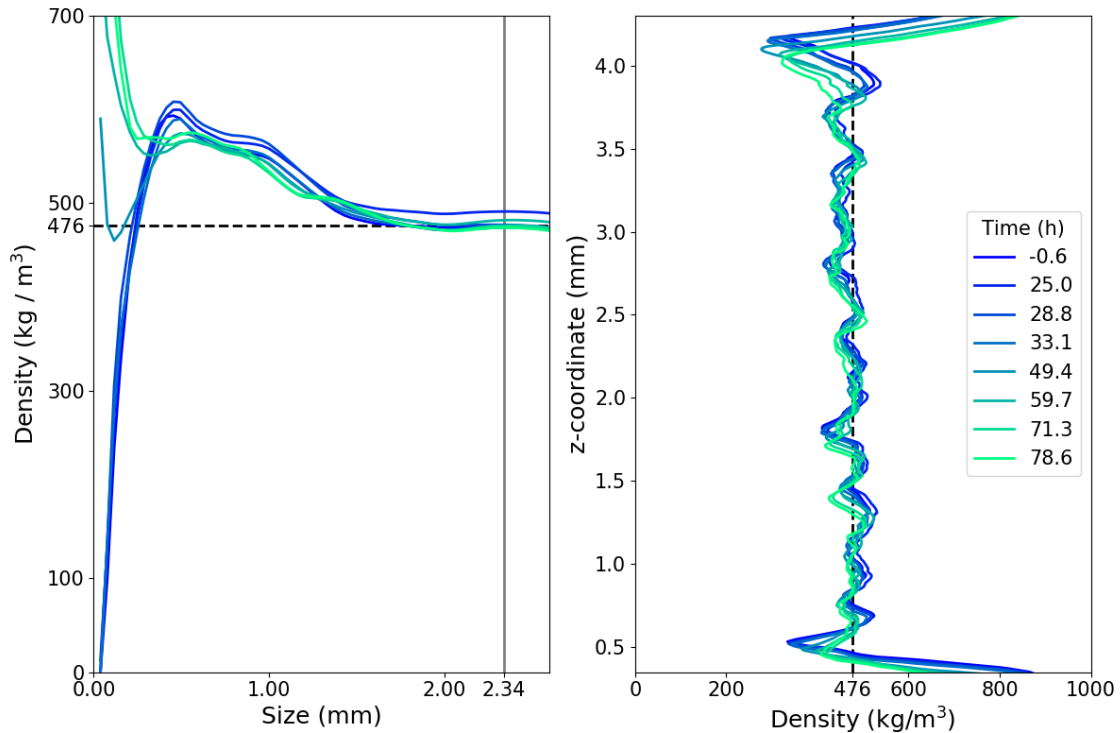


Figure 2.8: a): Representative Elementary Volume estimation for density, computed from centered cubic subvolumes of variable sizes. b): Vertical variation of density computed on centered discs of 1 voxel height and 3.25 mm in diameter.

ice lenses (917 kg m⁻³). Height and time fluctuations are visible, but the sample is

globally homogeneous in the vertical direction. We also computed the density for each absorption volume on a cubic REV of size 2.34 mm. The result is shown in Figure 2.9. We observe a constant density throughout the experiment at the initial value of 476 kg m^{-3} .

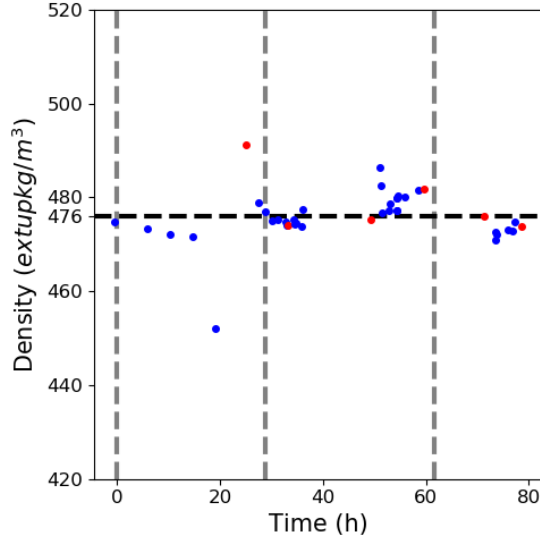


Figure 2.9: Evolution of density with time. The grey vertical lines represent the times of change of temperature conditions. Red dots correspond to times for which DCT information is available. The horizontal black dashed line represents mean density.

2.3.3 Specific Surface Area

First, REV for SSA were computed on centered cubic subvolumes of increasing sizes, at various times during the experiment. SSA computations were performed using VP projection algorithm [Flin *et al.*, 2005, 2011]. Figure 2.10 summarizes the results of this analysis. For all times, values are stable for subvolumes of size larger than 2 mm. So the REV of density (2.34 mm) can be chosen. Figure 2.11 shows evolution of SSA during the experiment. Starting at $18 \text{ m}^2 \text{ kg}^{-1}$, the SSA decreases slightly during the first 30 h and then increases more and more rapidly to reach about $20 \text{ m}^2 \text{ kg}^{-1}$.

2.3.4 Orientation tensor

Given the crystallographic orientation of each ice voxel, we can compute the second order orientation tensor [Fisher *et al.*, 1993; Riche *et al.*, 2013]:

$$\mathbf{a}^{(2)} = \frac{1}{N_i} \sum_{i=1}^{N_i} \mathbf{c}^i \otimes \mathbf{c}^i \quad (2.1)$$

with \mathbf{c}^i being the c-axis orientation of the i-th voxel in the volume, \otimes the tensor product and N_i the number of ice voxels. The orientation distribution is inscribed

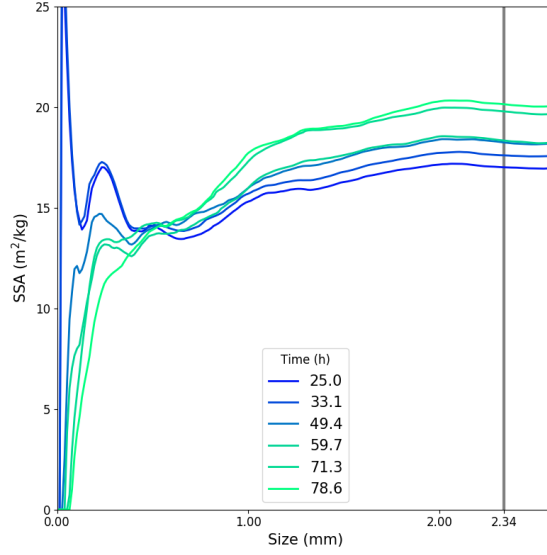


Figure 2.10: Specific Surface Area: REV estimation for different times. The vertical grey line represents the size of the REV volume taken for the remainder of the study.

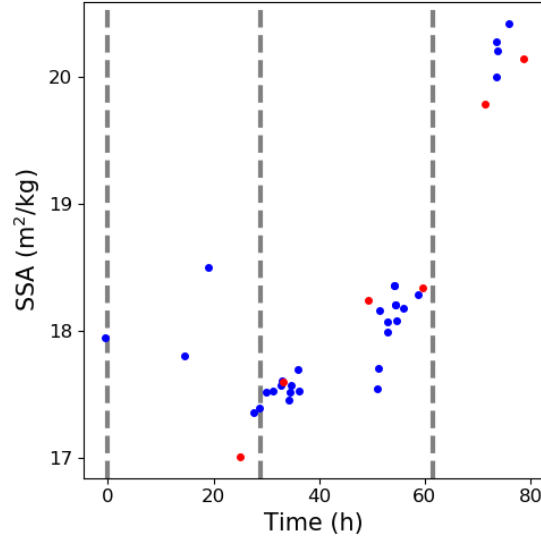


Figure 2.11: Evolution of the Specific Surface Area during the experiment. The grey vertical dashed lines represent the times of change of temperature conditions. Red dots correspond to times for which DCT information is available.

in an ellipsoid whose principal axes are given by the eigenvectors $(\mathbf{v}_1, \mathbf{v}_2, \mathbf{v}_3)$ of $\mathbf{a}^{(2)}$, and the length of the principal axis by its eigenvalues. Denoting the eigenvalues as a_1, a_2, a_3 with $1 > a_1 \geq a_2 \geq a_3 > 0$, we can identify 3 limit cases, defining 3 references of fabric.

- $a_1 > a_2 \simeq a_3$: Cluster-type fabric, majority of c axis in one direction (defined by \mathbf{v}_1)
- $a_1 \simeq a_2 > a_3$: girdle-type fabric, majority of c -axis in a plane (defined by \mathbf{v}_1

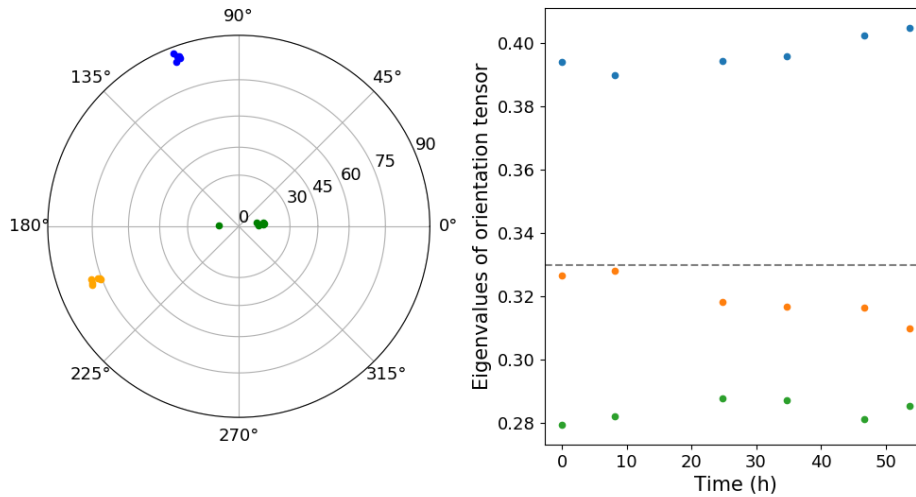


Figure 2.12: Evolution of the eigenvectors of the orientation tensors represented in pole figure with vertical axes as reference (left) and eigenvalues (right). Colors of dots for eigenvector on the left correspond to eigenvalue colors on the right. The grey dashed line represents value of 0.33, i.e. isotropy of the orientation tensor.

and \mathbf{v}_2)

- $a_1 = a_2 = a_3 = 1/3$: Isotropic fabric, same distribution in the three directions

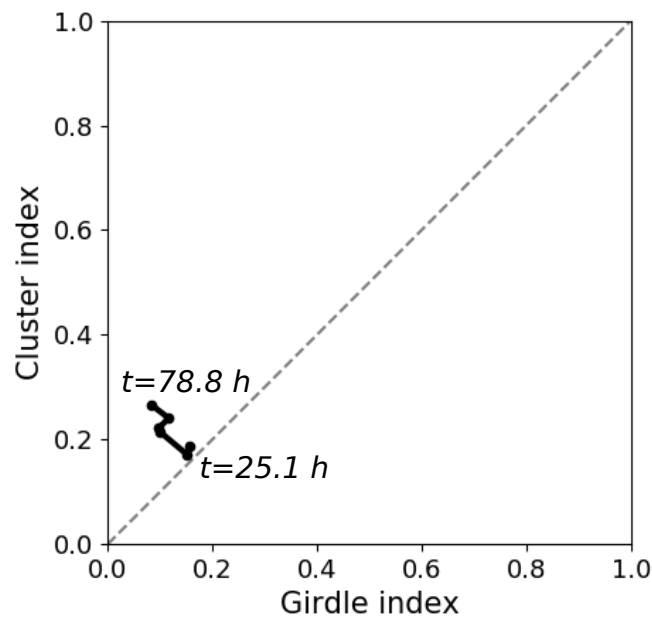


Figure 2.13: Cluster index versus girdle index for the different times indicated. Grey dashed line represent the $y=x$ line.

In order to evaluate the proximity of the measured distribution to those types, cluster index, girdle index and strength can be defined by $\ln(a_1/a_2)$, $\ln(a_2/a_3)$ and $\ln(a_1/a_3)$

respectively. The strength index equals 0 for a perfectly isotropic fabric. Figure 2.12 represents eigenvectors on the left panel, in pole figure representation, while the associated eigenvalues for the DCT images against time are shown on the right hand side. Eigenvalues lie in the range 0.279 to 0.405 without significant visible evolution over time. Eigenvectors are stable with time, one being parallel to temperature gradient, the two others being contained in the horizontal plane.

Figure 2.13 is a scatter plot of the cluster index against the girdle-index for the treated DCT volumes. The cluster index, girdle index and strength index are respectively 0.188, 0.156 and 0.343 at the initial stage and 0.266, 0.083 and 0.349 at the final stage, with mean values of 0.217, 0.117 and 0.335. Thus, the fabric is globally isotropic and stays isotropic during the evolution.

2.3.5 Pore size distribution

Pore size distributions were computed on absorption images using a sphere fitting algorithm. The results are shown for several times in Figure 2.14, with vertical lines denoting the mean of the corresponding distribution. Overall, the mean stays at about 190 μm and the distribution does not show any drastic evolution in shape. In particular, no trends are observable for the biggest pores, while a small trend is observable for the smaller ones. Indeed, the quantity of pores of size in the range 30 μm to 80 μm increases by about 1 %.

2.3.6 Relation between flux and grain orientation

The main objective of this study is to look at possible relations between local fluxes and crystalline orientation. In particular, we would like to test at the local scale the validity of orientation selective growth of grains under temperature gradient metamorphism.

From the 30 registered and segmented absorption images $(A_k)_{k \in \llbracket 1, 30 \rrbracket}$, we compute local interface speeds v_k where k is the index of the absorption image. At a given point of the surface of the volume $k \in \llbracket 1, 30 \rrbracket$ the normal \mathbf{n}_k was computed using the ADGF algorithm [Flin *et al.*, 2005]. Noting d_k^l the displacement of the interface along \mathbf{n}_k from A_k to A_l , we computed both d_k^{k+1} and d_k^{k-1} using an algorithm presented by Flin *et al.* [2018] whose principle is relatively close to the one presented by Krol and Löwe [2016]. Then local normal velocity v_k at the instant t_k of acquisition of A_k , was estimated using :

$$v_k = \begin{cases} \frac{d_k^{k+1}}{t_{k+1} - t_k} & \text{if } k = 1 \\ \frac{t_k - t_{k-1}}{t_{k+1} - t_{k-1}} \frac{d_k^{k+1}}{t_{k+1} - t_k} - \frac{t_{k+1} - t_k}{t_{k+1} - t_{k-1}} \frac{d_k^{k-1}}{t_k - t_{k-1}} & \text{if } k \in \llbracket 2, 29 \rrbracket \\ -\frac{d_k^{k-1}}{t_k - t_{k-1}} & \text{if } k = 30 \end{cases} \quad (2.2)$$

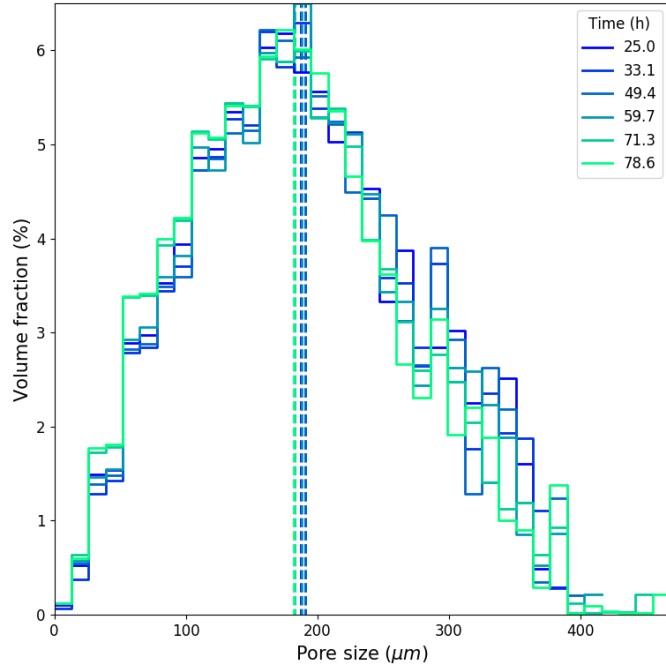


Figure 2.14: Pore size distribution, with 2 voxels = 13mm bin size computed using a fitting sphere algorithm. Vertical dotted lines represent the mean of the associated distribution.

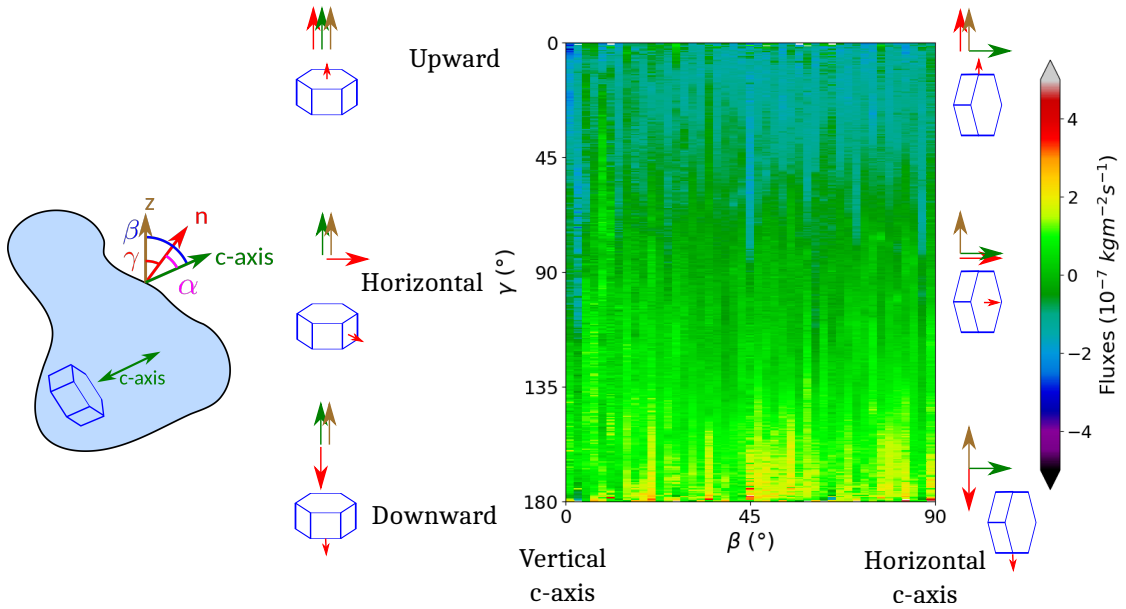


Figure 2.15: Interpretation of diagram of mean flux against (β, γ) .

From the normal velocity of the interface, the mass flux ϕ_k of vapor changing into ice can be computed using:

$$\phi_k = \rho_i \cdot v_k \tag{2.3}$$

Voxels were first classified depending on the values of α and γ in 2D bins. Then, a

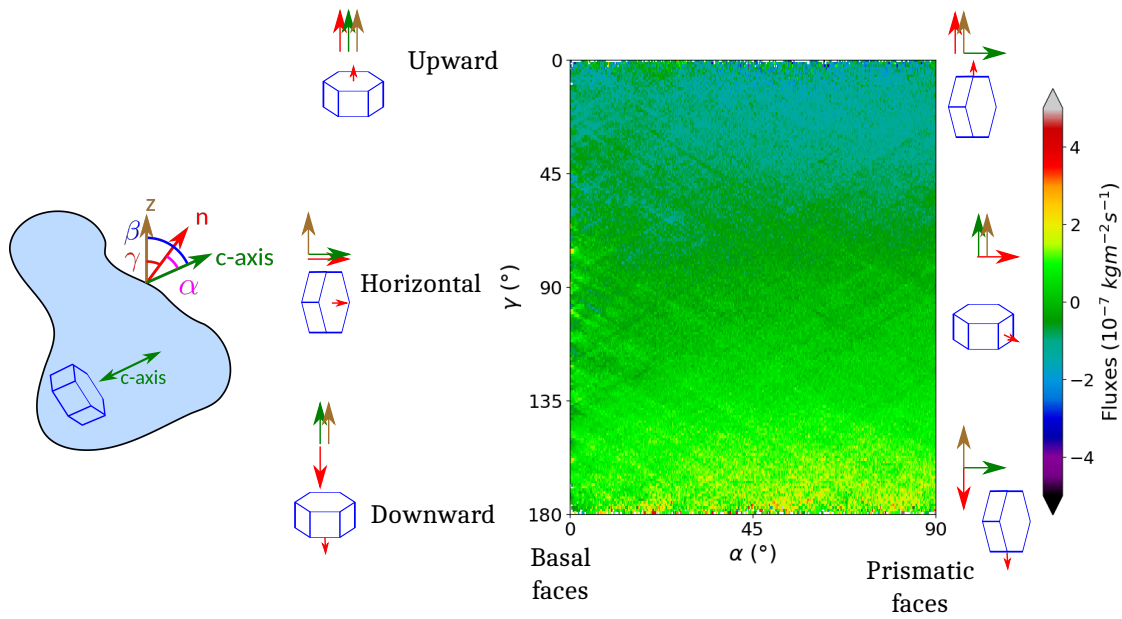


Figure 2.16: Interpretation of diagram of mean flux against (α, γ) .

mean flux value was computed for each bin. This enables us to represent a colormap of the mean fluxes against (α, γ) at the different times of the experiment. An example of this representation is given in Figure 2.16. The pixels on the right of the diagram represent prismatic faces ($\alpha = 90^\circ$) while the pixels on the left represent basal faces ($\alpha = 0$). The top diagram represent surfaces pointing upward ($\gamma = 0$), while the bottom of the diagram represent surfaces pointing downward ($\gamma = 180^\circ$), pixels at mid height of the diagram represent surfaces whose normals are horizontal ($\gamma = 90^\circ$). A similar representation can be done by representing the mean flux against (β, γ) (Figure 2.18). In that case, the right of the diagram represent grains with horizontal c-axis ($\beta = 90^\circ$) while the left of the diagram represent grains with vertical c-axis ($\beta = 0$).

Representations for all times of mean flux against (α, γ) are given in Figure 2.17, and against (β, γ) in Figure 2.18. At $t = 25.1$ h, from both figures, the absolute mean fluxes appear to be less than $10^{-8} \text{ kg m}^{-2} \text{ s}^{-1}$ in all cases. At $t = 33.3$ h, mean fluxes for $\gamma < 90^\circ$ are negative (denoting sublimation) and positive (deposition) otherwise. This is due to the fact that the mean vapor fluxes through the pore space are oriented upward: the faces whose normals point downward ($\gamma > 90^\circ$) catch vapor which deposits while the faces oriented upward sublimate.

In addition, we can observe a second variation depending on the value of α . Stronger rates of sublimation /deposition with absolute mean fluxes of $5 \cdot 10^{-7} \text{ kg m}^{-2} \text{ s}^{-1}$ are found for $\alpha > 45^\circ$. While there is no dependence on α for $\gamma = 90^\circ$, the closer γ gets to 0 or 180 the stronger is that dependence. Until $t = 78.8$ h, the same dependence on γ is observed, and the dependence on α has the same shape for $\gamma < 90^\circ$ while it is not visible for $\gamma > 90^\circ$. Globally, at all points of the diagram, the

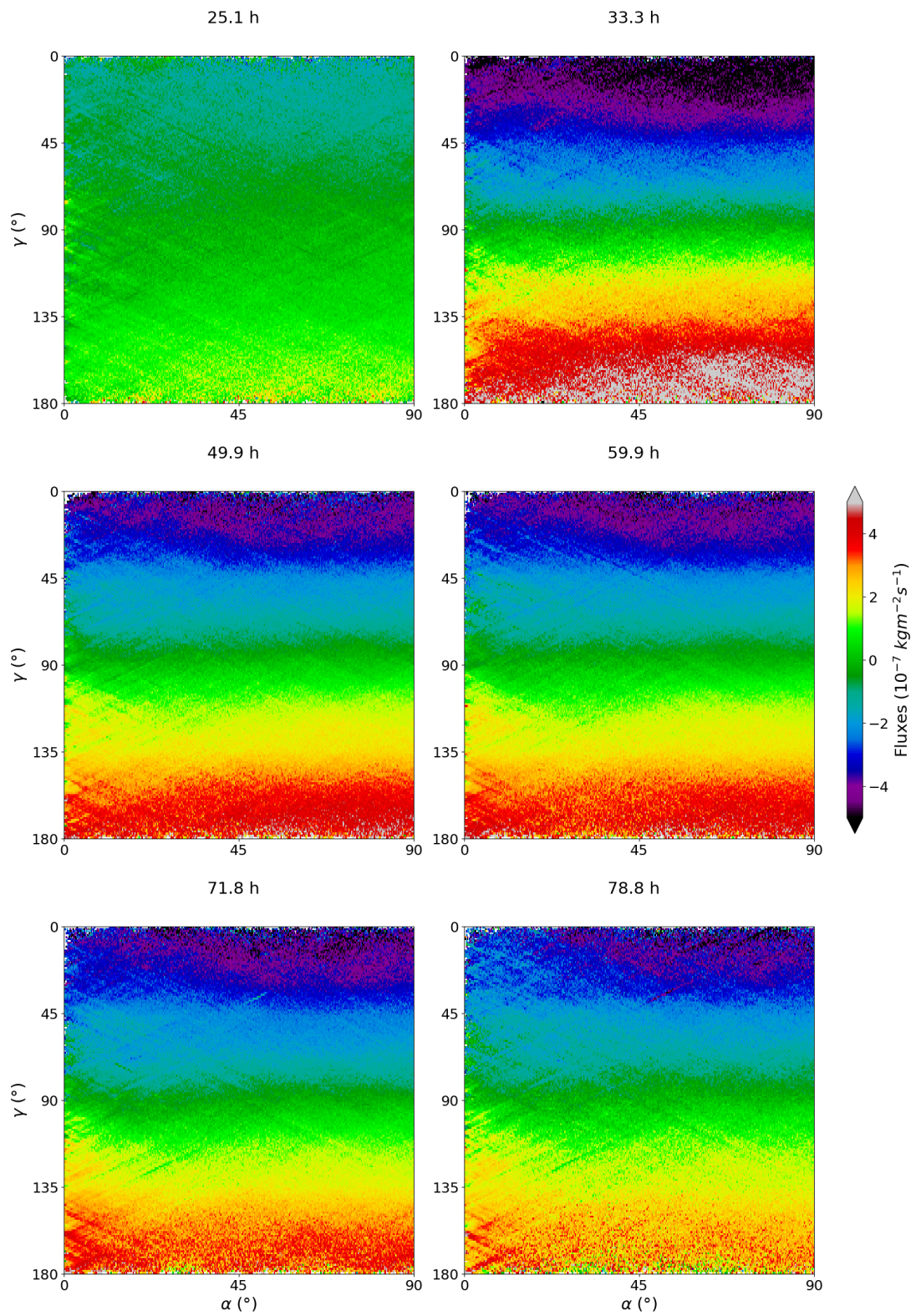


Figure 2.17: Mean fluxes against $\gamma = (\mathbf{z}, \mathbf{n})$ and $\alpha = (\mathbf{c}, \mathbf{n})$

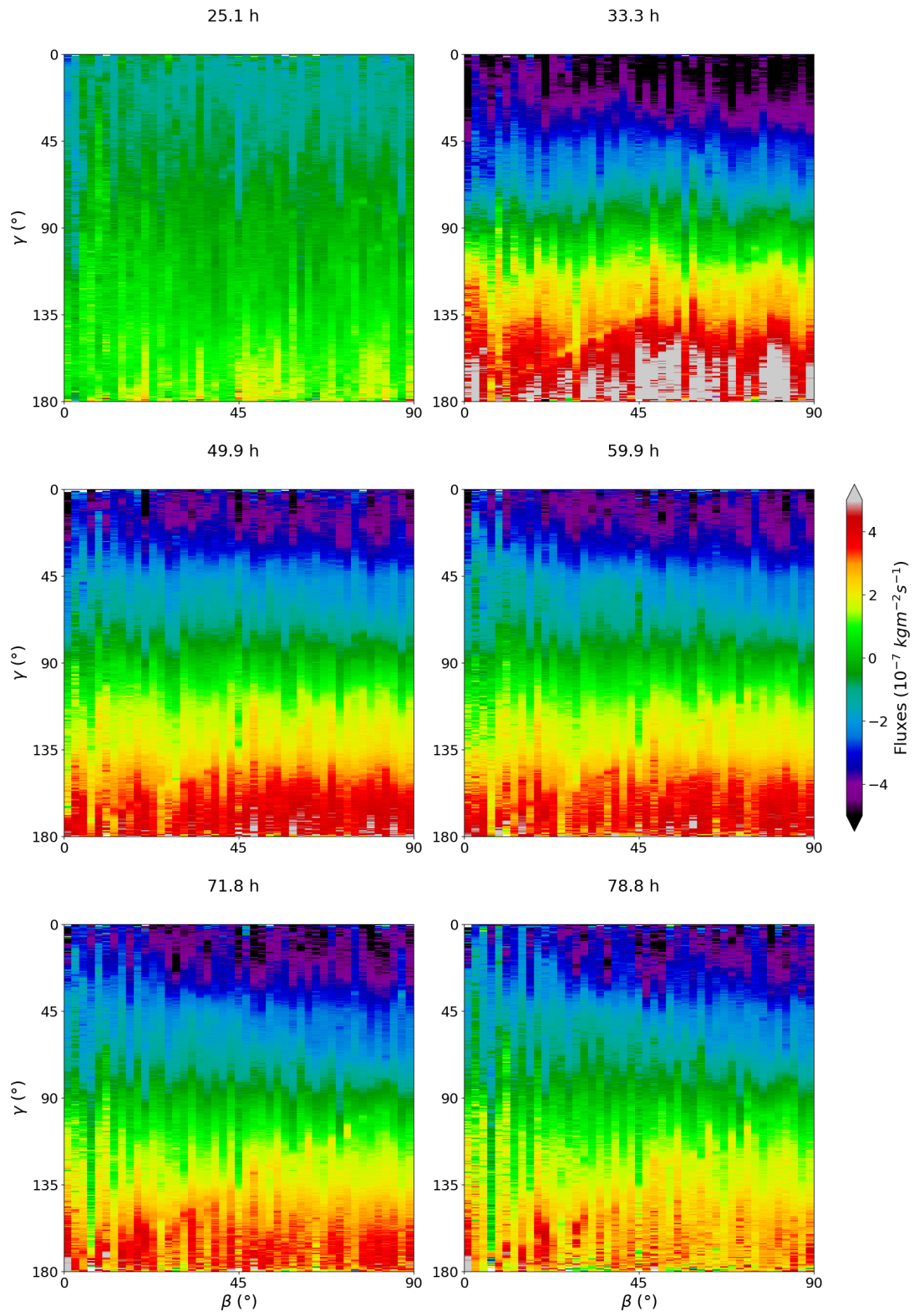


Figure 2.18: Mean fluxes against $\gamma = (\mathbf{z}, \mathbf{n})$ and $\beta = (\mathbf{z}, \mathbf{c})$

values are lower than at $t = 33.3$ h. The evolution between $t = 33.3$ h and $t = 78.8$ h is regular so that times $t = 49.9$ h, $t = 59.9$ h and $t = 71.8$ h are intermediate steps. The same observations can be made on Figure 2.18. The dependence on γ differentiates between faces subject to deposition and those subject to sublimation. For $t \geq 33.3$ h, voxels belonging to crystals with a c-axis in the horizontal plane, or close to this plane ($\beta \in [45^\circ, 90^\circ]$) are more active.

2.3.7 Example of evolution inside a small subvolume

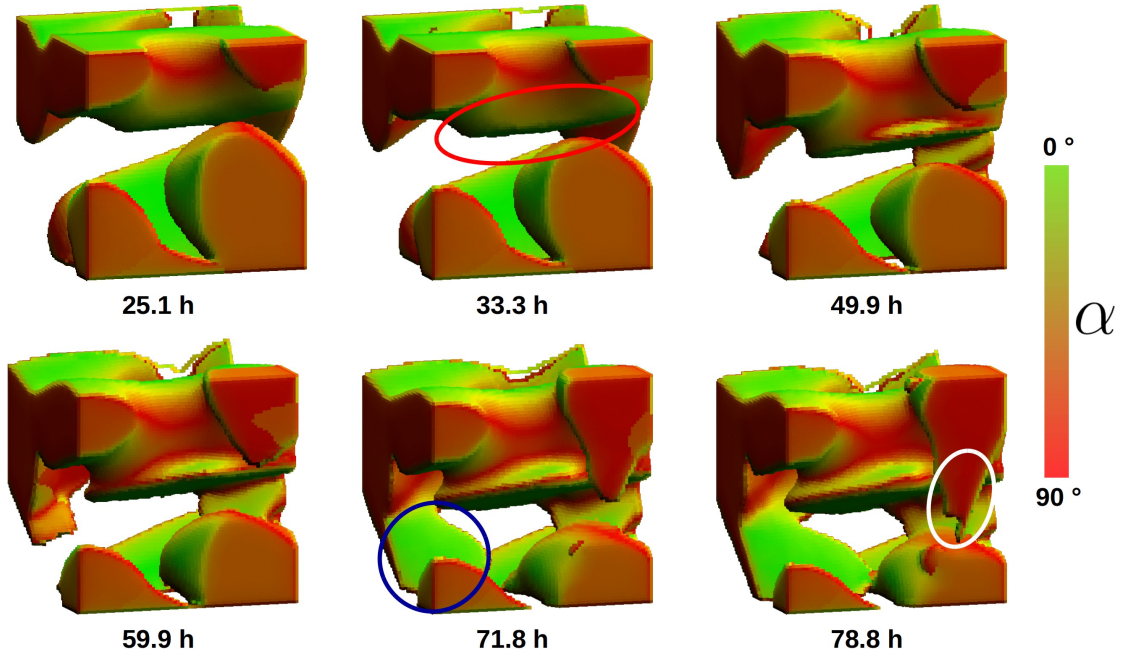


Figure 2.19: Example of evolution inside a small subvolume of $520 \mu\text{m}$. Colours refer to the α value, with green representing basal faces and red prismatic faces.

Figure 2.19 illustrates the various points observed from the data analysis. It shows the evolution of the microstructure inside a small cubic subsample of size $80 \text{ voxels} = 520 \mu\text{m}$. The color of the surface refers to α so that prismatic faces are represented in red and basal faces are represented in green. We can observe the formation of three faceted crystals, each with a different orientation. The one pointed out by the red ellipse is almost horizontal while the one pointed out by the white ellipse is almost vertical. The blue localised facet has intermediate orientation.

The horizontal plate is slowly evolving while the one pointed out by the blue circle develops very well. Also, we can see some interactions between the plates pointed out by red and white ellipses. In particular, at $t = 78.8$ h, we observe that the vertical plate grows at the expense of the horizontal one. Thus, while it is not a representative volume of the microstructure, this example illustrates well the observed trends on Figure 2.17 and 2.18.

2.4 Discussion

2.4.1 Fluxes and dependence on orientation

At $t = 25.1$ h, the fluxes and variations on fluxes are small. The temperature gradient of $17 \text{ }^\circ\text{C m}^{-1}$ is the smallest used. We conclude that in phase 1, metamorphism didn't act significantly due to small temperature gradient. This can be explained by the relatively high density of the sample of 476 kg m^{-3} . Indeed, it is known that high density snow requires higher temperature gradients [Akitaya, 1974; Marbouty, 1980; Pfeffer and Mrugala, 2002] and longer times of evolution to get visible modifications of the microstructure. Under a $52 \text{ K}^\circ\text{C m}^{-1}$ temperature gradient, the maximum values of the fluxes is of about $4 \cdot 10^{-7} \text{ kg m}^2 \text{ s}^{-1}$. Pinzer *et al.* [2012] computed a macroscopic flux of about $3.5 \cdot 10^{-7} \text{ kg m}^2 \text{ s}^{-1}$ for snow evolving under $49 \text{ }^\circ\text{C m}^{-1}$ temperature gradient at $-3.4 \text{ }^\circ\text{C}$. Flin and Brzoska [2008] computed the highest fluxes of about $1.6 \cdot 10^{-7} \text{ kg m}^2 \text{ s}^{-1}$ under $16 \text{ }^\circ\text{C m}^{-1}$. Thus, the present computed flux values are in very good agreement with this litterature.

As described in subsection 2.3.6, for $t = 33.3$ h, the most active points of the interface are for $\alpha > 45^\circ$. We think that corresponds to plates growing on grains, with prismatic faces being more active than basal faces. Indeed, from the definition of α , the prismatic faces correspond to $\alpha = 90^\circ$. Additionally, at the beginning of the experiment, the grain are typically rounded so that all values of α are equally represented in term of surface area. Since surfaces with $\alpha = 45^\circ$ which are high index orientations rougher at the molecular level, they have highest condensation coefficient and are more active. Moreover, in this experiment, grown plates were really thin: about 2-3 voxels thick, as a consequence, normals computed on the side of these structures were inaccurate, leading to several tens of degrees of uncertainty. These two effects explain why the highest fluxes are found in the range $\alpha \in 45^\circ$ to 90° and not just at $\alpha = 90^\circ$. So this observation is consistent with the mean temperature during the experiment, which was always higher or equal to -4° . Indeed, under that temperature condition, the kinetic coefficient is expected to be stronger on prismatic faces than on basal faces [Kuroda and Lacmann, 1982; Furukawa, 2015]. Correspondingly, from 2.18, most active faces correspond to crystals for which $\beta = 90^\circ$, i.e. with the c-axis in the horizontal plane. Following Adams and Miller [2003], this seems to confirm that kinetically favorably oriented crystals, in our case with basal faces oriented vertically and, thus, showing prismatic faces downward and upward, are indeed more active. At the end of the experiment, the fluxes at the interface globally decrease. We see three reasons for that: the first is that, the high index orientation (with $\alpha=45^\circ$) disappear as they grow. Secondly, after the important growth of plates between $t = 25$ h and $t = 33$ h, the growth, and globally the metamorphism slows down because of geometric interactions between grains. Finally, at the end of the experiment, the mean temperature was reduced, thus reducing globally the activity of the interface.

2.4.2 Independence on orientation for deposition

While, at $t = 33.3$ h, stronger activity for grains with c-axis close to the horizontal plane is clear, this progressively disappears on deposition surfaces. This suggests that at a certain point, growth intensity becomes less dictated by kinetics. We think that this may be explained by grain to grain interactions. At the beginning of phase 2, the microstructure has not evolved much, and a strong gradient triggers the growth of plates through the available pores. When the facets grow in the pore space between several grains, growth locally occurs if the temperature of the grain is lower than the average temperature of the grain in interaction with that pore. But, as the facet grows through the pores, it becomes closer and closer to another grain, and growth becomes more dependent on the local configuration of the microstructure, and less in relation with the macroscopic temperature gradient. So faceted grains develop well in pores and less efficiently after they have grown through the pores. This is similar to the conclusions from *Akitaya* [1974] on the necessity of pore space for growth. However, on the sublimating surfaces, as the interface moves away from the pore, such a phenomenon does not occur, and fluxes stay well dependent of orientation. While weakly marked, the slight increase in small pores occurrence in phase 3, seen on the pore size distribution (Figure 2.14), would be consistent with that explanation.

2.4.3 Uncertainties due to processing

As explained in section 2.2.3, a dilation step is required at the end of the processing route, in order to recover the orientation information missing due to dynamic diffraction. One can wonder if that could bias the Figures 2.17 and 2.18. When dilating the orientation information in one partially reconstructed grain, the correction is correct until the dilation front crosses a grain boundary. Beyond this, the correction is wrong. However, we assume the orientation difference between adjacent grains to be random. In consequence, that step affects the signal-to-noise ratio, which increases if the number of corrected voxels is higher than the number of errors. Errors are located in the vicinity of grain boundaries, and represent a small fraction of the analysed surface voxels and this implies no systematic error able to explain the observed trends. However, the improvement of the reconstruction assessing the problem of dynamic diffraction is of great interest, since it would increase the signal quality and permit other analyses. In particular, it seems crucial to properly study the grain boundaries. The problem of dynamic diffraction could be tackled by: i) improvement of diffraction spot thresholding and ii) modeling of the dynamic diffraction to reconstruct the grains from inhomogeneous intensities. The latter is a current subject of development of the technique.

2.4.4 Representativity

REV analysis for density and specific surface area shows that a 2.34 mm cubic subsample was representative of the volume sample as those quantities reached a plateau at that size. The dependence on γ is consistent with a global vertical temperature gradient, suggesting that possible edge-effects due to the small size of the sample were less important than temperature gradient.

The density of 476 kg m^{-3} is high for dry snow whose densities lies in the range 50 kg m^{-3} to 500 kg m^{-3} . *Akitaya* [1974] noticed the occurrence of hard depth hoar for a snow density $> 300 \text{ kg m}^{-3}$ exposed to temperature gradient of $39 \text{ }^\circ\text{C m}^{-1}$. *Pfeffer and Mrugala* [2002] observed formation of hard depth hoar for snow of 400 kg m^{-3} for temperature gradient $> 20 \text{ }^\circ\text{C m}^{-1}$ at a mean temperature of $-7 \text{ }^\circ\text{C}$ for 3 days. With a snow of density 230 kg m^{-3} , they did not observe the formation of hard depth hoar, and concluded it exist a critical density between those values. In the present experiment, the transition occurred in phases 2 and 3 where the temperature gradient was $52 \text{ }^\circ\text{C m}^{-1}$ with a mean temperature of $-2 \text{ }^\circ\text{C}$ and $-4 \text{ }^\circ\text{C}$ respectively. So results must be representative of the process of formation of hard depth hoar. In addition, both *Riche et al.* [2013] and *Calonne et al.* [2017] report no evolution of the fabric for the high-density snows, which would be consistent with the expectations that geometric-based competition between grains increases with density as the pore size decreases. However, the present results show that grain activity differences due to kinetics actually exist even at high density. So this suggests that while the effects exist, they are less important in the selection of growing grains at that density and are more likely to occur at lower density.

2.5 Conclusions

For the first time, DCT monitoring of a temperature gradient metamorphism experiment was carried out. A snow sample of rounded grains with initial density of 476 kg m^{-3} has been subject to a temperature gradient of $17 \text{ }^\circ\text{C m}^{-1}$ for 1 day then to a temperature gradient of $52 \text{ }^\circ\text{C m}^{-1}$ for 2 days at mean temperature of -2°C for 2 days, and -4°C for 1 day. Several points may be concluded from this experiment:

- The crystalline orientations have successfully been measured using DCT on about 900 growing and faceting grains.
- The local flux has been computed at each point of the interface, and the computed value is well consistent with previous studies.
- Analyses show that the first mass transfers were globally higher on grains with the c-axis close to the horizontal plane, for both sublimation and deposition, thus confirming the hypothesis of orientation selective metamorphism, even at high density.

- Fluxes become independent of orientation at longer times for deposition while differences remain for sublimation. We attribute this effect to grain to grain interactions, particularly present at that density, preventing further growth of crystals.

Additionally, this study also open new perspectives. Better accuracy on orientation, particularly at grains boundaries, can be obtained by a proper managment of dynamic diffraction, that occurs in ice, in the reconstruction process. Additionally, the observation of grain-selective activity at high density give confidence in the fact that this actually occurs in more general conditions. The present experiment could be repeated in various conditions to characterize this effect in more detail. Finally, the present data is necessary for models describing metamorphisms taking into account the crystalline nature of the ice.

From experiment to modeling

The crystalline orientation of the full 3D microstructure can be measured in a non-destructive manner (chapter 2). A better understanding of snow physics can be gathered from this data. However, to confirm interpretations of such experiments, it would be better to account for orientation and associated kinetics in a microstructural model running on a real 3D microstructure. Indeed, while curvature-driven metamorphism can be well reproduced based on tomographic data (see chapter 1), kinetics effects and faceting remain to be taken into account to model dry snow metamorphism in general thermal conditions.

Chapters 3, 4 and 5 are dedicated to that objective. The phase-field approach has been chosen for this task as it is a method of choice for the involved mathematical problem. The starting point is the model of *Kaempfer and Plapp* [2009], which couples phase change to heat and mass diffusion, and uses an isotropic kinetic coefficient. We focus here on extending that model with highly anisotropic kinetic coefficient with singular minimums in the way presented by *Uehara and Sekerka* [2003].

As the actual implementation of such a feature in a phase-field framework for tomographic data would require a massive development of both the mathematical formulation and the numerical implementation, the objective is here to evaluate first the potential of kinetic anisotropy to explain physical features of faceting, in the sharp interface limit. In particular, we study simple cases enabling comparison with experiments.

In chapter 3, we study the case of an air cavity migrating under a temperature gradient in a monocrystalline ice block. This enables us to test the faceting dependence on the phase change direction.

In chapter 4, we focus on the crystal habit. We use unequal singular minima in the kinetic coefficient to reproduce kinetic differences between basal and prismatic faces. The simulations are compared with an experiment of negative crystal growth, performed in 2015 at the Institute for Low Temperature Science.

In chapter 5, we present additional qualitative simulations. These include i) evolution of an isolated ice grain under a temperature gradient, and ii) 3D simulation of a the growth of negative crystal, without respecting phase-field convergence.

Kinetic faceting with phase-field model for snow metamorphism: validation on air cavity migration experiment.

Abstract

In the snowpack, the recrystallization of ice that occurs during metamorphism implies a shape transformation of the microstructure that critically influences snow properties. In particular, faceting of grains, which is the expression of the crystallographic structure, occurs under sufficiently strong temperature gradients, while they are rounded under weak temperature gradient conditions. The overall mechanism of snow metamorphism is well understood. However uncertainties remain in important details, including the description of the transition between regimes and the effect of the complex geometry of snow. Few models currently exist for that purpose. In that perspective, the phase-field method is a promising tool that has the advantage of simulating accurate physics on real geometries. Here, we use this technique to show the possibility of modeling kinetic faceting for ice-air systems that account for the basic anisotropy of the kinetic coefficient of ice surface. We show an experiment of an air cavity migrating in a monocrystalline ice block under a temperature gradient, and compare it with simulation. In both cases, the cavity migrates towards higher temperatures, conserving its volume and exhibiting a facet on the sublimating side while staying rounded on the depositing side.

3.1 Introduction

Once deposited on the ground, snow forms the snowpack, which is a porous medium made of ice, air containing water vapor and sometimes liquid water. The microstructure of this porous medium constantly evolves due to transformations called metamorphism so that different shapes can be observed depending on various factors such as the temperature gradient, the temperature, and the density or liquid water content [Colbeck, 1982]. Considering dry snow, when the temperature gradient is weak, fresh

snow evolves towards fine, rounded grains known as equilibrium forms. This results from the Kelvin effect: water vapor pressure at saturation is higher above convex surfaces than above concave surfaces. If the temperature is sufficiently homogeneous over the microstructure, the water vapor sublimates at the apex of snow grains, diffuses through the pore space and deposits in the concavities, thus resulting in equilibrium forms of snow [Colbeck, 1980]. These forms are generally fine grained and rounded. It's also known that ice, close to the melting point, presents a disordered state on the surface due to presence of quasi-liquid layer and temperature roughening [Libbrecht, 2005; Furukawa, 2015]. A plausible explanation in the shape transition of equilibrium forms is that, surface energy transits from isotropic to anisotropic as the smoothness of the surface increases when decreasing the temperature [Colbeck, 1982].

With increasing temperature gradient, the variation of water vapor pressure at saturation becomes more and more dominated by temperature differences so that the flow of water vapor is more and more oriented from warmer to colder parts of the air pores [Yosida *et al.*, 1955]. If the temperature gradient is strong enough, the water vapor flux is high and kinetic growth happens [Colbeck, 1983a]. This forms other types of snow called kinetic forms. Those can be classified in two categories, both presenting facets in a hexagonal symmetry. This is the expression of the hexagonal crystallographic structure of ice. The first are named faceted crystals [Fierz *et al.*, 2009], and consist of solid crystals with sharp edges and corners. At an even stronger gradient, the second category of kinetic forms, i.e. depth hoar, forms. They consist of hollow skeleton-type crystals than can be cup-shaped and striated [Akitaya, 1974; Colbeck, 1983a]. When low-density snow recrystallizes under a high temperature gradient for a long period of time, chains of depth hoar may form [Staron *et al.*, 2014], resulting in anisotropy of the macroscopic thermal conductivity [Sturm and Johnson, 1992]. Globally, faceted grains are weakly cohesive and form weak layers, thus playing an important role in dry-slab avalanche triggering mechanism [Schweizer *et al.*, 2003]. An exception is hard depth hoar, as reported by Akitaya [1974], which is cohesive depth hoar and may be formed at high temperature gradient and an initial density higher than 400 kg m^{-3} [Pfeffer and Mrugala, 2002].

Metamorphism of snow plays an important role in snow-air chemical interaction as it depends, beyond others, on size, shape and specific surface area (Dominé *et al.* [2003] and reference therein). It also strongly affects several snow properties. Although the main physics explained above are well understood, some uncertainties remain. The conditions of formation of the different snow types remain unclear. While it is known that temperature, snow types and density affect the critical temperature gradient value for the formation of faceted grains [Colbeck, 1987; Armstrong, 1981; Marbouty, 1980], a critical value of about $5 - 10 \text{ }^\circ\text{C m}^{-1}$ is retained, equilibrium forms being faceted under $-11 \text{ }^\circ\text{C}$ [Arons and Colbeck, 1995] with a transition between solid faceted crystals to depth hoar at about $20 \text{ }^\circ\text{C m}^{-1}$. In addition, such faceted grains are known to grow close to ice crusts: Colbeck and Jamieson [2001]

showed that a freezing buried wet layer tends to increase the faceted snow formation above itself. *Hammonds et al.* [2015] and *Hammonds and Baker* [2016] observed an amplification of the temperature gradient near the snow-ice interface, identified to be mainly due to increase in thermal resistance at that location. However, currently, no metamorphism model enables us to model the physics accurately in such a complex geometry. Finally, it's hypothesized that the interaction between the macroscopic temperature gradient direction and the crystal's orientations may favor growth of some crystals and so create anisotropy in the snow layers. Again, due to lack of data, only a few recent studies address this topic [*Riche et al.*, 2013; *Calonne et al.*, 2017], and many questions related to faceting of snow during metamorphism still remain unanswered.

On the theoretical side, it would be interesting to possess a model simulating microstructural evolution in general thermal conditions. *Miller and Adams* [2009] developed such a model, based on a simplified geometry consisting of spherical grains bounded by concave neck and stacked vertically. This modeling as the advantage of catching key features of metamorphism and linking it with microstructural parameters, and is able of treating weak gradient and temperature gradient metamorphism. However, to study the effects due to the complex geometry of snow like the local temperature gradient, chains formation, the dominance of the different types of grains, one needs to take the real geometry of the microstructure and its evolution into account. This is of even more interest due to the increasing availability of 3D microstructure geometry evolution data thanks to microcomputed tomography (μ CT) [*Brzoska et al.*, 1999a; *Pinzer et al.*, 2012; *Wang and Baker*, 2014; *Calonne*, 2014].

By considering heat conduction, vapor diffusion in the pore space, latent heat transfers, and writing down mass and energy conservation and phase change with Hertz-Knudsen formula, one find that this corresponds to a Stefan's problem. A similar problem is often found in alloy solidification, and is often solved using a phase-field method. Phase-field methods present several advantages: they enable us i) to rigorously solve Stefan's problem with model parameters being linked to physical properties, ii) to simulate the evolution of real complex geometries, and iii) to handle naturally topological changes. *Kaempfer and Plapp* [2009] developed a phase-field model taking into account heat conduction through ice and air, vapor diffusion in the air space, latent heat exchange and phase change, and the curvature effect on water vapor pressure at saturation. As a first step, this model does not take into account kinetics responsible for faceting. *Demange et al.* [2017] developed a phase-field model to simulate the different snowflake habits, the faceting being introduced with an anisotropy of the surface tension. *Yokoyama and Kuroda* [1990] presented a model for studying snow pattern formation and surface roughening. This model, based on boundary element method, allows the simulation of faceting of snow flakes using an anisotropic kinetic coefficient that presents sharp minima as

deduced by *Burton et al.* [1951]. Following this work, *Uehara and Sekerka* [2003] have demonstrated the possibility of kinetic faceting using phase-field methods.

In the present work, the phase-field model initially proposed by *Kaempfer and Plapp* [2009] is extended in order to describe the faceting observed during snow metamorphism under a high temperature gradient. Faceting is obtained by adding anisotropic kinetic coefficients with sharp minima as presented in *Uehara and Sekerka* [2003] which allows control of both the crystal growth in the basal plane (orthogonal with *c*-axis) and in the plane containing the *c*-axis independently. The proposed model is described in section 2. In section 3, the ability of the proposed model to reflect anisotropic faceting is presented through different simulations. Finally, qualitative comparisons between numerical simulations and experimental data are performed in the particular case of an air cavity migration in a monocrystalline ice block under a temperature gradient. This comparison is based on the analysis of 3D X-ray tomography images acquired during such an experiment.

3.2 Phase-field model

3.2.1 Isotropic model

In this section, the phase-field model initially proposed by *Kaempfer and Plapp* [2009] is summed-up. Let us consider a certain space domain Ω filled up with two complementary partitions Ω_a of air and Ω_i of ice forming a porous structure. The model consists of descriptions of three physical processes: diffusion of water vapor in the air, thermal conduction through the domain, and the phase change at the ice-air interface Γ .

Denoting κ_a and κ_i as the thermal conductivities ($\text{W m}^{-1} \text{K}^{-1}$) of air and ice respectively, C_a and C_i as the thermal capacities ($\text{J m}^{-3} \text{K}^{-1}$), D_v the diffusivity ($\text{m}^2 \cdot \text{s}^{-1}$) of water vapor in air, ρ_v the water vapor density (kg m^{-3}) in air, ρ_i the ice density (kg m^{-3}), T the temperature (K), and L the latent heat of sublimation (J m^{-3}). The first two processes are described by the following set of equations:

$$\frac{\partial \rho_v}{\partial t} = D_v \Delta \rho_v \quad \text{on } \Omega_a \quad (3.1)$$

$$C_a \frac{\partial T}{\partial t} = \kappa_a \Delta T \quad \text{on } \Omega_a \quad (3.2)$$

$$C_i \frac{\partial T}{\partial t} = \kappa_i \Delta T \quad \text{on } \Omega_i \quad (3.3)$$

$$\kappa_i \nabla T \cdot \mathbf{n} = \kappa_a \nabla T \cdot \mathbf{n} + Lv \cdot \mathbf{n} \quad \text{on } \Gamma \quad (3.4)$$

$$D_v \nabla \rho_v = \rho_i \mathbf{v} \cdot \mathbf{n} \quad \text{on } \Gamma \quad (3.5)$$

Equation (3.1) is the diffusion equation of water molecules in the pore space. Equations (3.2) and (3.3) correspond to the heat equation in the air and ice phase, respectively. Equations (3.4) and (3.5) describe the energy and mass conservation

conditions at the air/ice interface. At the air/ice interface, the normal velocity (v_n) of the interface due to the phase change is given by the Hertz-Knudsen equation:

$$v_n = \mathbf{v} \cdot \mathbf{n} = \beta \left(\frac{\rho_v - \rho_{vs}(T)}{\rho_{vs}(T)} - d_0 K \right) \quad (3.6)$$

where $\rho_{vs}(T)$ is the saturation density (kg m^{-3}) of water molecules in air at a temperature T over a flat surface, d_0 is the capillary length (m) of the ice, K is the mean curvature, and β is the kinetic coefficient (m s^{-1}) which measures the ability of the water molecules to be incorporated in the crystal. The $d_0 K$ term accounts for the Kelvin effect. Note that in phase-field literature [Kaempfer and Plapp, 2009; Echebarria et al., 2004; Karma and Rappel, 1998], β is introduced as $\sigma = \beta v_n$ where σ is the supersaturation. However, in the crystal growth literature [Yokoyama and Kuroda, 1990; Furukawa, 2015], the kinetic coefficient is defined from $v_n = \beta \sigma$. Here, the second notation is used. To describe attachment kinetics, the sticking or deposition coefficient α is often employed. This coefficient is the probability for a water molecule hitting the surface of the solid to be incorporated to the crystal, and so, ranges from 0 to 1. α and β are linked by the relation:

$$\beta = \alpha \frac{\rho_{vs}(T)}{\rho_i} \sqrt{\frac{k_B T}{2\pi m}} \quad (3.7)$$

m is the mass (kg) of a water molecule, and k_B is Boltzmann's constant. Finally, the water vapor density at saturation over a flat surface can be expressed with Clapeyron's equation [Colbeck, 1993]:

$$\rho_{vs}(T) = \rho_{vs}^{\text{ref}}(T^{\text{ref}}) \exp\left(\frac{Lm}{\rho_i k_B} \left(\frac{1}{T^{\text{ref}}} - \frac{1}{T}\right)\right) \quad (3.8)$$

where T^{ref} is a reference temperature (K), and $\rho_{vs}^{\text{ref}}(T^{\text{ref}})$ is the water vapor density at saturation at temperature T^{ref} .

Equations (3.1) to (3.5) define a system of equations of unknowns ρ_v , T and v_n and correspond to a Stefan's problem. In the following, a phase-field method is used to solve this problem. The phase-field method consists in defining an equivalent problem on a unique domain Ω on which the two phases will be differentiated by a new unknown scalar field ϕ , which will serve as an indicative function and so will be called the phase-field. This new problem is set up so that its solution is a good approximation to the Stefan's problem. The phase-field ϕ verifies the following properties:

- ϕ is close to 1 in the ice phase
- ϕ is close to -1 in the air phase
- The level set $\phi = 0$ represents the ice-air interface Γ

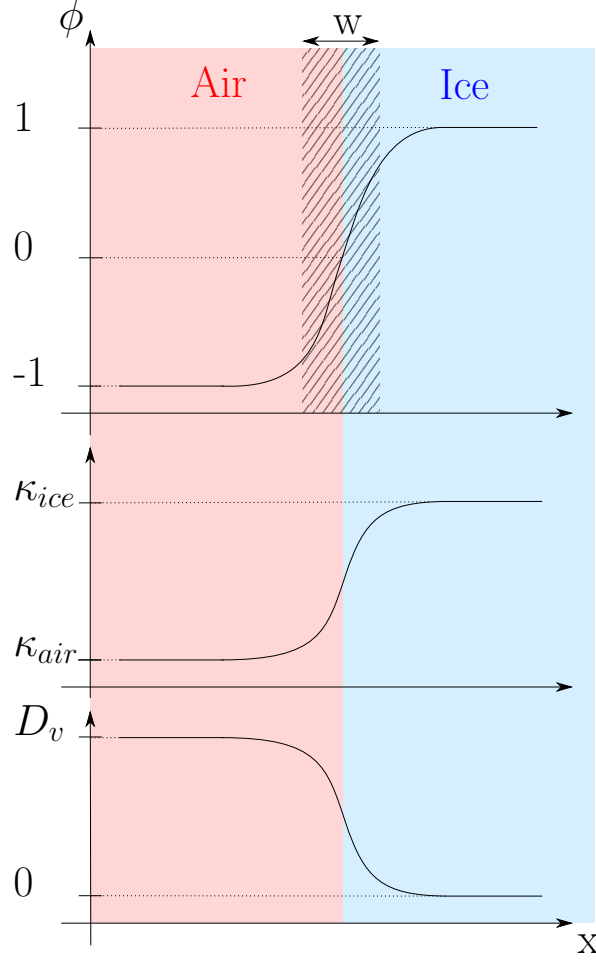


Figure 3.1: Typical evolution of the phase-field nearby the interface (top), and associated evolution of material properties evolution, e.g.: thermal conductivity (middle) and molecular diffusivity (bottom).

- ϕ varies rapidly and monotonically between -1 and 1 only on a small thickness W around Γ

Because only one domain is present, the material properties are introduced through continuous functions of ϕ as follows:

$$D(\phi) = D_v \frac{1 - \phi}{2} \quad (3.9)$$

$$\kappa(\phi) = \kappa_a \frac{1 - \phi}{2} + \kappa_i \frac{1 + \phi}{2} \quad (3.10)$$

$$C(\phi) = C_a \frac{1 - \phi}{2} + C_i \frac{1 + \phi}{2} \quad (3.11)$$

and a density variable needs to be defined on the whole domain:

$$\rho(\phi) = \rho_i \frac{1 + \phi}{2} + \rho_v \frac{1 - \phi}{2} \quad (3.12)$$

Similarly, a density at equilibrium can be defined:

$$\rho_{eq}(\phi, T) = \rho_i \frac{1 + \phi}{2} + \rho_{vs}(T) \frac{1 - \phi}{2} \quad (3.13)$$

For simplicity, the model is formulated in terms of a dimensionless variable (u) for the water vapor concentration:

$$u = \frac{\rho(\phi) - \rho_{eq}(\phi, T^{ref})}{\rho_i} \quad (3.14)$$

and

$$u_{eq}(T) = \frac{\rho_{vs}(T) - \rho_{vs}(T^{ref})}{\rho_i} \quad (3.15)$$

According to these definitions, it can be shown that equations (3.1) to (3.5) are equivalent to the following phase-field modeling:

$$\tau \frac{\partial \phi}{\partial t} = W^2 \Delta \phi + (\phi - \phi^3) + \lambda [u - u_{eq}(T)] (1 - \phi^2)^2 \quad (3.16)$$

$$C(\phi) \frac{\partial T}{\partial t} = \nabla [\kappa(\phi) \nabla T] + \frac{L}{2} \frac{\partial \phi}{\partial t} \quad (3.17)$$

$$\frac{\partial u}{\partial t} = \nabla [D(\phi) \nabla u] - \frac{1}{2} \frac{\partial \phi}{\partial t} \quad (3.18)$$

where τ and λ are a relaxation time and a coupling constant between the phase-change and supersaturation, defined as:

$$\tau = \frac{W^2}{\beta d_0} \quad (3.19)$$

$$\lambda = \frac{5\sqrt{2}}{8} \frac{\rho_i}{\rho_{vs}} \frac{W}{d_0} \quad (3.20)$$

where W is a model parameter which is a measure of the thickness of the diffuse interface. Equation (3.16) describes the phase change, the first two terms correspond to the fundamental Allen-Cahn equations and model equilibrium profile of the phase-field ϕ at the interface. The third term is the driving term due to dimensionless supersaturation $u - u_{eq}$. Equation (3.17) describes heat conduction and latent heat transfers. Equation (3.18) represents water vapor diffusion and mass conservation at the interface.

Physically, the interface between the phases is sharp and introducing a diffuse interface is an approximation. However, considering W a small parameter, and performing asymptotic analysis, it can be shown [Almgren, 1999; Ramirez et al., 2004] that the solutions of system (3.16) - (3.17) - (3.18) verify the conditions (3.1), (3.2), (3.3), (3.4) and (3.5) up to a $\mathcal{O}(W)$ term. In other words, the solution of the phase-field problem is a good approximation of the solution of the Stefan's problem as long as W is small enough. With $\beta = 2 \cdot 10^{-6} \text{ m s}^{-1}$ and $\rho_{vs}/\rho_i = 2 \cdot 10^{-6}$, it can be shown that the interface thickness W must be smaller to the following characteristic lengths:

$$\frac{\rho_{vs}}{\rho_i} \frac{1}{\beta} \frac{\kappa_a}{C_a} = 7 \cdot 10^{-6} \text{ m} \quad , \quad \frac{\rho_{vs}}{\rho_i} \frac{1}{\beta} \frac{\kappa_i}{C_i} = 1 \cdot 10^{-6} \text{ m} \quad , \quad \frac{\rho_{vs}}{\rho_i} \frac{1}{\beta} D_v = 2 \cdot 10^{-5} \text{ m} \quad (3.21)$$

According to Kaempfer and Plapp [2009], two more conditions need to be fulfilled so that the method remains valid: first, the interface thickness must be smaller than

radius of curvature $1/K$ in the microstructure. For snow, this would be of the order 10^{-4} m. Secondly, the asymptotic analysis is valid if ϕ is close to equilibrium. τ being the relaxation time of equation (3.16) and W the interface thickness, this implies that $v_n \ll W/\tau v$ where v_n is the normal interface velocity. This corresponds to:

$$v_n \ll \frac{\beta d_0}{W} = 5 \cdot 10^{-9} \text{ m s}^{-1} \quad (3.22)$$

with $\beta = 2 \cdot 10^{-6} \text{ m s}^{-1}$ and $W = 5 \cdot 10^{-7} \text{ m}$. This value correspond to a scale of speed at which the model may start to behave unphysically for the considered problem.

3.2.2 Anisotropic kinetic coefficient

Considering the surface diffusion for molecules, *Burton et al.* [1951] demonstrated that the kinetic coefficient exhibits a strong anisotropy, with a narrow minimum, because singular faces are molecularly smooth while other orientations present a much higher step density. *Yokoyama and Kuroda* [1990] used the expression of the kinetic coefficient obtained by *Burton et al.* [1951] to study pattern formation of snow crystals along with surface roughening, by the mean of boundary element method. *Uehara and Sekerka* [2003] used a phase-field model, that considered both an isotropic interfacial energy and an anisotropic kinetic coefficient. Those authors studied two expressions for the kinetic coefficient. Both with narrow minima but the first with smooth, derivable minima, and the second with sharp minima, of the form of the function obtained by *Burton et al.* [1951]. They showed that the phase-field approach enables the development of the kinetic Wulff shape with flat facets using such expressions. According to these previous works, the kinetic coefficients β_b and β_c , which allow the faceting in the basal plane (orthogonal to the c-axis) and in an orthogonal plane including the c-axis, are written:

$$\beta_b(\theta) = \beta_m \left[\delta + (1 - \delta) \tanh \left(\frac{k}{|\tan(3\theta)|} \right) \right] \quad (3.23)$$

$$\beta_c(\theta) = \beta_m \left[\delta + (1 - \delta) \tanh \left(\frac{k}{|\tan(2\theta - \frac{\pi}{2})|} \right) \right] \quad (3.24)$$

The evolution of these kinetic coefficients is presented in Figure 3.2. β_m is the maximum kinetic coefficient. δ is the ratio of the kinetic coefficient for the singular faces with β_m . k is a narrowness parameter of the minimum, which can be linked to step height and the mean surface diffusion distance of a molecule on the surface. Orientation of the maximum corresponds to the orientation of singular faces. Note that with expression (3.23) all minima correspond to prismatic faces, while with expression (3.24), if the c-axis is oriented at $\theta = \pi/2$, minima at $\pm\pi/2$ correspond to basal faces and minima at 0 or π correspond to prismatic faces, This expression assumes an equal kinetic coefficient for basal and prismatic faces. As a consequence,

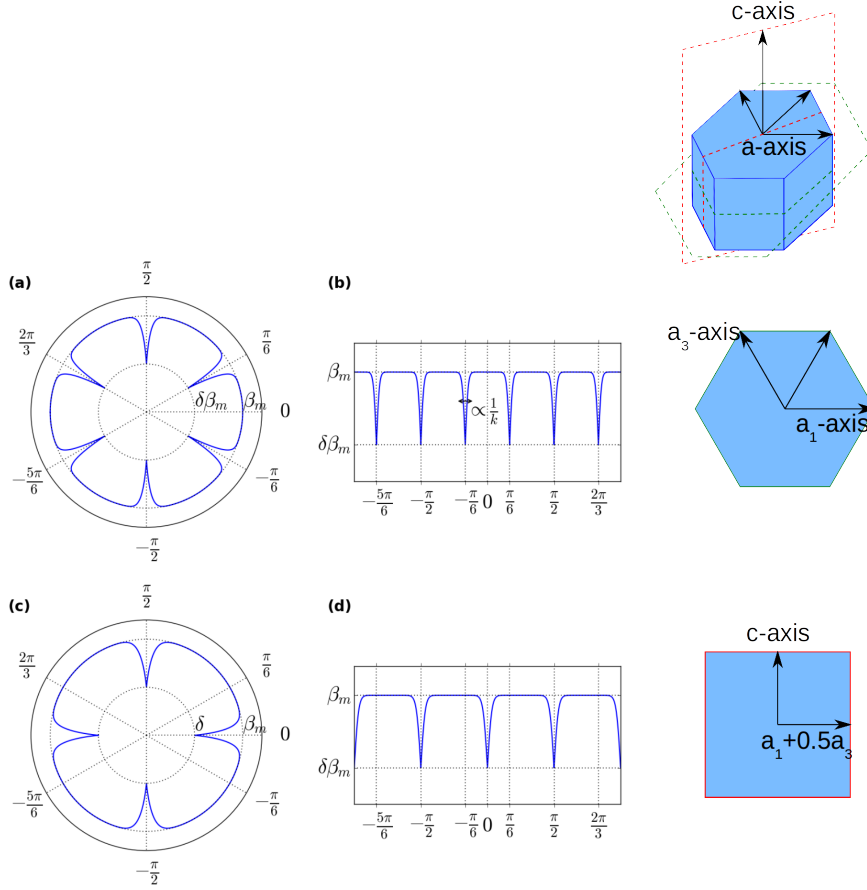


Figure 3.2: Plots of functions used for describing kinetic anisotropy for a plane orthogonal with c-axis ((a) and (b)) or for parallel to c-axis ((c) and (d)). Polar representations are depicted on the left and cartesian orientation on the center. β_m is the maximum kinetic coefficient, $\delta\beta_m$ the minimum kinetic coefficient, corresponding to singular faces and k is a narrowness parameter.

equation (3.19) becomes a function of θ , i.e of the orientation of the local normal at the interface becomes:

$$\tau(\theta) = \frac{W^2}{\beta(\theta)d_0} \quad (3.25)$$

and θ is computed from the partial derivative of ϕ with:

$$\theta = \arctan\left(\frac{\partial_r \phi}{\partial_z \phi}\right) \quad (3.26)$$

where ∂_r and ∂_z denote the local partial derivatives along radial and vertical directions respectively.

One has to pay attention to the fact that conditions (3.21) and (3.22) are still verified for all values of β . In our simulations, we will use $\beta_m = 2 \cdot 10^{-6} \text{ m s}^{-1}$ and $\delta = 0.1$. The former condition remains $W \ll 10^{-6} \text{ m}$, while the latter becomes $v_n \ll 2 \cdot 10^{-10} \text{ m s}^{-1}$.

In order to illustrate the effects of the anisotropy of the kinetic coefficient, simple 2D negative crystal formation simulations have been performed. Similarly

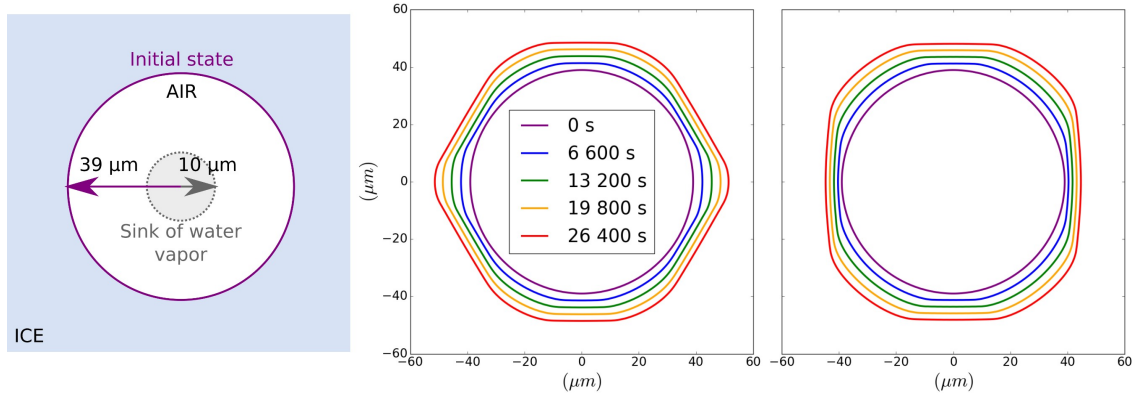


Figure 3.3: Illustrative 2D plane negative crystal formation by vacuum pumping simulation. Left: representation of the initial state of the circular cavity of radius $39 \mu\text{m}$, a sink of water vapor of $0.3 \text{ kg m}^{-3} \text{ s}^{-1}$ is imposed on an inner circle of radius $10 \mu\text{m}$. Middle and right: iso-0 contour lines of phase-field ϕ at different times of evolution for the two different β functions: (3.23) on the left, (3.24) on the right. Parameters for simulation were $\beta_m = 2 \cdot 10^{-6} \text{ m s}^{-1}$, $\delta = 0.1$ and $k = 1$.

to experiments presented by *Knight and Knight* [1965] and *Furukawa and Kohata* [1993], this consists in forcing sublimation of ice in an air cavity by the introduction of a sink of water vapor. As a consequence, the cavity grows and becomes faceted. The problem is as follows: an initial circular cavity of radius $39 \mu\text{m}$ is created in an ice block. The temperature is set to -4°C on boundaries and as initial condition. The dimensionless concentration u is initialised to its value at equilibrium u_{eq} . Then, a sink of water vapor of $0.3 \text{ kg m}^{-3} \text{ s}^{-1}$ is imposed over a disk of radius $10 \mu\text{m}$. Figure 3.3 represents the evolution of the interface in two cases corresponding to the two kinetic coefficient functions presented in 3.2.2: the first case corresponds to a simulation in a basal plane; the second case corresponds to a simulation in a plane parallel to the c -axis. Simulations were performed using $k = 1$ and the interface thickness was set to $W = 5 \cdot 10^{-7} \text{ m}$.

As expected, Figure 3.3 shows that the ice sublimates and progressively forms flat facets whose normals correspond to the singular directions of the anisotropic kinetic coefficient. The edges of facets then become sharper and sharper until a sufficiently strong curvature is attained so that Kelvin effect compensates kinetic faceting at those points.

3.3 Experiment

In order to test that model, we compared it to an experiment of migration of an air cavity under a temperature gradient in a monocrystal. This situation has the advantage of implying the same physics as snow temperature gradient metamorphism: the gradient of temperature creates a gradient of water vapor at saturation inside

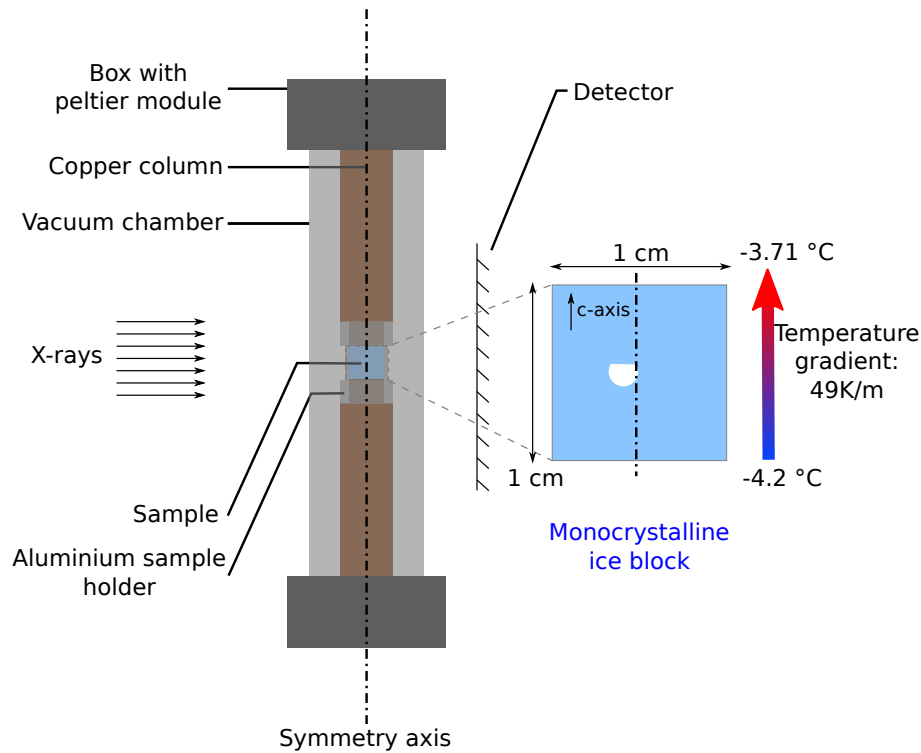


Figure 3.4: Schematic of the experimental setup. The sample is confined in aluminium sample holder. Its top and bottom temperature is controlled using a peltier module through copper columns. Insulation from room temperature is via a vacuum chamber. The c-axis and temperature gradient are vertical.

the cavity. So, the phase change happens on both sides in order to re-establish equilibrium, while diffusion tends to equalize the water vapor concentration inside the cavity. As a result, water molecules are transported from the warm towards the cold side and the cavity migrates in the direction of the temperature gradient. Such an experiment has the advantage that it involves a very simplified geometry, which permits focusing on the effect of kinetic anisotropy on the cavity, and, in particular, on the formation of facets. The experiment consists of imposing a temperature gradient to a monocrystalline ice block of known orientation containing an air cavity and following its evolution using X-ray micro-computed tomography.

Large ice monocrystals have been first grown from demineralized water following an approach similar to that described by *Baruchel et al.* [2013]. After freezing, we chose a cavity of appropriate size in a large monocrystalline zone. A cylinder of height and diameter 1 cm was machined so that the c-axis was oriented along the axis of revolution. The temperature of the sample was controlled using the CellDyM cryogenic cell (see Figure 3.4 and *Calonne et al.* [2015]). The sample was inserted into an aluminium sample holder, and the temperature on each basal face of the cylinder was controlled by a Peltier module, through copper columns. Because the tomograph operates at room temperature, a vacuum chamber is used around the sample to ensure a good thermal insulation of the sample. Initially, the sample was

cooling from -20°C to -4°C over 2 h. Then, the temperatures on sample's boundaries were set to -3.71°C and -4.2°C , which corresponds to a temperature gradient of $49^{\circ}\text{C m}^{-1}$ over the sample.

Data acquisition was performed with a laboratory tomograph (3SR Lab, RX Solutions) at $7.43\ \mu\text{m}$ of resolution. 23 scans have been done for 112 h of evolution under temperature gradient. After reconstruction of 3D images, several image processing methods have been applied. First, ring artefacts were filtered. Then images were registered so that displacement over time can be computed. Finally, the segmentation was performed using the energy-based method of *Hagenmuller et al.* [2013]. This results in a time series of 21 binary images describing the evolution

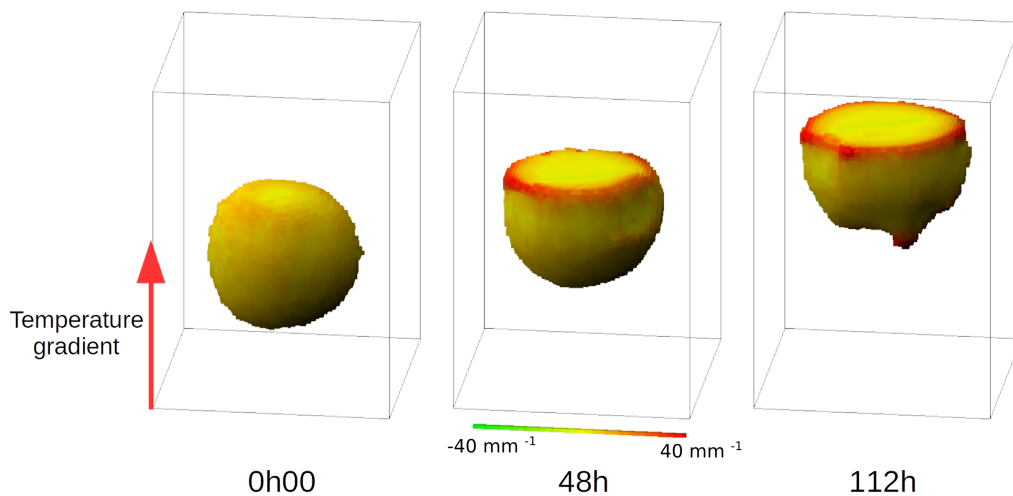


Figure 3.5: Evolution of the cavity in monocrystalline ice block under $49^{\circ}\text{C m}^{-1}$. Colors represent mean curvature of the ice-air interface as described by the colorbar. Frame box is $639 \times 453 \times 453\ \mu\text{m}^3$.

of the cavity (Figure 3.5). On the Figure, the colors represents mean curvature computed using a divergence approach [*Flin et al.*, 2004, 2005; *Calonne*, 2014]. At the initial state, the cavity is almost spherical with homogeneous curvature all over the surface. With increasing time, the cavity migrates towards the warmer boundary, and a facet develops on top, while the bottom stays rounded. In the second part of the evolution, a protuberance appears on the bottom of the cavity forming a narrow pore which does not advance as fast as the rest of the cavity and lags behind. Prismatic facets are weakly marked, so that the top of the cavity has an almost cylindrical shape, while the bottom remains quite spherical. Indeed, we can observe only two small prismatic faces at the end of the experiment.

In addition to those observations, we computed four global quantities to describe the overall geometrical evolution of the cavity: the position of the center of mass, its volume, the principal inertia momenta, and the angles α between vertical and principal axes of inertia. When using tomographic images, segmentation is a crucial step because it has an impact on following computations. However, there exists a

fuzzy transition between the two materials (air and ice) due to noise and partial volume effect, so that there remains some uncertainty on the determination on the exact interface positions.

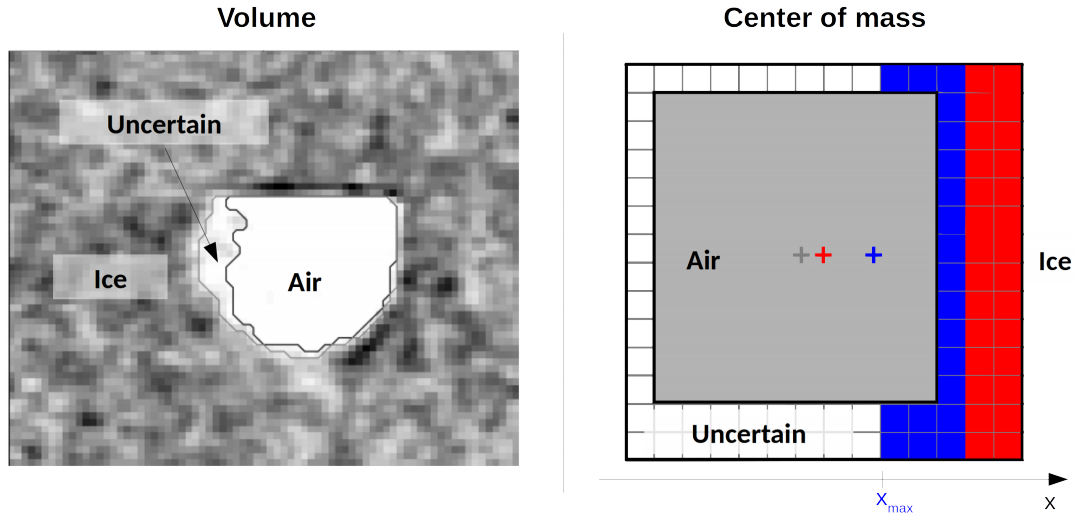


Figure 3.6: Evaluation of uncertainties due to segmentation using two acceptable segmentations. Left: uncertainty on volume is the difference of volume between the two segmentations. Right: scheme of principle for estimating maximum coordinate value of center of mass of the cavity in the x direction. Black solid lines represent the two possible segmentation as squares for simplicity, grey squares represent uncertain voxels. Possible voxels are added successively from high values of x (red voxels then blue voxels) and center of mass computed (Grey cross correspond to inner segmentation, then updated successively in red cross then blue cross) up to the point where the maximum value x_{max} is reached.

In order to estimate the impact of such uncertainties on the volume and the center of mass position, we determined two acceptable segmentations delimiting the extreme reasonable position of the interface: one for which no ice is possible in voxels segmented as air, and an other one in which no air is possible in voxels segmented as ice (see Figure 3.6). That way, the voxels which have different values between the two segmentations correspond to uncertain voxels at the interface. These voxels are used to compute uncertainty on volume and center of mass. The uncertainty on volume corresponds to the difference of volume computed from the two segmentations. The uncertainty on center of mass is estimated as follows: First, the center of mass corresponding to the inner segmentation is computed (in grey). Second, to compute as for example the maximum coordinate along x axis, uncertain voxels are successively added to the inner segmentation and center of mass computed, starting from a high x value. The computation stops when the maximum x coordinates is reached. The computations for the center of mass uncertainty on all directions are computed similarly.

The results are presented in Figure 3.7. From top to bottom, in the first panel, the displacement of the three coordinates of the center of mass over time is presented:

black being the vertical coordinate, blue and red being the two horizontal coordinates. Segmentation uncertainty is presented by error bars. The solid black curve is a linear fit to vertical displacement over time. We can observe that i) the displacement is almost vertical and ii) the evolution is linear, i.e. the migration speed of the cavity is constant and equals $4.5 \cdot 10^{-10} \text{ m s}^{-1}$. The second panel corresponds to the volume of the cavity, with error bars depicting the uncertainty due to segmentation. We observe that these uncertainties are small relative to the volume, which remains constant at 0.0119 mm^3 . The third panel represents the inertia momenta (red, blue and black points) and also the ratio between the momenta in black and blue (green crosses). For each momentum, i.e. for each color, the angle between the associated principal direction of inertia and the vertical is presented in the fourth panel. A schematic representation of these three principal directions with corresponding colors is given on the right of the figure. One of the angles initially close to zero becomes equal to zero (black), while the two other angles are 90° . This means that one of the principal axis of the cavity is aligned with the vertical direction while the two others are in the horizontal plane. In addition, we see that the inertia momenta associated with the vertical axe (black) increase while those associated with horizontal directions (blue and red) slightly decrease: The ratio of inertia momenta between horizontal and vertical directions decreases from 1 to 0.75. This means that the cavity flattens as it migrates.

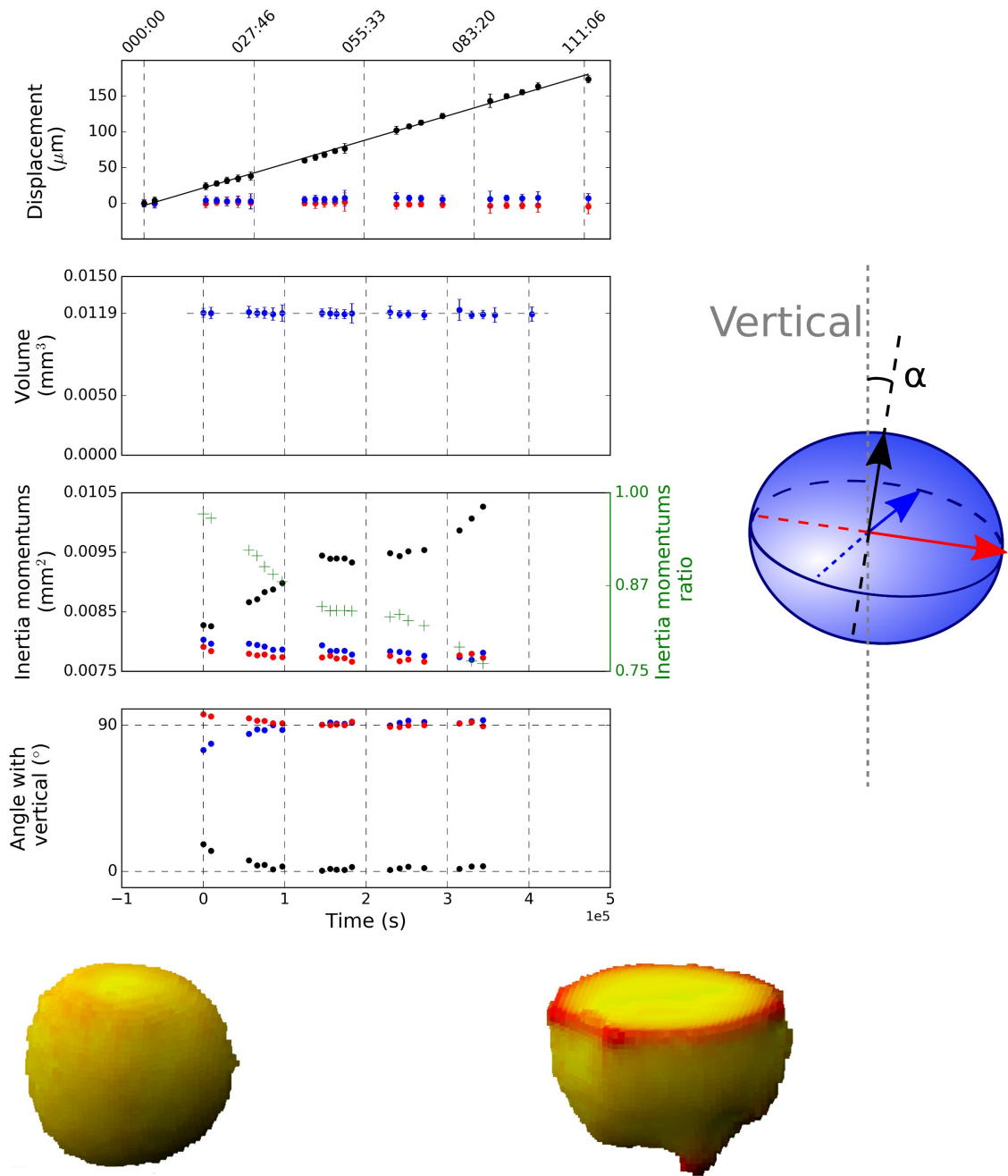


Figure 3.7: Top: Displacement of the coordinates of the center of mass of the cavity. Black signs corresponds to vertical direction; the solid line depicts the associated linear fit. Bars are uncertainties corresponding to segmentation of the images. The solid line is linear fit. 2nd panel: evolution of the volume. 3rd panel: principal inertia momenta (blue, red and black points) and inertia momenta ratio (green cross) between blue and black momenta. 4th panel: angle of the associated principal direction with the vertical direction, colors are represented by schematics on the right. Images at the bottom are views of the cavity at initial and final states.

3.4 Simulations

3.4.1 Isotropic model

In order to underline the effects of the anisotropy of the kinetic coefficient, we first performed a simulation with an isotropic kinetic coefficient. These first simulation results presented here are for initially ellipsoidal cavities migrating under a temperature gradient. Simulation was done using the Finite Element Method with the

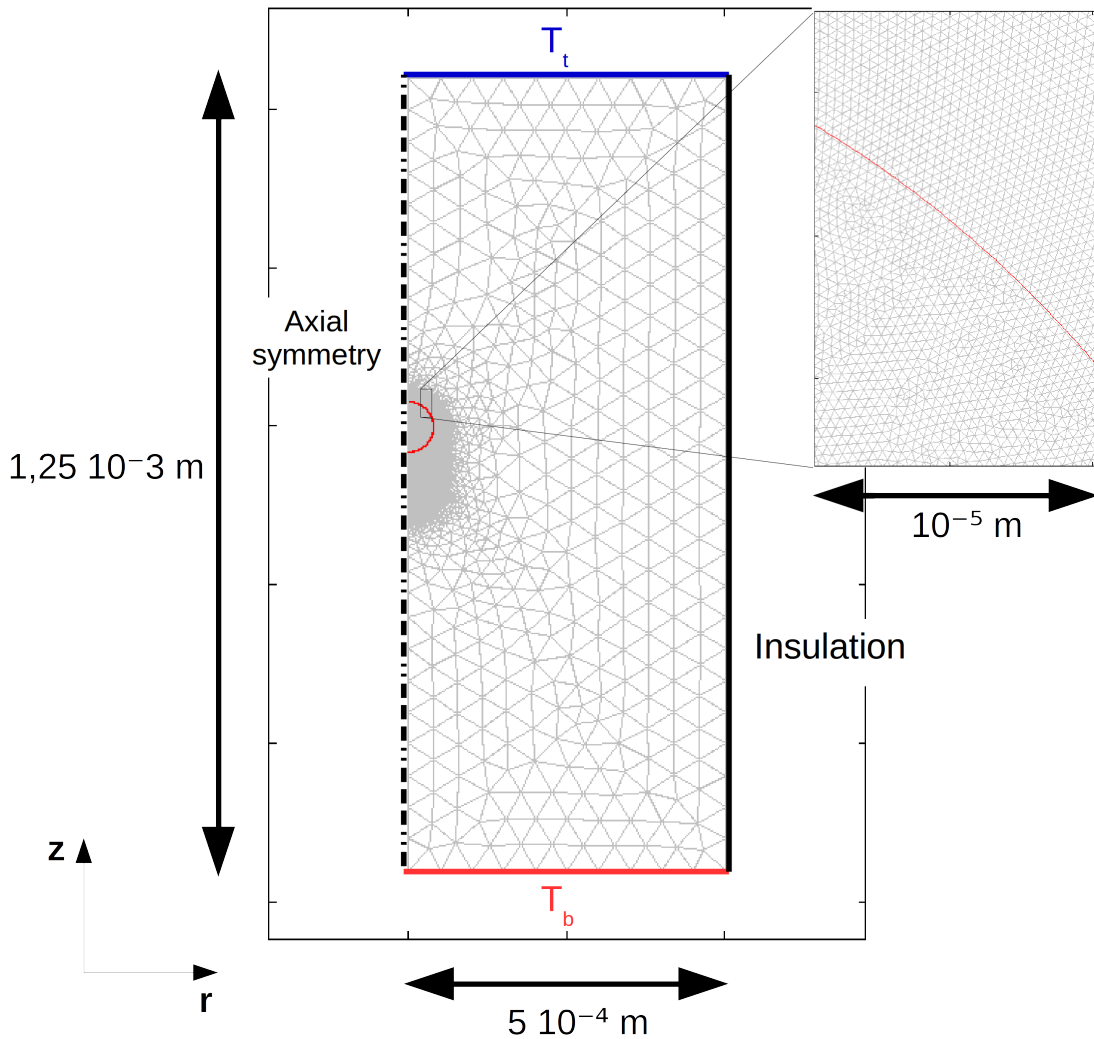


Figure 3.8: Representation of the domain, mesh and boundary conditions used for simulation in the isotropic case

commercial Software COMSOL Multiphysics. The simulations were made under the hypothesis of symmetry of revolution of the problem. The domain of resolution is then bidimensional (Figure 3.8) and consists of a rectangle of width $5 \cdot 10^{-4}$ m and height $1.25 \cdot 10^{-3}$ m. The boundary conditions are as follows: the left side is the axial symmetry condition, radial partial derivatives for the variables are 0 on this boundary. For ϕ and u , Neumann conditions of zero flux is imposed on all boundaries. For temperature, Dirichlet conditions of $T = T_t$ and $T = T_b$ are imposed

on top and bottom boundaries respectively. Zero flux, i.e. insulation, is imposed on the right boundary. This permits the imposition of a macroscopic temperature gradient.

A phase-field model implies really steep gradients of the variables at the interface, typically on a thickness W . Here, we used a single mesh with element size extremely fine in the area swept by the interface during its evolution. For simulations with $W = 5 \times 10^{-7}$ m, elements of size 4×10^{-7} m were used. Over the rest of the domain, elements of size 5×10^{-5} m were used.

For all simulations, initial conditions were defined as follows: first, phase-field was set to a desired geometry of the interface: ϕ was set to 1 (ice) outside a given circle and -1 (air) inside. Then, the problem was solved for 100 s with equation (3.16) alone so that ϕ relaxed to a smooth profile. Then, the equilibrium for temperature (equation 3.17) alone was computed, and finally u was initialised at $u_{eq}(T)$. The simulation was then performed by solving the fully coupled problem equations (3.16) - (3.18).

Three initial states were studied (see Figure 3.9, left column): a circular cavity of radius 39 μm , and ellipsoidal cavities, oriented either vertically or horizontally, with semi-major axis 50 μm and semi-minor axis 25 μm . The temperature gradient was set to 49 $^{\circ}\text{C m}^{-1}$ with mean temperature $\frac{T_t+T_b}{2}$ of -4°C . Simulations were performed with $\beta = 2 \cdot 10^{-6}$ m s^{-1} and $W = 5 \cdot 10^{-5}$ m. The results are shown in Figure 3.9, each line corresponding to one of the three cases (circular, oblate ellipsoid, prolate ellipsoid) and columns corresponding to times $t_A = 0$ s, $t_B = 5 \times 10^5$ s and $t_C = 1.12 \times 10^6$ s. The red line represents the interface at $t = 0$ and the black line at the corresponding times. Coloured isolines correspond to isotherm contours. Grey levels represent water vapor density in the air. Whatever the initial shape of the cavity, we can see that it migrates towards the warm side and ends up as a sphere.

We then computed the following global quantities: the center of mass of the cavity, its volume and the inertia momenta of the section. The results are given in Figure 3.10. For inertia momenta, the ratio of the momentum with respect to radial direction to the momentum with respect to vertical direction is represented. Over the three panels, the spherical cavity is represented in green, prolate ellipsoid in red, and oblate ellipsoid in blue. We can observe that:

- The displacements evolve linearly, so the migration speed is constant and is equal to $1.4 \cdot 10^{-10}$ m s^{-1} .
- For the three cavities, the volume remains constant over time.
- For the three cavities, the inertia momentum ratios evolve to one, i.e. the ellipsoidal cavities tend to spheres at the end of the simulations.

We suppose that this behavior is the superposition of two processes: the curvature effect, an initially spheroidal cavity under isothermal conditions would get rounded,

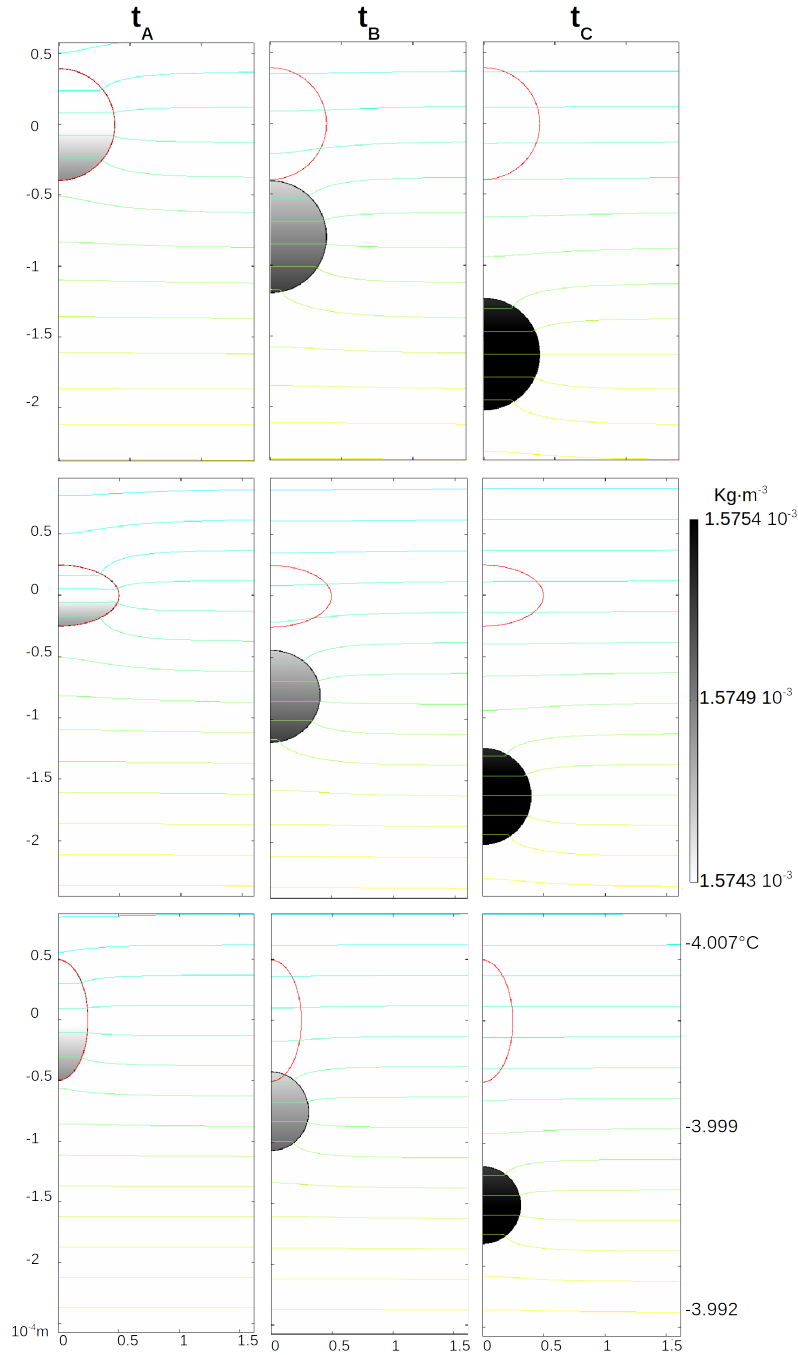


Figure 3.9: Simulation results for the evolution of ellipsoidal cavities in ice under a temperature gradient of $49\text{ }^{\circ}\text{C m}^{-1}$ with temperature at -4°C . Results for initial circular cavity (first line), oblate spheroid (second line), prolate spheroid (third line). At times, $t_A = 0\text{ s}$, $t_B = 5 \times 10^5\text{ s}$ and $t_C = 1.12 \times 10^6\text{ s}$ corresponding to points A, B, C on Figure 3.10, red and black contours correspond to position of the interface at initial and considered time respectively. Coloured contours correspond to temperature isolines, grey levels to water vapor density.

and the migration of the overall cavity due to the temperature gradient. In addition, the speed of migration is almost the same for the cavities with almost the same

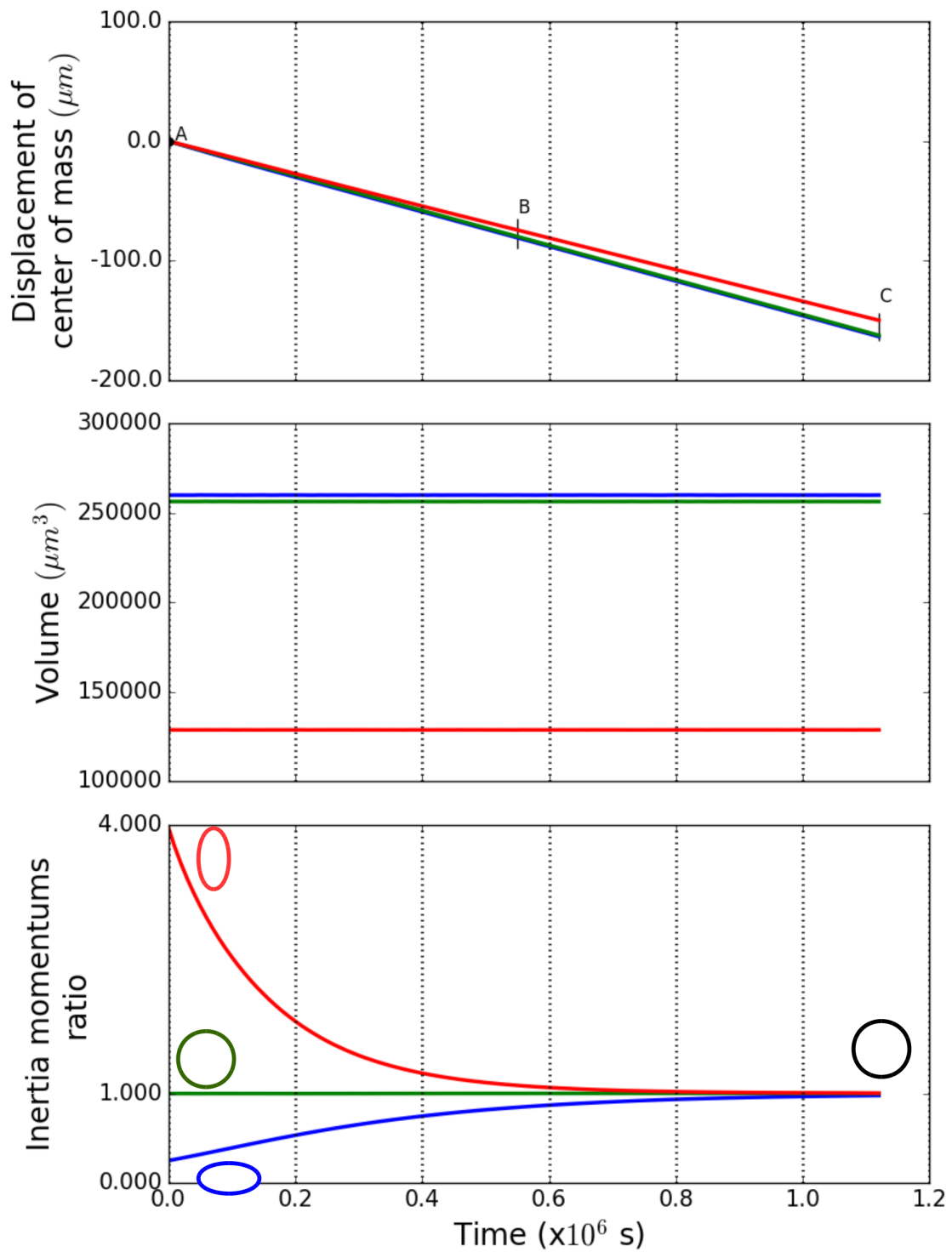


Figure 3.10: Evolutions of the position of the center of mass of a cavity (top), quadratic momentum ratio I_r/I_z (middle) and area of the 2D cavities (bottom) for the circular cavity (green) and the ellipsoidal cavity with the major axis aligned with vertical (red) or horizontal (blue) direction.

volume, while it's higher for the cavity with the smallest volume. *Shreve* [1967] shows that under the hypothesis of diffusion limited evolution, i.e. under the hypothesis

that kinetics are infinitely fast so that $\rho_v = \rho_{vs}$ at the interface, the velocity depends only of the shape and not on the size of the ellipsoidal cavity. So, the results obtained here differ from these conclusions. Actually, the present model does not make any assumption on a rate limiting process between diffusion and phase change at the interface. So, the observed differences suggest that the evolution in those simulations are not diffusion limited and that kinetics are not infinitely fast.

3.4.2 Anisotropic model

For comparison with the experiment, we simulated the migration of the cavity using an anisotropic kinetic coefficient.

The simulation was performed under the hypothesis of symmetry of revolution. This may be a good approximation as the prismatic faces on the cavity in the experiment are weakly marked. This implies that the kinetic coefficient is isotropic in the plane orthogonal to the c -axis of the crystal, the only remaining anisotropy of the crystal is in plane parallel to c -axis. At the initial state, the cavity is spherical with

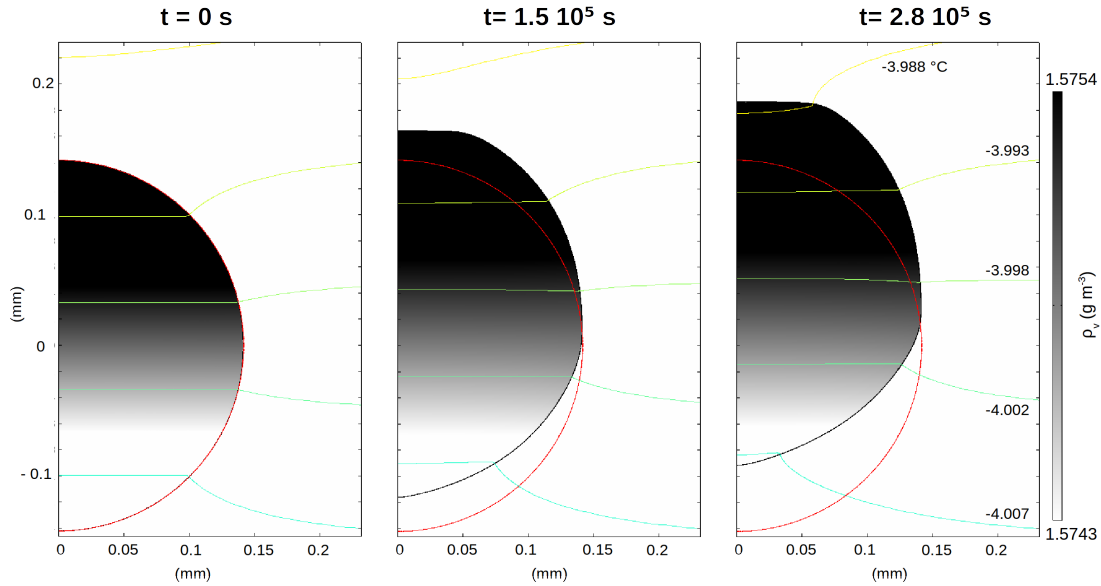


Figure 3.11: Simulating the migration of a cavity in a monocrystalline ice block under a temperature gradient, accounting for anisotropic kinetic coefficient with equation (3.24) and using $\beta_m = 2.5 \times 10^{-6} \text{ m s}^{-1}$, $\delta = 0.1$ and $k = 1$. Interface thickness is set to $W = 5 \times 10^{-7} \text{ m}$. Red and black contours correspond to position of the interface at initial and considered time respectively. Coloured contours correspond to temperature isolines, grey levels to water vapor density.

a radius of $141 \text{ }\mu\text{m}$ so that its volume corresponds to the volume of the experimental cavity. The simulation domain and mesh are similar to the ones presented in Figure 3.8 but increased in consequence to sizes of 2 mm in height and 5 mm in radius. Thermal boundary conditions were set so that a temperature gradient of $49 \text{ }^\circ\text{C m}^{-1}$ was imposed with a mean temperature of $-4 \text{ }^\circ\text{C}$ over the domain. The initialisation

was performed with the same procedure as for simulation of section 3.4.1. We chose to only simulate the beginning of the experiment: the finely meshed area covers 50 μm of displacement of the cavity. This enables us to limit the degree of freedom of the simulation while allowing comparisons. For that simulation, the kinetic coefficient was defined from equation (3.24), with parameters $\beta_m = 2.5 \times 10^{-6} \text{ m s}^{-1}$, $\delta = 0.1$ and $k = 1$. In consequence, the critical interface thickness is $1 \times 10^{-6} \text{ m}$. The simulation was performed with $W = 5 \times 10^{-7} \text{ m}$. With that set of parameters, the critical speed of the model is $5 \cdot 10^{-10} \text{ m s}^{-1}$.

The results obtained are given in Figure 3.11. As before, the red and black isolines correspond to interface at $t=0$ and considered time respectively, grey values to water vapor density and coloured isolines to temperature isolines. The cavity migrates toward the warmer temperatures. On the sublimating part, a facet develops progressively with a $\theta = \pi/2$. The part subject to deposition stays rounded.

Quantitative values are plotted in Figure 3.12. The displacement of the center of mass (upper panel) evolves linearly with a speed of 1.9 m s^{-1} , so the condition (3.22) is verified. The volume (middle panel) is conserved (with variations $< 0.02\%$). The bottom panel presents the inertia momentum ratio I_r/I_z of a vertical section, where I_r is the momentum ratio with reference to radial direction, and I_z with reference to vertical direction. This ratio decreases slightly from 1 to 0.97.

The overall simulated evolution of the cavity corresponds well to the experiment in several ways: i) a basal facet appears on the sublimating side while the depositing side remains rounded, ii) the speeds are constant and are equal up to a factor 2.4, iii) the volume is preserved and iv) the cavity flattens.

More quantitatively, the simulated speed is half of the experimental one and the facet and the flattening is not as large as in the experiment. As documented by *Uehara and Sekerka* [2003], a stronger anisotropy (higher δ) would lead to a stronger faceting. In addition, faceting occurs when assuming an anisotropic kinetic coefficient, so kinetics could not be assumed infinitely fast and actually influences the interface velocity. So, the advance speed of the interfaces depends on β : a greater β_m should imply a faster migration. So, the beta function could in principle be adjusted to fit the experiment. The values used here were limited by the validity of the phase-field approach since conditions (3.21) and (3.22) depend inversely on β . Because many uncertainties remain on kinetic coefficient measurements, we used here physically reasonable parameters that comply well with validity conditions. Discussion on available data on β and computational cost is developed in the next section.

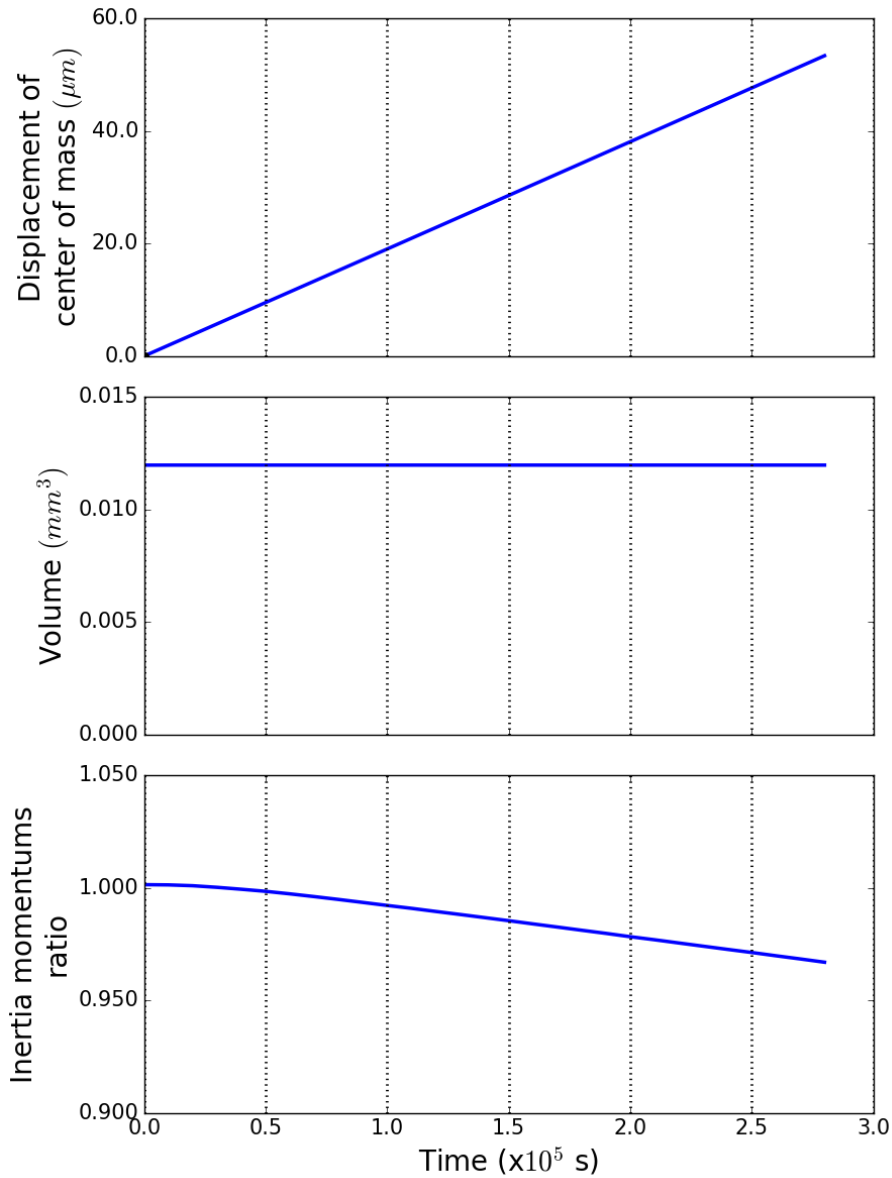


Figure 3.12: Evolution of the displacement of the center of mass of the simulated cavity, its volume and the ratio I_r/I_z of the inertia momentums of a vertical section.

3.5 Discussion

3.5.1 Kinetic coefficient values

The kinetic coefficient is a parameter at the grain scale that represents globally the different attachment mechanisms of molecules on the surface. These processes are of a lot of variety. The anisotropic function used here is a very simple representation. It takes into account that the orientation corresponding to a crystalline face will present the lowest density of steps, while other orientations will be much rougher. If no other kinetic process is considered, the kinetic coefficient would be equal to zero in the crystallographic orientations because those orientations would be molecularly

smooth [*Burton et al.*, 1951; *Chernov*, 1974; *Yokoyama and Kuroda*, 1990] i.e. that those orientations would not be able to grow. In the presence of step generators, like screw dislocation or 2D nucleation, step density is not zero at singular orientations and does not depend greatly on the orientation. In consequence, the minimum in kinetic coefficient function would then not be sharp and equal to zero, but be a plateau at a finite value that, however, should depend on supersaturation and/or temperature.

Here, the function used just has a finite minimum and reproduces the sharp variation in the vicinity of crystallographic faces. This is to implement the fact that crystallographic faces can actually grow.

It's well known that snowflakes change depending on the temperature and supersaturation as Nakaya's diagram shows [*Nakaya*, 1954; *Kobayashi*, 1961]. Particularly, shape changes sequentially from plates to prisms at -4 °C, from prisms to plates again at -10 °C and finally from plates to prisms at -22 °C. The current picture on this shape change is given by the Kuroda and Lacman model [*Kuroda and Lacmann*, 1982], which explains that plates are the result of a kinetic coefficient bigger for the prismatic faces than on basal faces, and inversely for the prism type. At the transitions, kinetic coefficients should be sensibly similar. This enable us to assume reasonably equals minima in the anisotropy function used for the simulations.

In terms of value for the crystallographic faces, experimental data are sparse and controversial, because the condensation coefficient is a difficult quantity to measure [*Libbrecht*, 2004]. *Libbrecht and Rickerby* [2013] show measurements for temperature ranging from -40 °C to -2 °C at low background pressure, typically < 0.025 atm. However, *Libbrecht* [2016] shows that the condensation coefficient for prismatic faces may vary strongly with background pressure. In the experiment presented here, we do not know the actual pressure inside the cavity, which prevents us from detailed estimation.

Because many uncertainties remain on the kinetic coefficient, values used here were selected at order of magnitude of about 2×10^{-6} m s $^{-1}$, following *Kaempfer and Plapp* [2009].

3.5.2 Computational cost

Computational cost is the bottleneck in phase-field modeling. Here, due to computational restrictions in the simulation presented in section 3.4.2, the interface thickness was set to $W = 5 \times 10^{-7}$ m to comply with characteristic thickness necessary for phase-field convergence of 10^{-6} m. Similarly, the speed of the cavity was of 2×10^{-10} m s $^{-1}$, for a limit speed of relaxation of the model of 5×10^{-10} m s $^{-1}$. In other words, the constraints (3.21) and (3.22) are verified, but without large margins. Thus, even if the results compare quantitatively well with the experiment, particularly when taking into account the uncertainty on the kinetic coefficient,

the reliability on the model predictions could still be increased by decreasing the interface thickness. However, this implies a higher computational cost.

If one would like to obtain more detailed quantitative results or perform computation on complex structures, the model cost should be reduced. This basically can be done in two ways: developing a thin interface-limit and/or using an adaptive mesh-refinement. The first consists in writing the asymptotic analysis at one supplementary order, choosing the interface thickness so that only errors at second order are a priori negligible. The errors made at first order are then suppressed by choosing a particular interpolation function for material properties in the diffuse interface layer and by adding an extra term, the so-called anti-trapping current [Karma and Rappel, 1998]. This permits us to perform simulations with greater W , and so, with a coarser mesh. Secondly, a strong gradient of variables occurs in the diffuse interface only. A refined mesh is only needed in its vicinity. So, the phase-field method is a typical example where adaptive mesh refinement techniques would permit to optimize greatly computations. Greenwood *et al.* [2018] obtained 1-2 order of magnitudes speedup for a simulation in alloy solidification using this approach.

3.6 Conclusion

Anisotropy in the kinetic coefficient has been used in a phase-field model to better describe snow metamorphism, and in particular, the associated faceting effect. Simulation of the migration of an air cavity in a monocrystalline ice block under a temperature gradient has been performed and compared to an experiment. The model compares well with experiment as in both cases:

- A facet appear on the sublimating while the cavity stays rounded on the deposition side
- Faceting is associated with flattening of the cavity in the direction of the temperature gradient
- The volume is conserved.
- Speeds of migration are constant in both cases and are similar within a factor of 2.4

Additionally, comparison with simulations taking into account isotropy confirms that i) faceting is due to kinetic coefficient, and ii) evolution is not diffusion limited. That said, the values of the kinetic coefficient and strength of anisotropy were constrained by computational cost. More accurate parameters could be used if one decreases the computational cost, e.g. by the developement of thin-interface limit and/or mesh refinement technique. Additionally, one could take into account more finely physical function for the kinetic coefficient by taking into account the difference of kinetics between basal and prismatic faces, and the dependence upon

temperature and supersaturation implied by growth mechanisms like 2D Nucleation or dislocation-aided growth. Such refinements will need additional experiments and cross-comparisons and will be considered in future works.

Adjusting phase-field simulations to an experiment of negative crystal growth at -10°C

Abstract

We present an attempt at adjusting phase-field simulations to an experiment of negative crystal growth in an ice monocrystalline ice block at -10°C . This constitutes a study case for faceting in ice and water vapor systems. Experimentally, the cavity takes the shape of a hexagonal prism with an aspect ratio of two. In the simulation, faceting was introduced using a highly anisotropic kinetic coefficient with narrow singular minimums. A ratio of 6 between kinetic coefficients at a singular orientation was used. A qualitative agreement is found as the cavity takes a well faceted shape and differences in the advancing rates of facets are observable. However, strong assumptions required to make the simulation computationally tractable prevent quantitative comparison with experiment.

4.1 Introduction

Snow grains exist in various shapes in the snowpack. This media results from the accumulation of snowflakes on the ground and consists of a porous media made of ice, air containing water vapor, and sometimes liquid water. The variety of shapes results in a corresponding variety of mechanisms of transformation from the initial snowflakes. These mechanisms are called snow metamorphism, see *Arons and Colbeck* [1995] and *Fierz et al.* [2009] for a review. Considering dry snow only, if the temperature gradient is small, typically under 10 K m^{-1} rounded grains are formed. This shape is explained by the Kelvin effect [*Colbeck*, 1982; *Flin et al.*, 2003]: The water vapor density at saturation increases with increasing curvature of the ice/air interface. Convexities in the microstructure tend to sublime, releasing water vapor that diffuses in the pore space and deposits in concavities where water vapor saturation is lower.

When the temperature gradient increases, as the water vapor density at saturation increases with temperature, a gradient of water vapor density at saturation develops over the snow. Under these conditions, the local disequilibrium of the ice with the water vapor phase can be important and this leads to faceted crystals, which are solid crystals with smooth flat surfaces, or even depth hoar crystals, which are faceted hollow crystals, often cup-shaped with striations. The presence of facets in the microstructure is a characteristic of temperature gradient metamorphism. As this is associated with higher local disequilibrium, it is commonly accepted that it is due to the effects of attachment kinetics, the processes by which new molecules are integrated into the crystalline lattice, that become predominant for high temperature gradients. For this reason, depth hoar crystals and faceted crystals are also called kinetic forms, while rounded grains are called equilibrium forms [*Fierz et al.*, 2009].

These morphologies can be compared with snowflakes morphologies. At the difference of snowpack microstructure, snowflakes are single crystals of ice growing independently in a wet atmosphere where the excess humidity first nucleates on aerosols and then deposits on the newly formed ice crystals. As shown by Nakaya's diagram [*Nakaya*, 1954; *Kobayashi*, 1961; *Furukawa*, 2015; *Libbrecht*, 2017], snowflakes come in various shapes and because of the hexagonal structure of ice, the formed crystals have a 6-fold symmetry. The crystals can be classified from two characteristics: the relative ratio of their extents in the three directions of space and their dendritic aspect. Indeed, depending on temperature, the crystals may be:

- plate-like, i.e. with an extent normal to the basal plane being significantly smaller than in the prismatic directions,
- column-like, i.e. with an extent in the direction normal to the basal plane being larger than those in the basal plane.

With increasing supersaturation, the formed crystals are in first solid like, i.e. with flat facets, then hollow and finally dendritic.

While the morphology of both snowflakes and snow on the ground are well described empirically, an accurate theoretical understanding is still lacking [*Libbrecht*, 2017]. Snowflake formation received more theoretical considerations than snow metamorphism. The model presented by *Kuroda and Lacmann* [1982] explains the dependence on temperature by a difference in kinetics between basal and prismatic faces. The presence of facets can be simulated from anisotropy of both kinetics [*Yokoyama and Kuroda*, 1990] or surface tension [*Barrett et al.*, 2012; *Demange et al.*, 2017]. The dendritic formation is due to a Mullins-Sekerka instability [*Mullins and Sekerka*, 1964] which is a purely diffusional effect acting on the corners of faceted crystals.

In the context of snow metamorphism, it is, however, rather expected that facets are due to kinetic effects. Indeed, the surface tension dependence on orientation predicts the equilibrium shape of the crystals which is quite rounded. Thus, surface

tension is expected to be rather isotropic. However, while this interpretation is consistent with experiments on snow metamorphism, no model currently exists for simulating kinetic forms formation during temperature gradient metamorphism. *Kaempfer and Plapp* [2009] developed a phase-field model for snow metamorphism coupling heat and mass diffusion with phase change. This however does not account for faceting and is, thus, restricted to curvature driven metamorphism.

If one wants to improve understanding of snow metamorphism, it should take into account kinetic effects in a physically realistic manner. This could then permit us to investigate the theoretical consequences of these effects. For example, the transitions between weak gradient metamorphism, leading to rounded forms, and temperature gradient metamorphism is coarsely known, and refinement in its understanding is highly desirable as rounded and faceted forms have extremely different properties, particularly mechanical behavior. Recent studies [*Adams and Miller*, 2003; *Riche et al.*, 2013; *Calonne et al.*, 2017] suggest that kinetic differences between basal and prismatic faces leads to selective growth of grains under temperature gradient metamorphism, which makes the distribution of the crystalline orientation to become anisotropic. Particular microstructures like chains of depth hoar that may appear in low density snow under high temperature gradient [*Staron et al.*, 2014] or hard depth hoar, which are depth hoar well bounded by necks [*Akitaya*, 1974; *Pfeffer and Mrugala*, 2002], forming in high density snow under high temperature gradient could be addressed. In order to reach this accuracy, it would be necessary that the model could quantitatively reproduce the experiments.

Here, we present an attempt of adjusting phase-field simulations on a dedicated experiment of negative crystal growth. In such an experiment, the geometry is well controlled and the crystal dimensions as well as its aspect ratio can be accurately measured. The first section describes the model. The experiment of negative crystal growth is presented in section 2. The third section describes the associated simulations.

4.2 Model summary

The phase-field modelling is based on the model of *Kaempfer and Plapp* [2009] (see also chapter 3). The model equations can be written:

$$\frac{W^2}{\beta(\mathbf{n})d_0} \frac{\partial \phi}{\partial t} = W^2 \Delta \phi + (\phi - \phi^3) + \frac{5\sqrt{2}W}{8} \frac{\rho_i}{d_0 \rho_{vs}(T)} [u - u_{eq}(T)] (1 - \phi^2)^2 \quad (4.1)$$

$$C(\phi) \frac{\partial T}{\partial t} = \nabla[\kappa(\phi) \nabla T] + \frac{L}{2} \frac{\partial \phi}{\partial t} \quad (4.2)$$

$$\frac{\partial u}{\partial t} = \nabla[D(\phi) \nabla u] - \frac{1}{2} \frac{\partial \phi}{\partial t} \quad (4.3)$$

where the variables are the phase-field ϕ , the temperature T , and the dimensionless density u . W is the smooth interface width, β is the kinetic coefficient (m s^{-1}) that can depend on the orientation of the normal \mathbf{n} to the interface, d_0 is the capillary length, ρ_i the ice density and $\rho_{vs}(T)$ is the water vapor density at saturation. $u_{eq}(T)$ is the dimensionless water vapor density at saturation.

One can define a water vapor density $\rho(\phi)$ and water vapor density at saturation $\rho_{eq}(\phi)$ extended in the ice phase with:

$$\rho(\phi) = \rho_i \frac{1 + \phi}{2} + \rho_v \frac{1 - \phi}{2} \quad (4.4)$$

$$\rho_{eq}(\phi, T) = \rho_i \frac{1 + \phi}{2} + \rho_{vs}(T) \frac{1 - \phi}{2} \quad (4.5)$$

u and $u_{eq}(T)$ are related to the water vapor density ρ_v and water vapor density at saturation $\rho_{vs}(T)$ by:

$$u = \frac{\rho(\phi) - \rho_{eq}(\phi, T^{ref})}{\rho_i} \quad (4.6)$$

$$u_{eq}(T) = \frac{\rho_{vs}(T) - \rho_{vs}(T^{ref})}{\rho_i} \quad (4.7)$$

The heat capacity $C(\phi)$, the heat conductivity $\kappa(\phi)$ and the water vapor diffusivity coefficient $D(\phi)$ are interpolation of the physical values in air and ice respectively, with:

$$D(\phi) = D_v \frac{1 + \phi}{2} \quad (4.8)$$

$$\kappa(\phi) = \kappa_a \frac{1 + \phi}{2} + \kappa_i \frac{1 - \phi}{2} \quad (4.9)$$

$$C(\phi) = C_a \frac{1 + \phi}{2} + C_i \frac{1 - \phi}{2} \quad (4.10)$$

where D_v is the water vapor diffusivity coefficient, κ_a and κ_i the heat conductivities in air and ice, respectively, and C_a and C_i are the heat capacities in air and ice, respectively.

Equation (4.1) is the phase-field equation that describes the evolution of the interface. The term $(\phi - \phi^2)$ is a double-well potential term that makes the values in the bulk to be -1 for air and 1 for ice. The last term with $u - u_{eq}(T)$ is the coupling terms that represents the Hertz-Knudsen relation. Equation (4.2) is the heat equation in which the last right hand side term accounts for the latent heat release or absorption due to a phase change. Similarly, equation (4.3) is the water vapor diffusion and the last term ensures mass conservation at the ice/air interface. This set of equations with the corresponding definitions of interpolated material properties is the sharp interface limit phase-field reformulation of the associated Stefan problem. The convergence of the reformulation is ensured as long as the interface width W is

small enough to remain in the sharp interface limit. As demonstrated by *Kaempfer and Plapp* [2009], this leads to a set of constraints that can be formulated as:

$$W \ll \min \left(1/K, \frac{1}{\beta' C_i}, \frac{1}{\beta' C_a}, \frac{1}{\beta' D_v}, \frac{d_0 \beta'}{v_n} \right) \quad (4.11)$$

where $\beta' = \beta \frac{\rho_i}{\rho_{vs}}$ and v_n is the interface normal velocity. The first of these constraints is that the width of the interface should remain small in comparison with the smallest radius of curvature in the microstructure. The three following constraints ($\frac{1}{\beta' C_i}$, $\frac{1}{\beta' C_a}$ and $\frac{1}{\beta' D_v}$) arise from the match-asymptotic analysis and are the necessary constraints for the anomalies in the interface conditions to remain small [*Kaempfer and Plapp*, 2009; *Almgren*, 1999]. The last constraint is necessary to have the phase-field profile to be close to its equilibrium profile. Otherwise the match asymptotics analysis does not hold.

The difference in the present simulations with the model presented by *Kaempfer and Plapp* [2009] holds in the expression of the kinetic coefficient. In order to produce kinetic faceting, it is necessary to use an highly anisotropic kinetic coefficient.

As explained by *Chernov* [1974] and *Yokoyama and Kuroda* [1990], when looking at a vicinal face, i.e. a crystal face inclined from a crystallographic plane, at the molecular level, one sees that it is composed of molecular steps and terraces. The step density then depends on the inclination angle of this vicinal face from a singular face. It reaches its minimum for a singular face, and its maximum for intermediate orientations as the face is molecularly rough for significantly inclined faces.

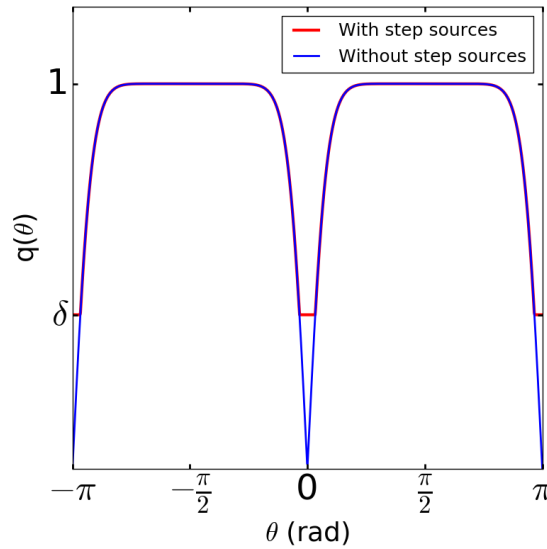


Figure 4.1: Anisotropy of the kinetic coefficient depending on the inclination θ from a singular orientation.

In consequence, the kinetic coefficient has narrow singular minima in the direction of singular faces. In addition, if no step generators are considered on singular faces, those are molecularly smooth. Thus, the kinetic coefficient drops to 0. A general form to describe the anisotropy is then given by:

$$q(\theta) = \tanh\left(\frac{k}{|\tan(\theta + \frac{\pi}{2})|}\right) \quad (4.12)$$

which is represented in blue in Figure 4.1. k is a parameter that describes the narrowness of the minimum. Because of mechanisms like 2D nucleation or dislocation growth, the step density is not zero on singular faces. And even for slightly inclined vicinal faces, the step density will be dominated by those processes. As a consequence, a more realistic anisotropy is given by the red curve on Figure 4.1, where the kinetic coefficient becomes independent of orientation near singular orientations. δ is the ratio between the kinetic coefficient of the singular face, i.e. at the minimum, and the maximum kinetic coefficient. The value of the minima could be made dependent of temperature and supersaturation to represent more finely the growth mechanisms cited above. However, here, we focus on characterizing faceting arising from high kinetic anisotropy, for this reason we will not consider this dependence in this work. According to these results, the differences in kinetic coefficient for the different faces, namely between prismatic and basal faces can be then modeled with unequal minimum values between basal and prismatic orientations.

In the following, we will assume symmetry of revolution around the c axis of the crystal. Although it is obviously not the case of an hexagonal prism, it permits us to greatly reduce the computational cost and allows us to have a small interface width, and thus, good convergence of the phase-field model. As we focus principally in reproducing the aspect ratio of crystals, errors due to this approximation should be of second order in comparison with the kinetic difference between basal and prismatic orientations. Thus, this globally permits us to obtain a more quantitative representation of the aspect ratio evolution.

We then used a kinetic coefficient depending only on the angle between the normal to the interface and the basal plane as depicted in Figure 4.2a. Let us define

$$\tilde{q}(\theta, \delta, \theta_0) = \max\left[\tanh\left(\frac{k}{|\tan(\theta + \frac{\pi}{2} - \theta_0)|}\right), \delta\right] \quad (4.13)$$

where θ_0 is the value of θ at the minimum and δ the value of the minimum of \tilde{q} . We then express the kinetic coefficient as:

$$\beta(\theta) = \beta_{max} \cdot \tilde{q}(\theta, r_\beta \delta, 0) \cdot \tilde{q}(\theta, \delta, \frac{\pi}{2}) \quad (4.14)$$

where r_β is the ratio of kinetic coefficient between the prismatic ($\theta = 0$) and the basal ($\theta = \pi/2$) orientations. A graphical representation of that function is given in Figure 4.2b for a case where $r_\beta > 1$

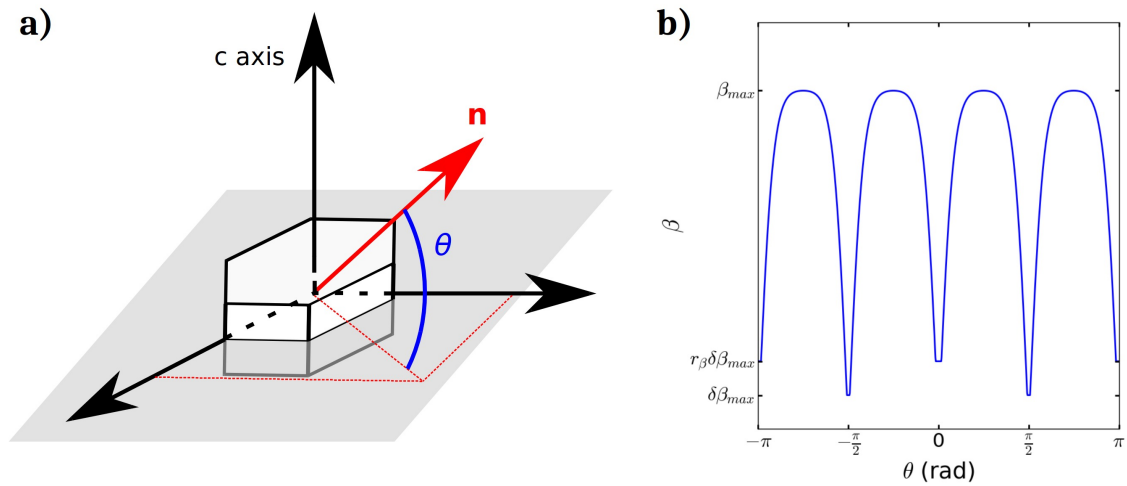


Figure 4.2: a) Orientation of \mathbf{n} and b) anisotropy of the kinetic coefficient used to represent kinetics differences between prismatic and basal faces.

4.3 Case of a simple ice/air system: negative crystal growth

4.3.1 Experiment

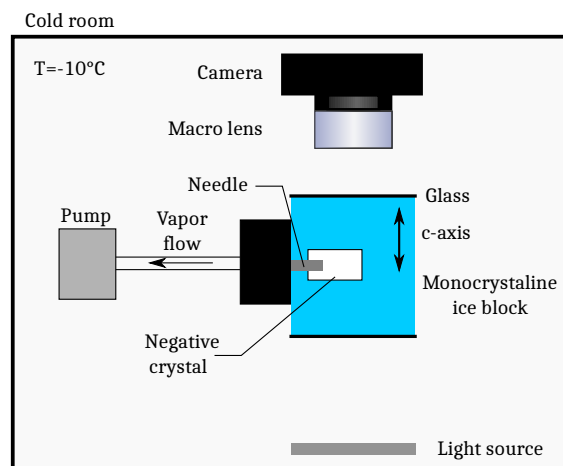


Figure 4.3: Scheme of the experiment.

In order to obtain well defined experimental data to guide accurate modeling, we conducted an experiment of negative crystal growth at the Institute of Low Temperature Science at Hokkaido, Japan. An ice negative crystal is a cavity in a monocrystalline ice block, where the growth is produced by pumping out water vapor from the cavity. The set up of the experiment is given by Figure 4.3. A needle of 0.8 mm of outer diameter is inserted into a monocrystalline ice block and connected to a vacuum pump. The water vapor at the tip of the needle is continuously pumped out so that the undersaturation level is maintained. Glass slides are stuck to the ice block in order to avoid optical distortion by the refracting exterior ice/air interface. The evolution of the cavity can then be followed by time-lapse microscopy through

the glass slides. All the apparatus is installed in a cold room whose temperature is maintained at $-10 \pm 2^\circ\text{C}$. Here, we are particularly interested in following the shape evolution and in measuring the growth rate of the different faces of the crystal. They are of two types: basal faces and prismatic faces. Thus, this requires to follow the evolution from two points of view. However, the setup did not permit to follow the evolution on the basal and prismatic faces simultaneously. So, the experiment was repeated twice: one time with an optical axis along the c-axis of the crystal (sample A) and a second time with the optical axis perpendicular to the c-axis (sample B). The experiment lasted for 1 day for Sample A and 2 days for sample B.

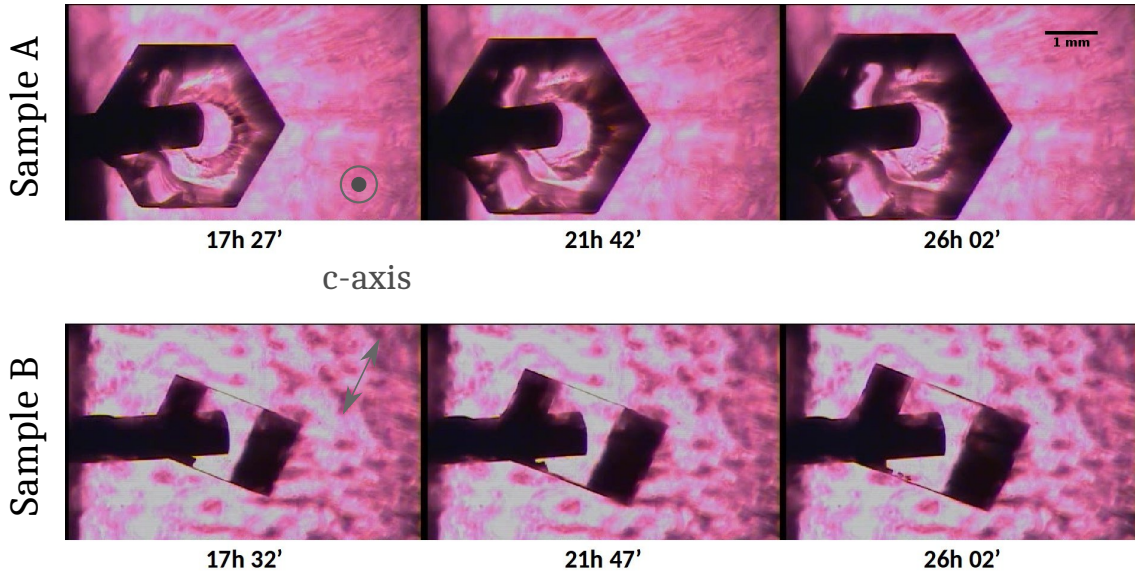


Figure 4.4: Negative crystals growing by pumping out water vapor from a monocrystalline ice block through a needle. Sample A: c-axis parallel to optical axis. Sample B: c-axis perpendicular to optical axis. For all photographs, the scale is given by the scale bar on the top right of the figure.

The images obtained are shown in Figure 4.4. In both cases, the ice/air interface is clearly defined, the cavity has the shape of a hexagonal prism and is nicely regular. Particularly, we observe that the presence of the needle has a minor effect on the interface, with the crystal being well centered on the tip of the needle and only the immediate neighboring interface area to the crossing point of the needle is affected.

From this time series, the interface is recovered from simple image analysis operations. The processing route goes as follow:

1. Sharpen images
2. Segmentation using isodata algorithm [*Ridler and Calvard, 1978*]
3. Three iterations of closing filter
4. Three iterations of opening filter

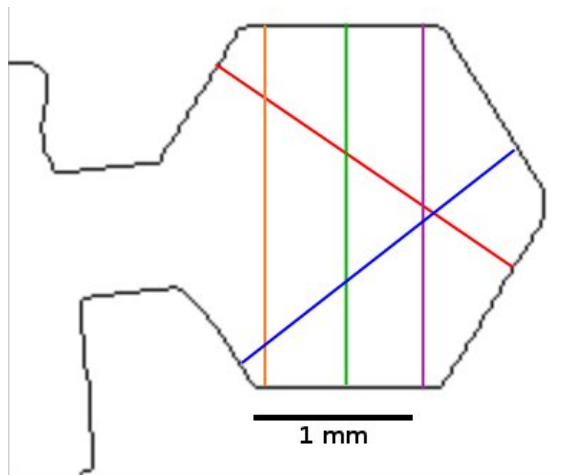


Figure 4.5: . Size measurements from the crystal contours obtained after image processing. Black: crystal contour for sample A obtained after processing at $t = 8$ h 15 min. Coloured lines show directions of size measurements on prismatic faces.

5. Sobel edge detection

An example of the results is given by the black contour in Figure 4.5. From this contour, the distances between the faces are computed from the contour pixels coordinates. The coloured lines in Figure 4.5 show lines along which the size of crystal is determined in the basal plane.

The results of the size evolution are presented by dots in Figure 4.6.a. Both extents increase with time. We note that measurements along yellow, green and purple directions overlap. These measurements were made on the same face (see Figure 4.5). Thus, there is no gradient of interface velocity along that face. In particular, the proximity of the needle tip does not lead to faster sublimation at the center of the face than at edges. We note also that the prismatic-prismatic size along the blue and red directions are similar but different to the first couple of prismatic faces. Additionally, the evolution appears to be non linear. We then defined a cubic root fit function f of the form:

$$f(t) = a + b\sqrt[3]{t} \quad (4.15)$$

where a (mm) and b ($\text{mm h}^{-\frac{1}{3}}$) are fitting parameters. The fits of that function to the size evolution with time are drawn as solid lines of the corresponding colors in Figure 4.6. This function fits well the data points and for all of the six curves, the root mean square error was less than 0.013 mm. The fact that the evolution with respect to time of the different sizes goes as $\sim \sqrt[3]{t}$ is consistent with a constant water vapor sink as this implies a volume increasing linearly with time.

We then compute the derivative of these functions in order to obtain a growth rate of the crystal. By definition, the interface velocity is half of the crystal growth rate. The results are drawn on Figure 4.6.b. The growth rates decrease with time

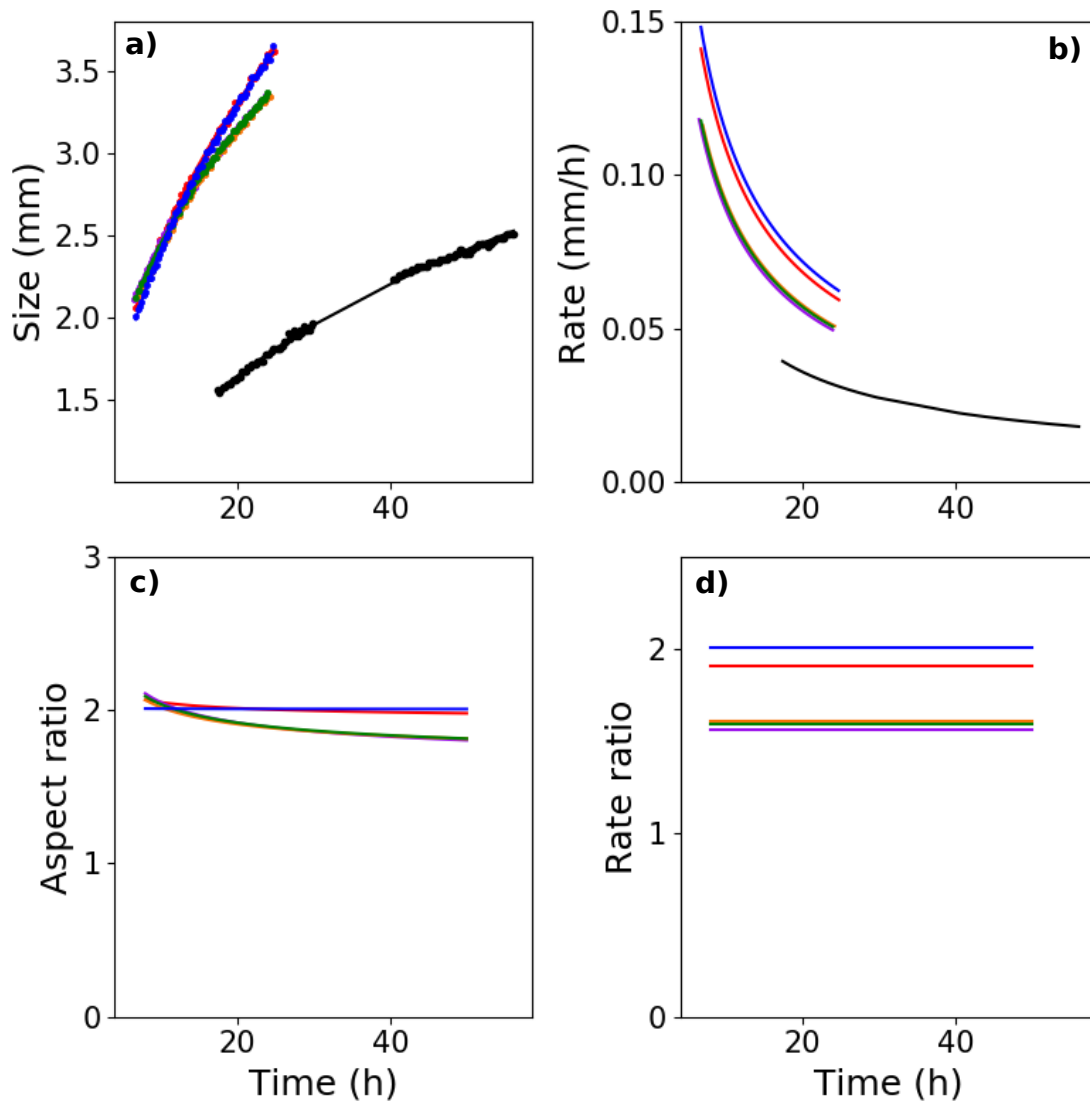


Figure 4.6: Quantitative data from image processing and analysis. a) Size evolution of the crystals, black dots refer to basal-basal distance, coloured dots refer to size measured in directions of the corresponding colour on Figure 4.5. Solid lines are cubic root fits of the form given by equation (4.15) to the data points with the corresponding color. b) Rates computed from the fits. c) Aspect ratio computed as the fitted prismatic-prismatic distance over fitted basal-basal distance. d) Rate ratios computed as the fitted prismatic growth rates over the fitted basal growth rates.

and are typically divided by two in the first 20 h. Additionally, we can note that the rates measured along blue and red directions are higher than those measured along yellow, green and purple directions. This last group of curves refers to the only couple of prismatic faces that are not crossed by the needle. So, a possibility is that the presence of the needle leads to a higher sublimation rate of the faces it crosses. This appears plausible as the edge between needle and ice may be a source of steps that sublimates more easily than on other faces.

From the fits, we also computed the aspect ratio, i.e. the ratio of prismatic-prismatic sizes over basal-basal sizes for the different measured prismatic-prismatic sizes. Figure 4.6.c represents these aspect ratios for all times where there is a data point for at least one of the two samples. In other words, this corresponds to an extrapolation of the basal-basal sizes for the early evolution ($t < 17$ h 25 min) and of prismatic-prismatic sizes for late evolution ($t > 25$ h 15 min). The aspect ratio appears to be close to two and to slightly decrease with time for that period of time. This result is consistent with Nakaya's diagram as -10 °C is a transition temperature between plate and column.

Finally, we computed from the fits the ratio of growth rate along prismatic directions over the growth rate along basal direction (Figure 4.6.d). Because of the form of the fit function given by equation (4.15), these ratios are constant over time and are about 2 for red and blue directions and about 1.6 for yellow, green and purple directions.

4.3.2 Simulation

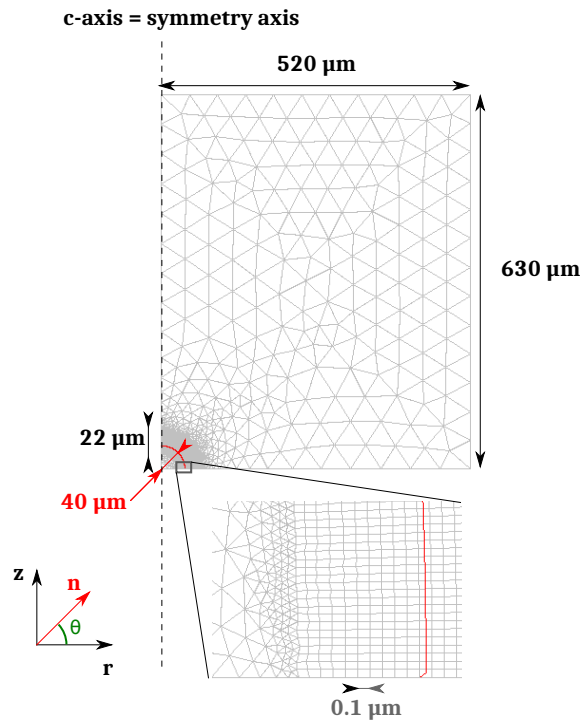


Figure 4.7: Domain, mesh (grey) and initial ice/air interface (Red)

In that simulation, we are interested in reproducing the size ratio evolution measured in the previous section, as this is representative of the crystal shape. Motivated by computational cost constraints $W \ll 1$ μm, we conducted simulations under several hypothesis:

- Assumption of axisymmetry: the 3D shape of the crystal is approximated by a cylinder whose axis is the c-axis of the crystals, i.e. the hexagonal shape

is replaced by a circular shape. Although this is clearly not the case in the experiment, this approximation permits us to use a 2D domain while preserving interactions between basal facets and the cylindrical facets (approximation of prismatic facets).

- A cavity of a reduced size (39 μm) in comparison to experiment (about 1 mm).
- The needle is modeled by a sink of water vapor inside the cavity

Figure 4.7 shows the computational domain and the initial conditions for the phase-field. The domain consists in a rectangle of 620 x 520 μm . The domain was meshed with two areas of different mesh size. Between two circles with the same center as the cavity with respective radii 38 μm and 62 μm , the mesh consists of regular quadrangles of size $W = 10^{-7}$ m. The rest of the domain was meshed with free triangles of maximum size of about 50 μm (see Figure 4.7). The mesh comprises in total 234,000 elements and leads to 700,000 degrees of freedom for the numerical resolution. The initial cavity was initialised as being spherical with a radius of 39 μm centered at the bottom left corner of the simulation domain, i.e. only one half of the cavity was simulated thanks to the periodicity of the anisotropy function. Thus, zero flux boundary conditions were imposed for all variables on bottom and left boundary of the domain. On top and right boundaries, zero flux was imposed for both the phase-field ϕ and the dimensionless water vapor density u , and a Dirichlet condition was imposed for T with $T = T_0 = 263.15$ K. At the initial state, u was set to u_{eq} and T to T_0 . The needle was represented by a sink of water vapor density of $Q = -10$ kg m $^{-3}$ s $^{-1}$ in a small sphere of radius 10 μm centered inside the initial cavity. In the simulation, the monocrystalline ice block was represented by defining

Parameter	Value
β_m	2×10^{-6} m s $^{-1}$
δ	1/60
r_β	6
w	1×10^{-7} m

Table 4.1: Parameters used for simulation of the pumping experiment.

the kinetic coefficient β uniquely all over the domain. β was defined by equation (4.14) so that c-axis was represented along the vertical direction ($\theta = \frac{\pi}{2}$), parallel to the symmetry axis. Parameters for the simulation are given in table 4.1, and the corresponding anisotropy function is represented in Figure 4.8. In particular, $r_\beta > 1$ implies that the cylindrical faces are more reactive than basal faces. The simulation is then performed up to a time of $t = 1.75$ h.

Figure 4.9 presents the 3D evolution of the cavity. We observe that the cavity is growing and takes progressively a cylindrical shape as it is faceting. The corner remains rounded but the radius of curvature decreases from the initial cavity radius

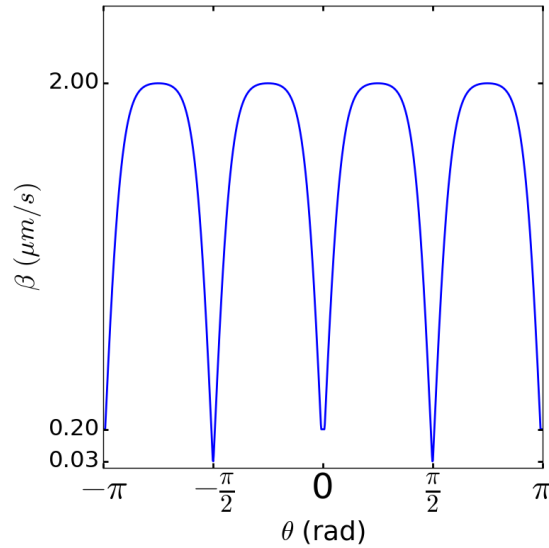


Figure 4.8: Kinetic coefficient used in the simulation.

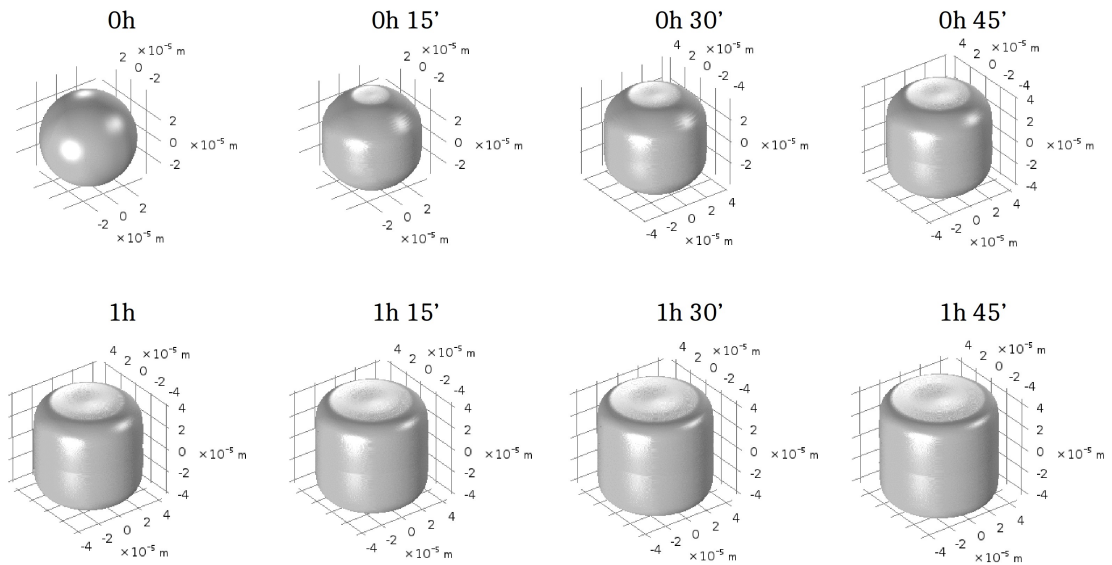


Figure 4.9: Simulation of negative crystal growth, assuming axial symmetry.

of about $40 \mu\text{m}$ to a value of approximately $10 \mu\text{m}$. The facets appear to be slightly convex at their centers.

Then, we measured the extents of the cavity along the c -axis (height) and perpendicularly to c -axis (diameter) as defined in Figure 4.10: the measure was done at the center of faces. Figure 4.11.a) shows the time evolution of diameter and height. At all times, the diameter of the cylinder is always greater than its height. That actually means that the face with the lowest kinetic coefficient is indeed the slowest. The evolution appears to be non linear.

This is well visible from the growth rates (Figure 4.11.b)), where such rates were computed as the time derivatives of diameter and height using a simple forward

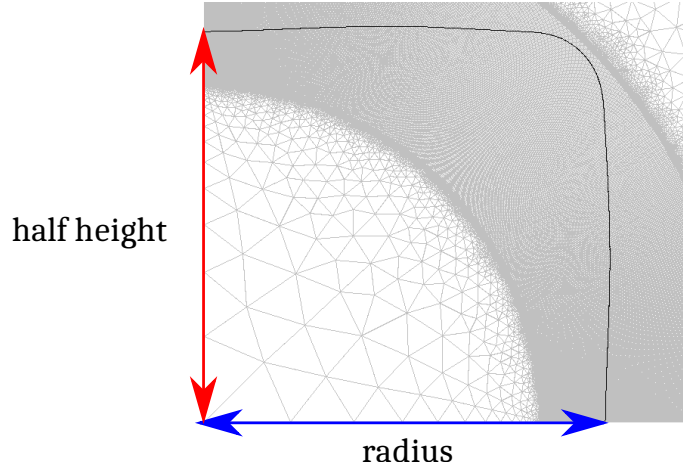


Figure 4.10: Height and radius definitions. Grey lines represent the mesh, black lines the air/ice interface at $t = 5500$ s. Height is measured at the center of the basal facet and radius at the center of the cylindrical facet.

Euler differentiation scheme. Both growth rates appear to be non constant. Both growth rates increase, but seem to reach a constant value at the end of the simulation. Globally, the simulated growth rates are in the range $2\text{-}12 \mu\text{m s}^{-1}$, which are about one tenth smaller than the experimental growth rates. Which is not surprising based on the approximations listed at the beginning of this section.

Figure 4.11.c) gives the evolution of the aspect ratio defined as the diameter divided by the height. It appears that the aspect ratio keeps increasing throughout the simulations. While the final time of simulation is too small to observe clear behavior, the current evolution is well fitted by an exponential transitory law of the form:

$$g(t) = (A_\infty - 1)(1 - e^{-\frac{t}{\tau_a}}) + 1 \quad (4.16)$$

with a value at infinity of $A_\infty = 1.16$, and a characteristic time of $\tau_a = 2 \text{ h } 35 \text{ min}$.

Finally, Figure 4.11.d) presents the evolution of the ratio of the diameter growth rate over the height growth rate. The rate ratio appears to decrease progressively. A correct fit can be obtained with a decreasing exponential transitory law of the form:

$$h(t) = (R_0 - R_\infty)e^{-\frac{t}{\tau_r}} + R_\infty \quad (4.17)$$

with a rate ratio at $t = 0$ of $R_0 = 7.6$, a value at infinity of $R_\infty = 1.49$ and a characteristic time of 13 min . Again, the simulation is too short to observe clearly the behavior at long times, and this fit only permits us to obtain an order of magnitude of the fitted value.

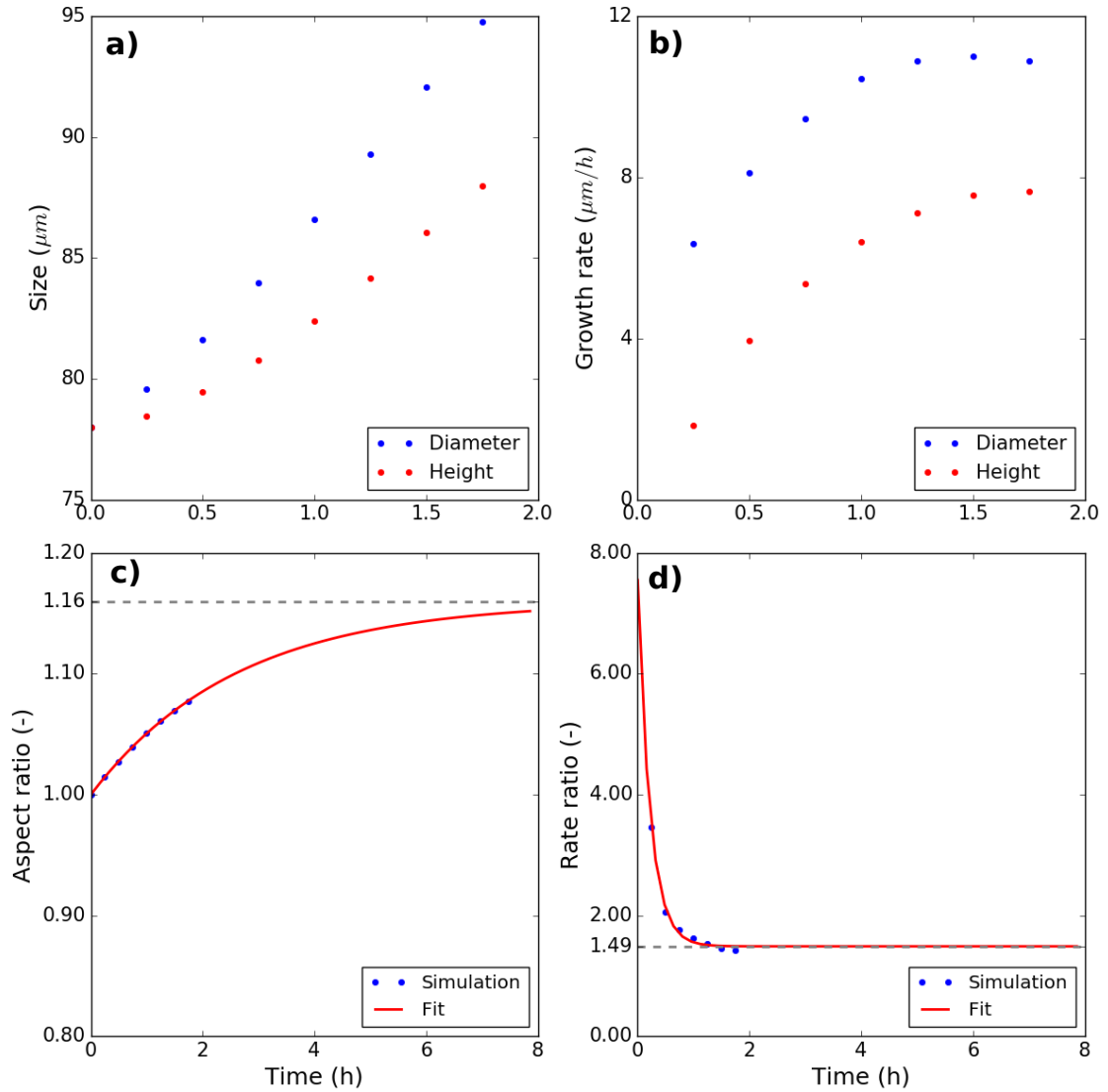


Figure 4.11: Quantitative data from the axisymmetric simulation. a) Evolution of diameter and height of the cavity. b) Growth rate of diameter and height. c) Aspect ratio defined as diameter divided by height (blue dots). Red curve is a fit to the data with function of the form given by equation (4.16) d) Ratio of diameter growth rate over height growth rate (blue dots). Red curve is a fit to the data with a function of the form given by equation (4.17).

4.4 Discussion

Experiment The experimental work enables us to obtain clearly defined and regular negative crystals. Each face appears to have a well defined velocity and can be accurately measured. However, the experiment suffered from two limitations. First, the pumping flow, and thus, the water vapor conditions imposed at the tip of the needle was not well known. This would be a stringent limitation if one would like to accurately model the growth rate of the faces. However, in the limit of the accuracy of the presented simulation, the different sizes measured followed well a

cubic root evolution. Thus, the water vapor flow was really likely not subjected to increasing or decreasing drifts. Secondly, limited by technical feasibility, the evolution on basal and prismatic faces had to be followed with two different samples. This experiment was a first attempt. Thus, the setup was kept simple. However, there is at least two possibilities to improve that point. One can use the same setup but with two cameras with crossed optical axis in order to image simultaneously both faces. Better still, the experiment could be conducted using X-ray microtomography to obtain 3D images of the growing cavity. This would permit accurate computation of size, volume, interface velocities, etc. This last solution appears particularly interesting as the simplicity of the system and the regularity of the negative crystal makes the experiment a nice validation test for modeling. In the limit of these uncertainties, the aspect ratio appears to remain constant with a value of about 2. This is consistent with the temperature of -10°C as it is not a high aspect ratio and this temperature is a transition temperature between plates and column as indicated by Nakaya's diagram. The rate ratio was in order of 2, also which is consistent with the aspect ratio. As the shape was well fitted by a function of the type given by equation (4.15), the ratio was constant over time. However, to describe the ratio accurately, particularly its evolution, would also require measurement of both growth rates on the same crystal.

Simulation For comparison to the experiment, a simulation of pumping in a monocrystalline ice block was performed. The anisotropy function used enables us to produce facets. However, several approximations have been made. The axial symmetry is a strong assumption as it can be seen from the experiment that the created cavity is clearly not cylindrical. However, all prismatic faces should physically behave similarly, while the basal and prismatic faces are different by nature. So, although the simulation does not take into account the complexity induced by the presence of six prismatic faces, it permits to study and test the model with faces of different nature.

In the simulation, we used a kinetic coefficient ratio of 6 between the two values of the minima. So, if the supersaturations near the faces are nearly equal, and the faces are flat with normals in the singular orientation, this should be the ratio of interface velocity too. The rate ratio actually corresponds approximately to r_{β} at the beginning of the simulation. However, the rate ratio decreases rapidly and becomes lower than 2. If the presented fit is realistic, the rate ratio would be 1.5 at longer times. This has to be explained either by supersaturation differences that counterbalance the kinetic differences, either by faces whose normals are not strictly in the singular directions. Figure 4.12 presents the saturation field at $t = 5500$ s. The observation of this data has to be done at two scales: at the bulk scale, the scale of the air cavity, and in the diffuse interface. When looking at the bulk supersaturation close to the interface, it appears that the supersaturation is similar at the proximity

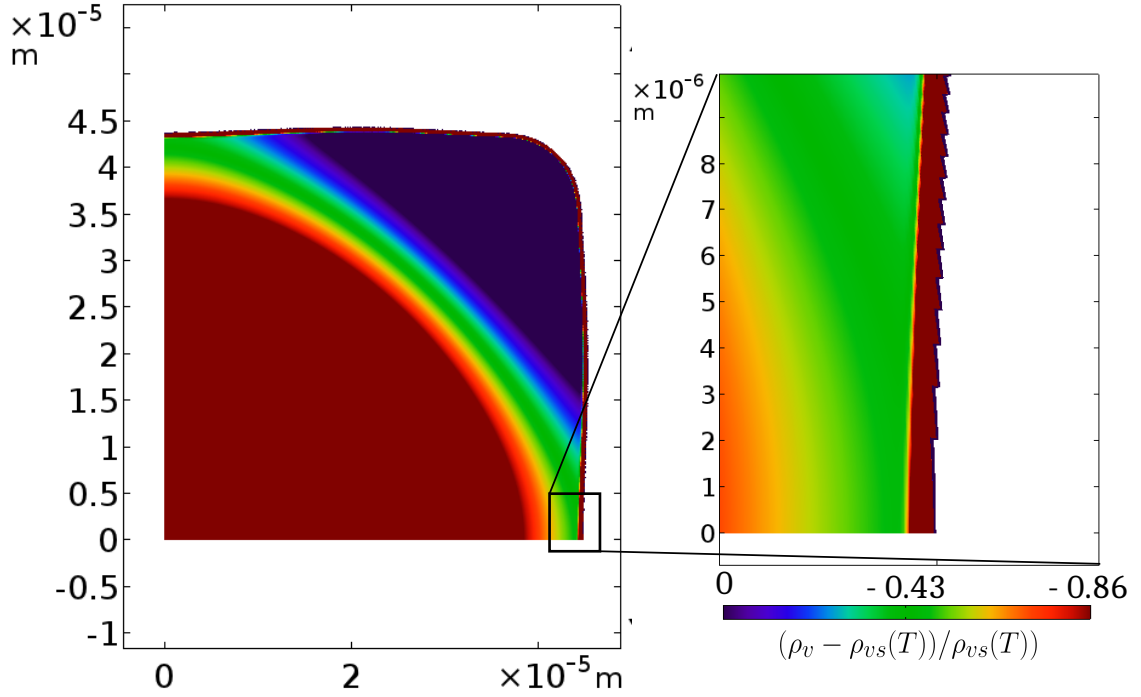


Figure 4.12: Supersaturation field obtained at $t = 5500$ s, at bulk scale (left) and at the scale of the diffuse interface (right).

of both faces. So this could not explain the discrepancies between the rate ratio and the kinetic coefficient ratio r_β . However, when looking to the diffuse interface, one can see that the supersaturation is subject to a discontinuity. That discontinuity appears uniform along the interface. This is unphysical and corresponds well to the jump in diffusive field at the interface condition described by *Almgren* [1999] also called the solute trapping anomaly [*Karma*, 2001]. This is typically due to a bad phase-field convergence. In other words, the interface width W appears to be too large for the sharp interface limit to be valid.

In addition, as the cavity is growing, the facets become convex. A consequence of this convexity is that a kinetic coefficient gradient exists along the face and such that the kinetic coefficient does not correspond exactly to the value for singular faces. Finally, the rate ratio is not directly linked to r_β . The weak phase-field convergence could be an explanation of the presence of this convexity, as one can expect several abnormal terms like surface diffusion or interface stretching to deform the interface. Additionally, as the corner appears relatively rounded in comparison to the cavity size, a possibility is that facets are not developed enough to be sufficiently flat. So, if this convexity is indeed due to the interaction between rounded corner and facets, it should be reduced by increasing the sharpness of the corner i.e. by increasing the strength of the anisotropy (i.e. decreasing δ , see *Uehara and Sekerka* [2003]) or by increasing the initial cavity size.

To do so, one would need to i) increase the anisotropy in the kinetic coefficient, which in turn would make the constraints on W stiffer, or ii) perform a simulation

on a larger cavity size and simulating for longer times. Therefore, we will obtain sufficiently important displacement of the faces in comparison to the initial radius.

Thus, this seems impractical with the current formulation as

- the value W is already really small in comparison to the geometrical length scales of the cavity
- the convergence of phase-field appears weak as the continuity condition at the interface is not verified for the supersaturation.
- the cost was already high: the simulation implied 700,000 degrees of freedom and took 30 h.

Instead, a correct simulation of the addressed problem would require us to develop better strategy in the numerical approach. There is indeed promising possibilities. The first is to develop a thin-interface formulation for the present model [*Karma and Rappel, 1998; Echebarria et al., 2004*]. This consists in performing the match asymptotics analysis and removing the abnormal second order terms by choosing appropriately the coefficients in equation (4.1) and the interpolation functions for κ , D , and C . We note that for the present physics, since there is unequal diffusivity for both u and T fields, this would require the addition of an anti-trapping current to remove all anomalies. Developing a thin-interface limit typically allows to use an interface thickness of the scale of the microstructure. In turn, this would permit to decrease drastically the computational time. Indeed, the grid elements typically scale as W and the characteristic time of the phase-field equation τ scales as W^2 , thus the computational time of simulations diverges as $W^{-(2+d)}$ where d is the dimension of the domain [*Karma and Rappel, 1998*].

An additional possibility to reduce computational time is to use adaptive mesh refinement techniques to benefit from the separation between the smooth interface scale and the microstructure scale. Actually, only the areas where ϕ varies require a fine mesh, thus adaptive mesh would permit us to reduce the thickness of the finely meshed zone to basically W , while in the present simulation it was $22/0.1 = 220 W$.

4.5 Conclusion

In order to obtain experimental data for modeling the kinetic faceting in ice/air systems, we performed an experiment of negative crystal growth, by pumping water vapor out from monocrystalline ice blocks through a needle for one day. The cavities reached sizes of the order of 2 mm and take the shape of a hexagonal prism with flat facets. The size evolution normal to basal faces and normal to prismatic faces has been measured, but on two distinct samples because of technical limitations. Globally, the aspect ratio appears to remain constant in the limit of the experiment duration and accuracy.

The experiment shows a good potential as a validation experiment as the formed crystals appear to be really regular, and the implied physics involves fundamental aspects of faceting while keeping the problem simple. From the perspective of obtaining accurate validation data, the experiment could be improved by an accurate measurement of the water vapor conditions imposed at the needle tip and by the use of X ray microtomography as this would permit an accurate 3D description of the evolution of the crystals.

For comparison, we performed simulations of the growth of an initially spherical cavity of radius $39\ \mu\text{m}$ in ice by means of phase-field method, accounting for kinetic faceting with highly anisotropic kinetic coefficient, with narrow minima. Simulations were performed under axial symmetry hypothesis so that kinetic coefficient is anisotropic only relative to the rotation axis. Two narrow minima with different values were used. As a result, the cavity grows, forming facets connected by rounded corners, and, thus, becomes cylindrical with time. However, the facets appeared lightly convex and the advancing rate ratio of the corresponding facets were not equal to the kinetic coefficient ratios between the two minima. These observations appear unphysical, and additionally, the continuity condition appeared to be not verified for the supersaturation field. This suggests that the phase-field convergence was not sufficient and that anomalies arising from the introduction of a diffuse interface were not small enough to allow a realistic simulation.

A more realistic simulation would require a better phase-field convergence, and to perform simulation of a larger cavity, for longer simulation times as the simulated behavior appeared to be transitory. However, this implies an increased computational cost with the current formulation. Further developments of the model would need to be performed before producing more realistic simulations. This include reformulation of the present model using a thin-interface limit and the use of adaptative mesh refinement technique as the problem implies intrinsically an important separation between the interface and microstructure scales.

Towards modeling of temperature gradient metamorphism

Abstract

Chapter 3 showed that the presented phase-field model with kinetic faceting reproduces well the experiment of negative crystal migration under a temperature gradient. Chapter 4 presents an attempt of setting the kinetic coefficient parameters with an experiment of negative crystal growth. It appears that high computational cost requires some strong assumptions that prevent quantitative simulations. In this chapter, we show on-going works on additional simulations that characterize the behavior of the present model. First, in section 5.1, we present simulations of temperature gradient metamorphism of an isolated grain and characterize the influence of grain size, temperature and temperature gradient amplitude. Then, in section 5.2, we present a qualitative simulation of negative crystal growth. By increasing the interface thickness W and accepting large errors in the phase-field convergence, we illustrate the potential of fully 3D simulations that show the eight faces of the hexagonal negative crystals.

5.1 2D axisymmetric simulation of temperature gradient metamorphism of a grain

5.1.1 Method

We propose to study the metamorphism of an isolated snow grain using the developed phase-field model accounting for kinetic anisotropy. In order to test the consistency of the model against the known trends of metamorphism, we propose to simulate the evolution of an initially spherical grain under a temperature gradient. In the simulations, we have:

- initial radius r_i of the grain in the range 10-100 μm

- mean temperature T_0 of -15°C , -10°C or -5°C
- temperature gradient amplitude G of 35°C m^{-1} , 70°C m^{-1} or 140°C m^{-1}

All the simulations were performed assuming axisymmetry around the c-axis. The kinetic coefficient function is characterised by $\beta_m = 2 \cdot 10^{-6} \text{ m s}^{-1}$, $\delta = 0.1$, $r_\beta = 1$ and $k = 4$. The domain consists of a rectangle of 6 mm in height and 3 mm in radius

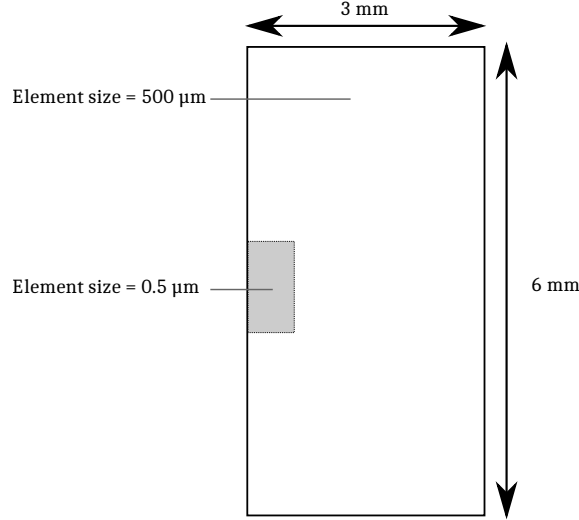


Figure 5.1: Representation of the computational domain. The mesh consists in regular quadrangle grid with element size of $0.5 \mu\text{m}$ in the grey area and in free triangles of size $500 \mu\text{m}$ in the rest of the domain.

(see Figure 5.1), with the left boundaries being the symmetry axis. Zero fluxes were imposed on the right boundary for all variables. Dirichlet conditions were imposed for temperature T and dimensionless water vapor concentration u on top and bottom boundaries. The temperature gradient was set from top (cold) to bottom (warm). On the top and bottom boundaries, the dimensionless concentration u was set to $u_{eq}(T) + \rho_{vs}(T, 1/r_i)/\rho_i$ so that the initial grain is in theoretical equilibrium with that boundary condition. Zero flux was imposed for the phase-field variable on top and bottom boundaries. An interface thickness of $W = 5 \times 10^{-7} \text{ m}$ was used, the mesh in a rectangle including the grain at all times consists in regular quadrangles of size W . The simulations were performed up to a final time of 48 h.

5.1.2 Results

Figure 5.2 presents for each temperature gradient (each columns) and each initial radius (each row) the interface for the three different temperatures after 48 h of metamorphism. Many observations can be done on these results:

- For a radii of $100 \mu\text{m}$ and $10 \mu\text{m}$, and temperature gradient of 70 K m^{-1} , facets appear clearly on bottom interface while the top interface remains rounded. This is typically the effect of a temperature gradient as deposition occurs on

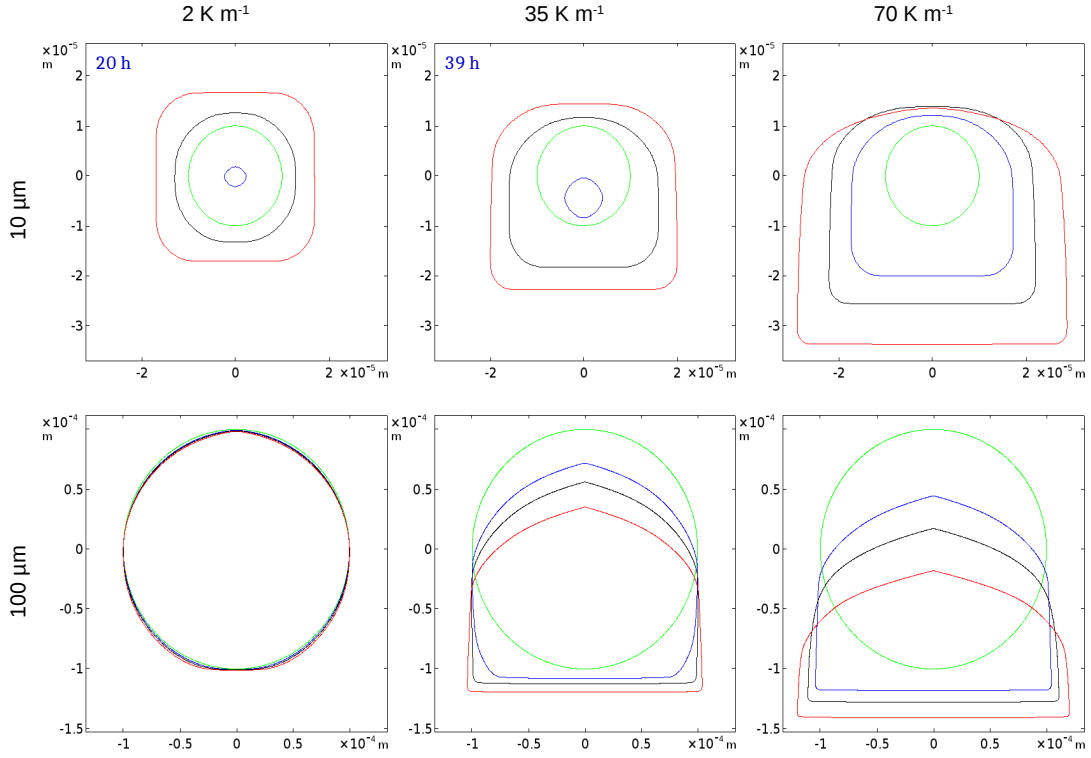


Figure 5.2: Variations in the evolutions of the metamorphism of a spherical grain under temperature gradient, varying its initial radius, temperature and temperature gradient. Green is the interface of the initial grain. Its radius is equal on each row. The imposed temperature gradient is equal in each column. Unless stated otherwise, this represents the final state after 48 h of metamorphism. Blue is the interface for $T_0 = -15$ °C. Black is the interface for $T_0 = -10$ °C. Red is the interface for $T_0 = -5$ °C.

the bottom which then becomes faceted while sublimation occurs on the top of the grain, and leads to rounding. This is consistent with the negative crystal experiment presented in chapter 3 and with other experiments on temperature gradient metamorphism [Akitaya, 1974; Flin and Brzoska, 2008; Pinzer et al., 2012].

- With a radius of $10\ \mu\text{m}$ and a temperature gradient of $2\ \text{°C m}^{-1}$ and $35\ \text{°C m}^{-1}$ the grain grows for temperatures of $-10\ \text{°C}$ and $-5\ \text{°C}$. However, it sublimates for $T_0 = -15\ \text{°C}$ after $t = 20\ \text{h}$ under $2\ \text{°C m}^{-1}$ and after $t = 39\ \text{h}$ under $35\ \text{°C m}^{-1}$. We attribute that to curvature effects, that are more pronounced with a smaller grain. Indeed, if one considers the limiting case where $G=0$, due to Kelvin effects, the grain is in unstable equilibrium with the prescribed boundary and initial conditions: a slight perturbation due to local sublimation will make the grain radius decrease, and, thus, the curvature increase, which makes the supersaturation decrease, and in turn, the grain sublimates even more. Similarly, a small initial deposition will make the grain grow. We think

that this sensibility to perturbation explains the difference in behavior (growth or decay) for the different temperatures under a temperature gradient of $2\text{ }^{\circ}\text{C m}^{-1}$.

- At $35\text{ }^{\circ}\text{C m}^{-1}$, the Kelvin effect is visible as the same unstability that can be observed between -15°C in one hand and $-10/-5^{\circ}\text{C}$ in the other hand. However, the effects of temperature gradient are also visible: when the grain grows (at 263 K and 268 K) the top is more rounded than the bottom, showing that the growth rate is smaller on the colder part. Additionally, when the grain sublimates (at 258 K) the migration towards the bottom is clearly visible. Thus, these results show an intermediate regime where both curvature and temperature gradient effects are visible.
- For all cases, a higher temperature leads to faster growth, and facets becomes more pronounced. The increase of growth rate with temperature is consistent with our knowledge on snow metamorphism [*Fierz et al.*, 2009]. It comes from the fact that ρ_{vs} increases exponentially with T so that a higher temperature leads to larger variations of ρ_{vs} and so quicker metamorphism. A consequence of this faster growth is that kinetic effects are more pronounced and facets are more marked.

We further developed that last point. While the temperature accelerates the metamorphism, one can wonder if the migration and the shape evolution is affected in the same manner by temperature, i.e. if an increase of temperature leads just to an increase of the evolution timescale or if the evolution route is different. To answer, for each couple (r_i, G) we search times of evolution at 263 K and 268 K where the bottom interface of the grain is at the same position than at $t = 48\text{ h}$ and $T = 258\text{ K}$, and compare the shape of the grain. The results are presented in Figure 5.3. One can see that for $r_i = 100\text{ }\mu\text{m}$, the three interfaces overlap almost perfectly. Thus, the evolution at the three different temperatures differs only by a timescale. However, for $r_i = 10\text{ }\mu\text{m}$, the center of the facets overlaps well but significant differences are visible at corners. We interpret this by the fact that the temperature acts on different time scales. Indeed, in that case, the kinetics effects dominate curvature effects because facets are clearly visible but with small margins. The growth rate differences between the three temperatures lead to sensibly different balance between these two effects and thus to a sensible different shape, particularly at the corners, where the curvature is higher. Thus, here, the temperature does not only change the timescale of the evolution, but also modifies the balance between curvature and kinetic effects.

5.1.3 Concluding remarks

The presented simulations are simple and are only qualitatively representative of snow metamorphism. However, these simulations permit us to show the behavior

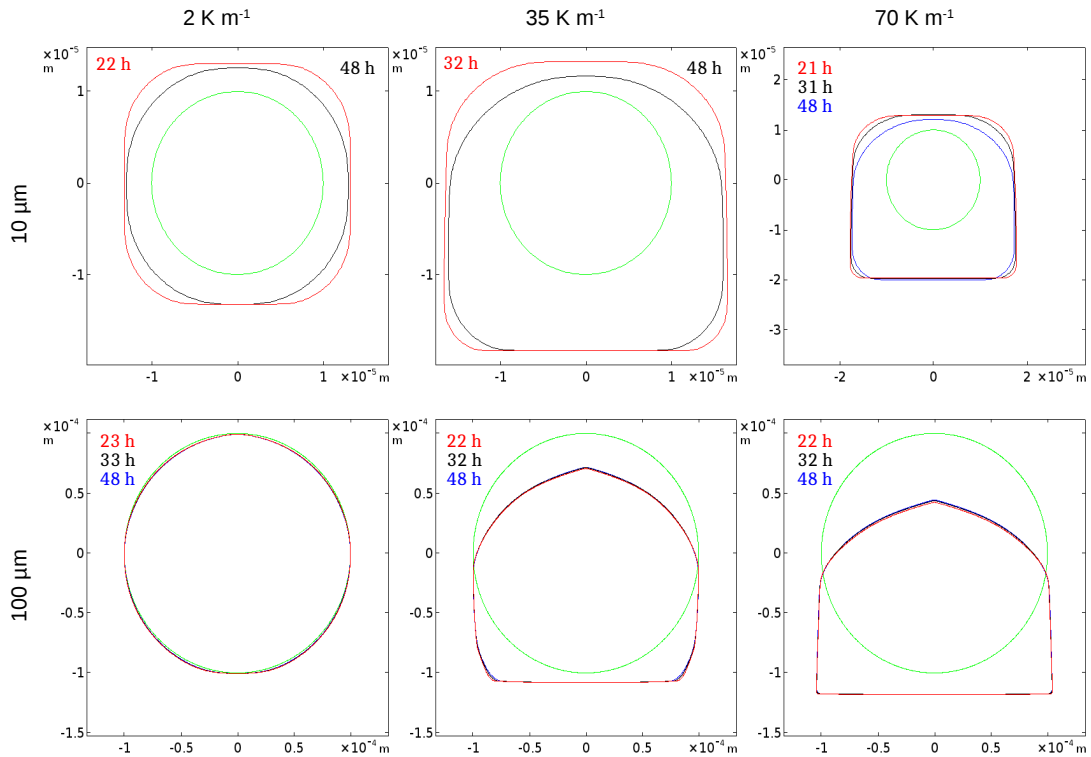


Figure 5.3: Influence of the temperature on the timescale of the evolution. For each couple of parameters (temperature gradient, initial radius), interfaces at different radius are compared with equal displacements. Blue corresponds to $T = 258$ K, black to $T = 263$ K and red to $T = 268$ K. The coloured times are the times of simulation for the corresponding temperature so that the bottom of the grains is at the same position.

of the model on several aspects of metamorphism. Particularly, several trends are reproduced physically and are:

- Faceting occurs on deposition areas while the interface remains rounded on the sublimating part.
- The higher is the growth rate, the more pronounced are the facets (the sharper are the corners). Particularly, a higher temperature gradient leads to a more faceted grain.
- A grain tends to grow under temperature gradient
- The larger is the initial grain, the sharper are the corners of final grain.
- The growth rate increases with temperature. Particularly, for a strongly faceted grains, evolution at different temperatures differs only by a global timescale.

5.2 3D simulation of anisotropy

The results presented in section 5.1 show that our model is qualitatively consistent with our understanding of dry snow metamorphism. However, in order to be more realistic, one should consider necessarily the 3D geometry of the crystal. Particularly, the 3D anisotropy of the kinetic coefficient should be able to reproduce hexagonal shapes as observed in snow metamorphism.

In this section, we illustrate the possibility of such 3D faceting with a simulation of negative crystal growth, that is qualitatively similar to the experiment presented in 4.3.1.

5.2.1 Method

Here, we present a coarse qualitative 3D simulation of the growth of a negative crystal, taking into account the 3D anisotropy of the kinetic coefficient, in order to produce basal and prismatic faces. Because it necessarily requires us to consider a 3D domain and there is an increased computational cost, we used an interface thickness of $W = 50 \mu\text{m}$ larger than the critical value for the phase-field convergence, of the order of $0.5 \mu\text{m}$. Thus, the results are expected to be qualitative only.

Let us define the anisotropy function

$$\tilde{q}(\theta) = \max \left[\tanh \left(\frac{k}{|\tan(\frac{\theta}{2} + \frac{\pi}{2})|} \right), \delta \right] \quad (5.1)$$

and express the kinetic coefficient as :

$$\beta(\theta, \psi) = \beta_{max} \cdot \tilde{q} \left(\theta - \frac{\pi}{2} \right) \cdot \prod_{i=0}^3 \tilde{q} \left(\sqrt{\left(\left(|\psi| - \frac{i\pi}{3} \right)^2 + \theta^2 \right)} \right) \quad (5.2)$$

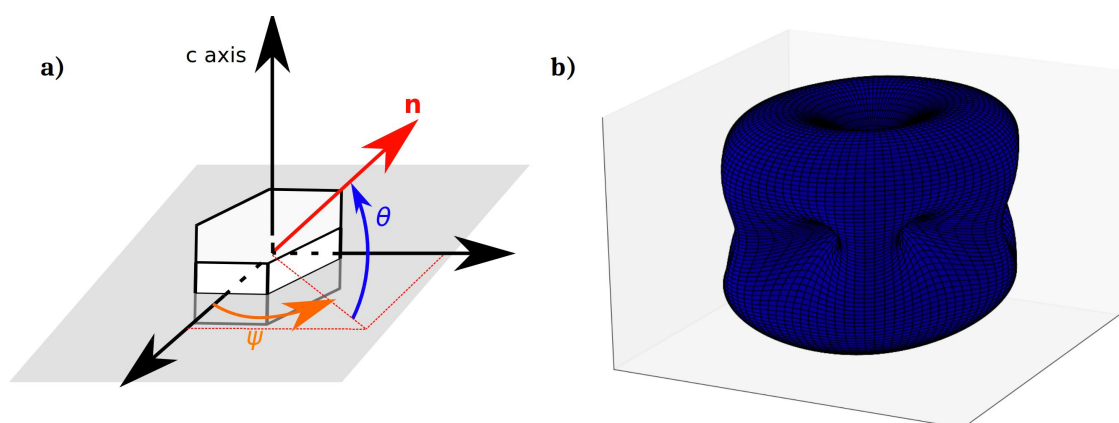


Figure 5.4: a) Definitions of angles ψ and θ relative to the crystalline orientation. b) Representation of the 3D anisotropy given by equation 5.2 in spherical coordinates.

where we have $\beta_{max} = 2 \times 10^{-6} \text{m s}^{-1}$, $\delta = 0.1$ and $k = 2$. Note that the kinetic coefficients in prismatic and basal directions are equal. A representation of that

function is then given in Figure 5.4. Thanks to symmetries in the problem, we can reduce the domain to a sector of a cylinder with aperture of $\frac{\pi}{6}$ so that the initial cavity and sink are centered at the lower corner of the edge of this sector. This, thus, permits us to divide by 24 the number of degrees of freedom. The part of the domain comprised between 100 μm and 200 μm from the center of the cavity was meshed with tetraedrons of 5 μm in size. The Dirichlet boundary condition was

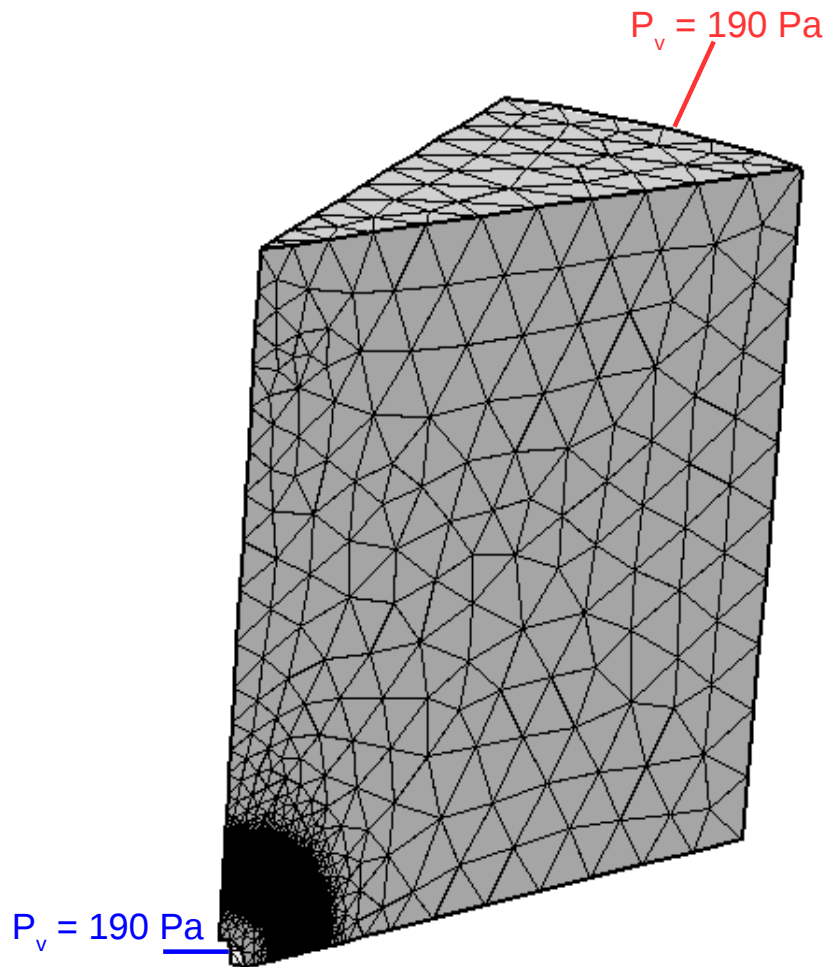


Figure 5.5: Representation of the domain used to perform the simulation

given for T on the cylindrical face of the domain. All others boundary conditions were zero fluxes. The initial state was assumed to be a cavity in a monocrystalline ice block, with a c -axis parallel to the edge of the cylindrical sector, i.e. with a kinetic coefficient expressed by equation (5.2). The cavity was initialised as being

spherical with a radius of $120\ \mu\text{m}$. The mean temperature was fixed to $T_0 = -4\ ^\circ\text{C}$. The growth was driven by a fixed partial pressure of water vapor fixed to $190\ \text{Pa}$ on a sphere of radius $50\ \mu\text{m}$.

5.2.2 Results

The evolution of the cavity is given in Figure 5.6. Cuts in the horizontal and vertical planes are shown in Figure 5.7. As we can see on both figures, the negative crystal grows with facets appearing in the direction of the minima in the kinetic coefficient function. The edge between prismatic and basal faces is correctly defined while some rounding is, however, visible. During the simulation, this edge keeps getting sharper with time. The edges between prismatic faces are clearly defined even at $t = 2\ \text{h}$ and appear really sharp. Facets are nicely visible. They appear to be really flat at $t = 2\ \text{h}$ and then become slightly concave with increasing time. Additionally, we observe some roughness appearing at early times of the simulation in the centers of the faces. With increasing time, that roughness gets smoothed out, collapsing into a pattern of 6-fold symmetry on basal faces and 4-fold symmetry on prismatic faces.

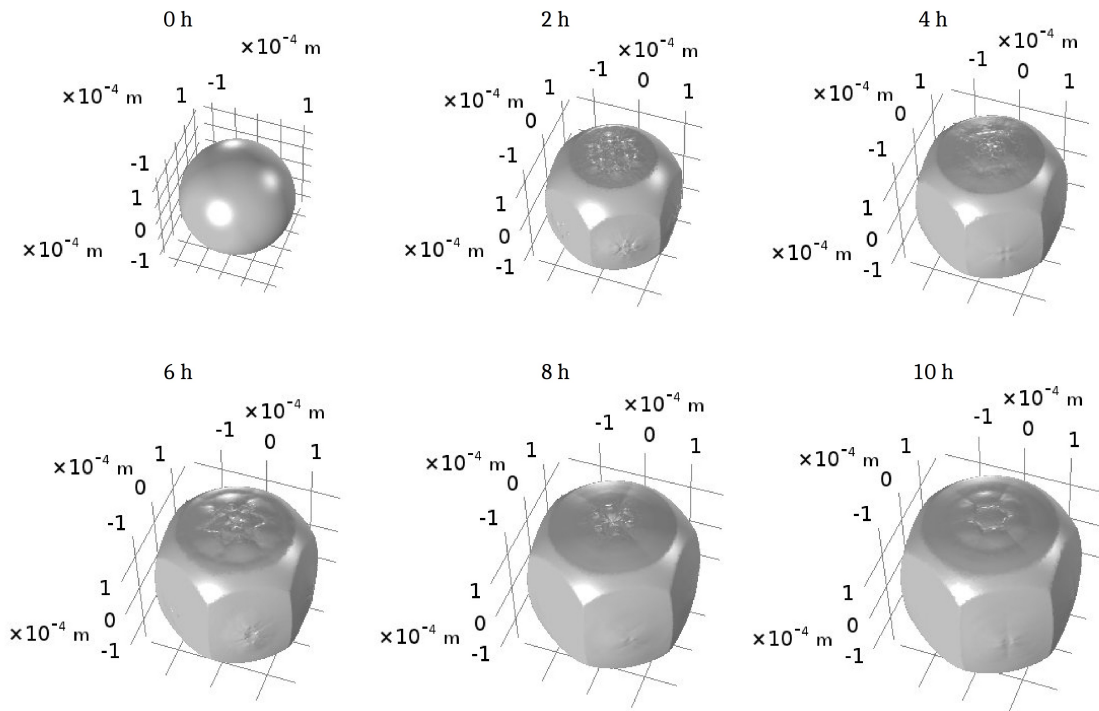


Figure 5.6: Simulation results for the growth of a 3D negative crystal accounting for anisotropy in the kinetic coefficient for prismatic and basal faces.

5.2.3 Discussion

From Figure 5.7, the interface speed is of the order of $v_n = 10^{-9}\ \text{m}\ \text{s}^{-1}$, which leads to a critical interface thickness for phase-field convergence of $10^{-7}\ \text{m}$. The

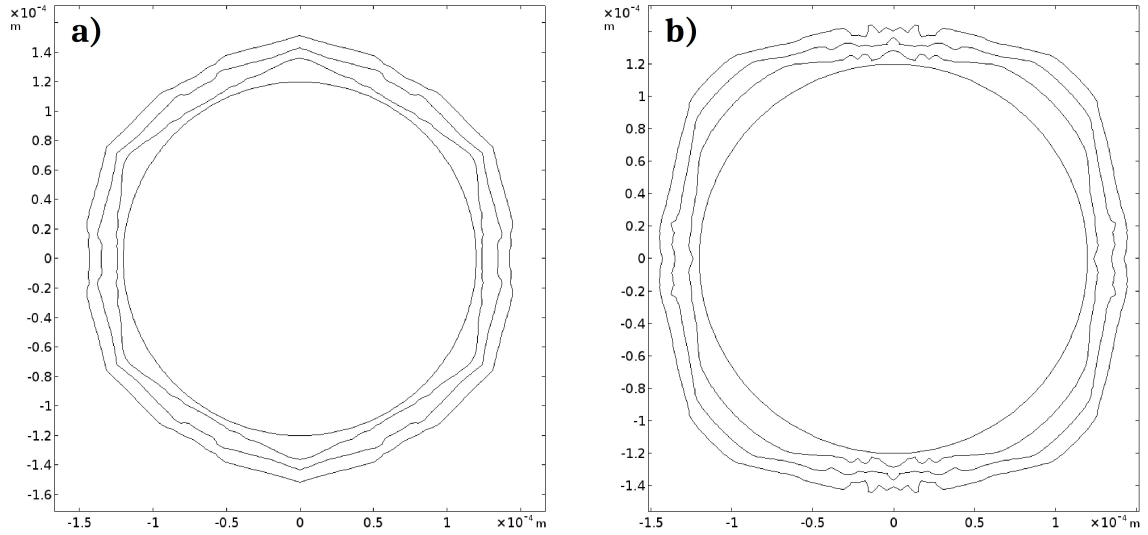


Figure 5.7: Simulation results for the growth of a negative crystal: cross-section of the 3D volume. a) Horizontal and b) vertical cuts of the 0 level set of phase-field function represented every 2 h of simulated time.

value of the interface thickness used here is then about 500 times larger than that critical value. Under these conditions, the phase-field formulation introduces, in principle, unphysical anomalies in the solution [Almgren, 1999]. Nonetheless, the cavity evolutions still behave consistently with experiment in some measures. The geometry is well reproduced as the cavity takes the shape of a hexagonal prism, with marked faces and edges. We think that the observed concavities can be due to the value of $k = 2$ used here. As shown by *Uehara and Sekerka* [2003] this parameter control the facet flatness. This parameter is physical and is linked to surface diffusion. So that parameter could be adjusted to fit experiment on that point. Similarly, the basal/prismatic edge appeared to be relatively smooth. This is probably due to the value of $\delta = 0.1$, as a smaller value would have increased that sharpness. That parameter is the anisotropy strength and is linked to step density variations with orientation, and may also be fitted to correctly reproduce the experiment. We explain the difference in apparent sharpness between prismatic and basal faces by the fact that the angle between prismatic faces is $\frac{2\pi}{3}$ while it is $\frac{\pi}{2}$ between prismatic and basal: prismatic facets require smaller times to be fully developed than basal facets.

The only observed feature that we can not explain physically, and thus we think is due to violations of phase-field convergence restrictions, is the apparent noise and patterns at face centers. The observable roughness corresponds well to the underlying mesh used. In simulations with smaller W , i.e. respecting the convergence conditions, such noise is not visible. So, we think that the large thickness of interface used here may create abnormal fluxes of heat and water vapor close to the interface, both in terms of intensity and direction. As for example, this could arise from the abnormal terms such as solute trapping, interface stretching, or surface diffusion. In

consequence, the flux may be unphysically excessively large, and may lead to an unstable numerical resolution with that mesh. It would be interesting to test finer meshes to see if that spurious effect may be suppressed while keeping reasonable computational cost. Interestingly, this roughness gets smoothed out with time. Possibly, this smoothing leads to the concavity of the faces. The origin of that smoothing can be due to the Allen-Cahn equation used in phase-field models, which is a diffusion-reaction equation. This illustrates the robustness of the phase-field formulation to numerical errors.

5.2.4 Concluding remarks

These qualitative simulations illustrates the potential of the phase-field model to simulate the 3D growth of crystals with kinetic faceting. The abnormal terms coming from the violation of the restrictions of phase-field convergence do not lead to qualitative unphysical results. However, it seems that unphysical fluxes arise from that approximation. Thus, an interesting perspective can be to perform such simulations, ignoring restrictions, and to compare with experiment in order to quantify the global discrepancy.

5.3 Conclusion

This chapter explored the behavior of the present phase-field model by simple simulations of spherical ice grains under a vapor flows imposed by a temperature gradient and by a qualitative 3D simulation of the growth of a negative crystal. It appears that the present model, with kinetic faceting reproduces well the expected trends. Particularly:

- the hexagonal symmetry can be simulated.
- Faceting occurs on grains where deposition occurs and rounding is maintained where sublimation takes place. This behavior is inverse for cavities.
- The metamorphism rate increases with temperature.
- With the parameters used, grains tend to grow under a temperature gradient.

Conclusion and perspectives

The global objective of the thesis was to improve the knowledge of kinetic-related effects during snow metamorphism. More precisely, we focused on the anisotropy of the kinetic coefficient relative to the ice crystal and its consequences under temperature gradient metamorphism. There were two main objectives:

- Experimental characterisation of the effects of differences in kinetic coefficient between basal and prismatic faces under temperature gradient metamorphism.
- Development of kinetic faceting in a numerical model, that would permits us to study the growth processes and their interactions with heat and mass diffusion. Particularly, the model should permit us to study transitions between rounded equilibrium forms and faceted kinetic forms.

6.1 Experiment of temperature gradient metamorphism observed with Diffraction Contrast Tomography

For the first time, we conducted an experiment of diffraction contrast tomography on temperature gradient metamorphism. The experiment has been performed at the European Synchrotron Radiation Facility. The experiment has required the modification of the cryogenic cell CellDyM to avoid spurious diffraction spots by the materials of the sample holder and to allow technical compliance with the beamline.

A snow sample of rounded grains with initial density of 476 kg m^{-3} was subject to temperature gradient of $17 \text{ }^\circ\text{C m}^{-1}$ for 1 day and then of $52 \text{ }^\circ\text{C m}^{-1}$ for 2 days at mean temperature of -2°C for 2 days and -4°C for 1 day. Image analysis permitted us to obtain an accurate description of the orientation distribution, compute local fluxes and study the relationship between local fluxes and the crystalline orientation. Several points may be made from this experiment:

- Crystalline orientations were successfully measured using DCT on about 900 growing and faceting grains.
- Local fluxes were computed at each point of the interface and are consistent with previous studies.
- Analyses show that the first mass transfers were globally higher on grains with the c-axis close to the horizontal plane, for both sublimation and deposition, thus confirming the hypothesis of orientation selective metamorphism, even at high density.
- When the temperature gradient was very well established, fluxes became almost independent of orientation for deposition, while differences remain for sublimation. We attribute this effect to grain to grain interactions, particularly present at that density, preventing further growth of crystals.

Perspectives The images obtained are ideal to serve as validation data for numerical models that would model the metamorphism at the scale of the REV, taking into account the polycrystalline nature of the microstructure along with its complex 3D geometry.

Additionally, one could reproduce the present experiment at lower density, e.g. of 200 kg m^{-3} , to obtain a more complete picture of the orientation selective activity in snow. In addition, it would be especially interesting to perform such kind an experiment for longer times as it would permit us to link the orientation-selective activity with the evolution of the orientation distribution with time. However, the technique is mainly used at synchrotrons whose beamtime is very difficult to obtain for longer periods than 2-3 days. So, an interesting perspective is to transpose the technique to laboratory tomographs as it would open the way to a more intensive and systematic characterisation of snow and ice crystalline structure.

The potential of the technique could also be developed further. Indeed, dynamic diffraction appear to occur as the ice crystals are nearly perfect. This, in turns, leads to intensities variations that may produce artefacts in the reconstruction procedure. The accuracy could be increased by managing such effects in the reconstruction process.

6.2 Modeling of kinetic faceting

The objective was to simulate faceting at the grain scale from crystal growth laws which of kinetic coefficient. In that end, we started from the phase-field approach of *Kaempfer and Plapp* [2009], and extend it to handle faceting. The model couples heat and water vapor diffusion to a phase change. The description of kinetic faceting has been done using highly anisotropic kinetic coefficient with narrow minima. The

analytical expression of the dependence upon the crystal orientation as a physical meaning has it represents the variation of the kinetic coefficient resulting from the variation of step density with orientation. In consequence, the parameters of the anisotropy function can be set from experiments or theories of ice crystal growth.

In chapter 3, the simulation of the migration of an air cavity in a monocrystalline ice block under a temperature gradient has been performed and compared to the corresponding experiment observed by time-lapse tomography. Experimentally, X-ray microtomography has been used to monitor the evolution of the cavity. By performing image analysis on the acquired 3D images, this has permitted to quantitatively characterize the cavity evolution in terms of displacement and shape. The model compares well with the experiment. Indeed, in both cases:

- A facet appears on the sublimating side while the cavity stays rounded on the deposition side.
- The faceting is associated with a flattening of the cavity in the direction of the temperature gradient.
- The volume is conserved.
- The speeds of migration are constant and are equal within a factor of 2.4.

Additionally, the comparison with simulations taking into account isotropy shows that i) faceting is due to kinetic coefficient, and that ii) the evolution is not diffusion-limited.

In chapter 4, we compared a simulation of negative crystal growth to the corresponding experiment monitored by optical microscopy. The experiment was performed by pumping water vapor out from monocrystalline ice blocks through a needle for one day. Again, by performing image analysis on the acquired images, we obtained important experimental data for modeling the kinetic faceting in ice/air systems. The cavity reaches sizes of the order of 2 mm and takes the shape of a hexagonal prism with flat facets. The evolution of the size normal to basal faces and normal to prismatic faces have been measured. Globally, the aspect ratio appears to remain constant (about 2) in the limit of the experiment duration and accuracy.

The simulation was performed with an initially spherical cavity of radius 39 μm under an axial symmetry hypothesis so that the kinetic coefficient is anisotropic only relative to the rotation axis. Two narrow minima with different values were used. As a result, the cavity grows, forming facets connected by rounded corners, and, thus, becoming cylindrical with time. However, the facets appeared slightly convex and the advancing rate ratio of the corresponding facets were not equal to the kinetic coefficient ratio between the two minimums. These observations appear unphysical, and additionally, the continuity condition appeared to be not verified for

the supersaturation field. This suggests that the phase-field convergence was not sufficient and that anomalies arising from the introduction of a diffuse interface were not small enough to allow realistic simulation.

In chapter 5, we presented additional numerical investigations using the phase-field model. We first focused on simulations of the evolution of an ice grain subject to a temperature gradient. We studied the evolution of the grain depending on i) its initial radius, ii) the mean temperature and iii) the temperature gradient. Several trends of snow metamorphism are very well reproduced:

- Faceting occurs on deposition areas while the interface remains rounded on the sublimating part.
- The higher is the growth rate, the more pronounced are the facets (the sharper are the corners). Particularly, a higher temperature gradient leads to a more faceted grain.
- Grains tend to grow under temperature gradient, at least for the tested parameters of our study.
- The larger is the initial grain, the sharper are the corners of the final grain.
- The growth rate increases with temperature. Particularly, for strongly faceted grains, the evolution at different temperatures differs only by a global timescale.

Finally, we illustrated the potential of the proposed phase-field model with the 3D growth of a negative crystal with kinetic faceting, by using a large interface width. The abnormal terms coming from the violations of the restrictions of the phase-field convergence do not lead to qualitatively unphysical results and the cavity exhibits hexagonal facets as it grows.

Perspectives for modeling Quantitative predictions appeared to be difficult with the current state of development. Proper quantitative simulations would require:

- 3D simulations, taking into account the hexagonal structure of ice
- Simulations at the size of the experiment
- Use of more physical kinetic coefficients

All of these three points increase the computational cost, the first two because they increase the size of the simulation domain, and the last one because the constraint on W depends on the kinetic coefficient and different values would reduce the grid size and timesteps. In addition, experimental measurements of the kinetic coefficient come with large uncertainties (see e.g. *Libbrecht [2004]*).

The computational cost could be largely reduced by the use of a thin-interface limit, with the addition of an anti-trapping current. This consist in choosing i) adequate interpolation functions in the material properties and ii) adequate phase-field parameters in order to remove spurious terms appearing at second order in the matched asymptotics expansion. The thin-interface limit typically permits us to use an interface thickness of the size of the radius of curvature in the microstructure. Thus, the computational time, which typically diverges as $\mathcal{O}(W^{-5})$ in 3D domains, could be reduced by several order of magnitudes. Additionally, the phase-field approach is intrinsically multi-scale, and efficient adaptative mesh refinement techniques could bring additional significant gain. Thus, quantitative simulations would be possible.

This would open additional interesting perspectives. For example, it would permit us to model snow metamorphism on a large sample representative of a snow layer. Additionally, the present model does not assume predominance of diffusion or kinetics on each other and the asymptotic analysis shows the physical consistency of the reformulation of the Stefan problem. So, one can expect that such a numerical model would permit us to estimate more accurately the kinetic coefficient from experiments.

An additional perspective is to apply multi phase-field formulation to the present model. This would permit us, for example, to take into account several crystalline orientations and open the way for understanding of phenomena at the grains boundaries.

Finally, it could be interesting to implement anisotropy in the surface tension along with anisotropy in the kinetic coefficients. Indeed, this anisotropy is basicaly poorly characterised experimentally. Numerical simulations would allow clarifying its implication in the picture of snow metamorphism.

List of publications resulting from this thesis

Peer-reviewed publications

- Granger R. et. al. :Orientation selective grain activity in snow under temperature gradient metamorphism observed with Diffraction Contrast Tomography. In preparation.
- Granger R. et. al.: Kinetic faceting with phase-field model for snow metamorphism. In preparation.
- Granger R. et. al.: Adjusting phase-field simulations to an experiment of negative crystal growth at -10°C . In preparation.

International Conferences

- Granger R., Geindreau C. and Flin F.: Air cavity migration in ice as a case study for temperature gradient metamorphism of snow: time lapse X-ray microtomography observation and phase-field simulations. 14th International Conference on the Physics and Chemistry of Ice (PCI 2018), Zürich, Switzerland. 7-12 January 2018. Talk.
- Granger R., Geindreau C., Flin F., Ludwig W., Hammad I., Rolland Du Roscoat S., Philip A., Lahoucine F., Lapalus P., Pézard L., Roulle J., Burr A., Dufour A., Hagenmuller P., Peinke I. and Tafforeau P. : Time-lapse Diffraction Contrast Tomography of snow temperature gradient metamorphism. International Conference on Tomography of Materials & Structures (ICTMS 2019). Cairns, Australia. 22-26 July 2019. Talk.
- Granger R., Geindreau C. Flin F., Ando E., Calonne N., Charrier P., Dufour A., Furukawa Y., Lesaffre B., Pézard L., Philip A., Rolland Du Roscoat S., Roulle J. and Hagenmuller P: Air bubble migration and faceting in ice: X-ray tomography observations vs phase field modeling. International Conference on Tomography of Materials & Structures. 22-26 July 2019 (ICTMS 2019). Cairns, Australia. Talk.

Seminars

- Granger R. Geindreau C. and Flin F.: Air cavity migration in ice as a case study for temperature gradient metamorphism of snow: time lapse X-ray microtomography observation and phase-field simulations. Atelier Neige OSUG. Centre d'Études de la Neige. 20th October 2017. Talk.
- Granger R., Flin F. and Geindreau C., Phase field modeling of snow metamorphism. Workshop sur la simulation numérique par éléments finis avec interfaces. Laboratoire Sols, Solides, Structures, Risques. 16th March, 2017. Talk.



Bibliography

- Adams, E. E., and D. A. Miller, Ice crystals grown from vapor onto an orientated substrate: application to snow depth-hoar development and gas inclusions in lake ice, *Journal of Glaciology*, 49(164), 8–12, doi:10.3189/172756503781830953, 2003.
- Akitaya, E., Studies on depth hoar, *Contributions from the Institute of Low Temperature Science*, 26, 1–67, 1974.
- Almgren, R. F., Second-order phase field asymptotics for unequal conductivities, *SIAM Journal on Applied Mathematics*, 59(6), 2086–2107, 1999.
- Armstrong, R. L., Some observations on snowcover temperature patterns, *Natural Resource Council, Canadian Associate Committee on Geotechnical Research, Tech. Memo*, 133, 66–81, 1981.
- Arons, E., and S. Colbeck, Geometry of heat and mass transfer in dry snow: A review of theory and experiment, *Reviews of Geophysics*, 33(4), 463–493, 1995.
- Asakawa, H., G. Sazaki, K. Nagashima, S. Nakatsubo, and Y. Furukawa, Two types of quasi-liquid layers on ice crystals are formed kinetically, *Proceedings of the National Academy of Sciences*, 113(7), 1749–1753, doi:10.1073/pnas.1521607113, 2016.
- Barrett, J. W., H. Garcke, and R. Nürnberg, Numerical computations of faceted pattern formation in snow crystal growth, *Physical Review E*, 86(1), 011,604, 2012.
- Bartels-Rausch, T., et al., A review of air–ice chemical and physical interactions (AICI): Liquids, quasi-liquids, and solids in snow, *Atmospheric chemistry and physics*, 14(3), 1587–1633, 2014.
- Bartelt, P., and M. Lehning, A physical SNOWPACK model for the Swiss avalanche warning: Part I: Numerical model, *Cold Regions Science and Technology*, 35(3), 123–145, 2002.

- Baruchel, J., et al., Synchrotron X-ray imaging for crystal growth studies, *Comptes Rendus Physique*, 14(2-3), 208–220, 2013.
- Bentley, W. A., and W. J. Humphries, *Snow Crystals. 1931*, New York: McGraw-Hill, 1931.
- Blackford, J. R., Sintering and microstructure of ice: A review, *Journal of Physics D: Applied Physics*, 40(21), R355, 2007.
- Bretin, E., R. Denis, F. Flin, J.-O. Lachaud, E. Oudet, and T. Roussillon, *Discrete-Continuous Approach for Deformable Partitions*, Technical, 2015.
- Brun, E., E. Martin, V. Simon, C. Gendre, and C. Coleou, An Energy and Mass Model of Snow Cover Suitable for Operational Avalanche Forecasting, *Journal of Glaciology*, 35(121), 333–342, doi:10.3189/S0022143000009254, 1989.
- Brun, E., P. David, M. Sudul, and G. Brunot, A numerical model to simulate snow-cover stratigraphy for operational avalanche forecasting, *Journal of Glaciology*, 38(128), 13–22, doi:10.3189/S0022143000009552, 1992.
- Brzoska, J.-B., C. Coléou, and B. Lesaffre, Thin-sectioning of wet snow after flash-freezing, *Journal of Glaciology*, 44(146), 54–62, 1998.
- Brzoska, J. B., C. Coléou, B. Lesaffre, S. Borel, O. Brissaud, W. Ludwig, E. Boller, and J. Baruchel, 3D visualization of snow samples by microtomography at low temperature, *ESRF Newsletter*, 32(22-23), 112, 1999a.
- Brzoska, J. B., B. Lesaffre, C. Coléou, K. Xu, and R. A. Pieritz, Computation of 3D curvatures on a wet snow sample, *The European Physical Journal-Applied Physics*, 7(1), 45–57, 1999b.
- Brzoska, J. B., F. Flin, and N. Ogawa, Using Gaussian curvature for the 3D segmentation of snow grains from microtomographic data, in *Physics and Chemistry of Ice*, p. 125, 2007.
- Burton, W.-K., N. Cabrera, and F. Frank, The growth of crystals and the equilibrium structure of their surfaces, *Phil. Trans. R. Soc. Lond. A*, 243(866), 299–358, 1951.
- Calonne, N., Physique des métamorphoses de la neige sèche: De la microstructure aux propriétés macroscopiques, PhD Thesis, Grenoble, 2014.
- Calonne, N., F. Flin, S. Morin, B. Lesaffre, S. R. du Roscoat, and C. Geindreau, Numerical and experimental investigations of the effective thermal conductivity of snow, *Geophysical Research Letters*, 38(23), 2011.
- Calonne, N., C. Geindreau, F. Flin, S. Morin, B. Lesaffre, S. Rolland du Roscoat, and P. Charrier, 3-D image-based numerical computations of snow permeability: Links

- to specific surface area, density, and microstructural anisotropy, *The Cryosphere*, *6*(5), 939–951, doi:<https://doi.org/10.5194/tc-6-939-2012>, 2012.
- Calonne, N., F. Flin, C. Geindreau, B. Lesaffre, and S. Rolland du Roscoat, Study of a temperature gradient metamorphism of snow from 3-D images: Time evolution of microstructures, physical properties and their associated anisotropy, *The Cryosphere*, *8*(6), 2255–2274, doi:<https://doi.org/10.5194/tc-8-2255-2014>, 2014a.
- Calonne, N., C. Geindreau, and F. Flin, Macroscopic Modeling for Heat and Water Vapor Transfer in Dry Snow by Homogenization, *The Journal of Physical Chemistry B*, *118*(47), 13,393–13,403, doi:[10.1021/jp5052535](https://doi.org/10.1021/jp5052535), 2014b.
- Calonne, N., M. Montagnat, M. Matzl, and M. Schneebeli, The layered evolution of fabric and microstructure of snow at Point Barnola, Central East Antarctica, *Earth and Planetary Science Letters*, *460*, 293–301, 2017.
- Calonne, N., et al., CellDyM: A room temperature operating cryogenic cell for the dynamic monitoring of snow metamorphism by time-lapse X-ray microtomography, *Geophysical Research Letters*, *42*(10), 3911–3918, 2015.
- Chernov, A., Stability of faceted shapes, *Journal of Crystal Growth*, *24*, 11–31, 1974.
- Chernov, A. A., Roughening and melting of crystalline surfaces, *Progress in crystal growth and characterization of materials*, *26*, 195–218, 1993.
- Cho, N., and J. Hallett, Epitaxial ice crystal growth on covellite (CuS) I. Influence of misfit strain on the growth of non-thickening crystals, *Journal of crystal growth*, *69*(2-3), 317–324, 1984a.
- Cho, N., and J. Hallett, Epitaxial ice crystal growth on covellite (CuS) II. Growth characteristics of basal plane steps, *Journal of crystal growth*, *69*(2-3), 325–334, 1984b.
- Choukroun, M., and O. Grasset, Thermodynamic model for water and high-pressure ices up to 2.2 GPa and down to the metastable domain, *The Journal of chemical physics*, *127*(12), 124,506, 2007.
- Colbeck, S., An overview of seasonal snow metamorphism, *Reviews of Geophysics*, *20*(1), 45–61, 1982.
- Colbeck, S., Theory of metamorphism of dry snow, *Journal of Geophysical Research: Oceans*, *88*(C9), 5475–5482, 1983a.
- Colbeck, S., Ice crystal morphology and growth rates at low supersaturations and high temperatures, *Journal of Applied Physics*, *54*(5), 2677–2682, 1983b.
- Colbeck, S., A review of the metamorphism and classification of seasonal snow cover crystals, *IAHS Publication*, *162*, 3–24, 1987.

- Colbeck, S., The vapor diffusion coefficient for snow, *Water resources research*, 29(1), 109–115, 1993.
- Colbeck, S. C., Thermodynamics of snow metamorphism due to variations in curvature, *Journal of Glaciology*, 26(94), 291–301, 1980.
- Colbeck, S. C., Temperature dependence of the equilibrium form of ice, *Journal of crystal growth*, 72(3), 726–732, 1985.
- Colbeck, S. C., and J. B. Jamieson, The formation of faceted layers above crusts, *Cold Regions Science and Technology*, 33(2-3), 247–252, 2001.
- De Quervain, M. R., Snow structure, heat and mass flux through snow, *The role of snow and ice in hydrology*, 105(14), 203, 1973.
- de Quervain, M. R., The Institute for Snow and Avalanche Research at Weissfluhjoch/Davos: The First Five Years (1943 to 1948), *Annals of Glaciology*, 4, 307–314, doi:10.3189/S0260305500005814, 1983.
- Demange, G., H. Zapolsky, R. Patte, and M. Brunel, A phase field model for snow crystal growth in three dimensions, *npj Computational Materials*, 3(1), 15, 2017.
- Desarnaud, J., H. Derluyn, J. Carmeliet, D. Bonn, and N. Shahidzadeh, Hopper Growth of Salt Crystals, *The Journal of Physical Chemistry Letters*, 9(11), 2961–2966, doi:10.1021/acs.jpcllett.8b01082, 2018.
- Dominé, F., T. Lauzier, A. Cabanes, L. Legagneux, W. F. Kuhs, K. Techmer, and T. Heinrichs, Snow metamorphism as revealed by scanning electron microscopy, *Microscopy research and technique*, 62(1), 33–48, 2003.
- Echebarria, B., R. Folch, A. Karma, and M. Plapp, Quantitative phase-field model of alloy solidification, *Physical Review E*, 70(6), 061,604, 2004.
- Eggleston, J. J., G. B. McFadden, and P. W. Voorhees, A phase-field model for highly anisotropic interfacial energy, *Physica D: Nonlinear Phenomena*, 150(1-2), 91–103, 2001.
- Elbaum, M., Roughening transition observed on the prism facet of ice, *Physical review letters*, 67(21), 2982, 1991.
- Erbe, E. F., A. Rango, J. Foster, E. G. Josberger, C. Pooley, and W. P. Wergin, Collecting, shipping, storing, and imaging snow crystals and ice grains with low-temperature scanning electron microscopy, *Microscopy research and technique*, 62(1), 19–32, 2003.
- Fierz, C., R. L. Armstrong, Y. Durand, P. Etchevers, E. Greene, D. M. McClung, K. Nishimura, P. K. Satyawali, and S. A. Sokratov, *The International Classification for Seasonal Snow on the Ground*, vol. 5, UNESCO/IHP, 2009.

- Fisher, N. I., T. Lewis, and B. J. J. Embleton, *Statistical Analysis of Spherical Data*, Cambridge University Press, 1993.
- Flin, F., and J.-B. Brzoska, The temperature-gradient metamorphism of snow: Vapour diffusion model and application to tomographic images, *Annals of Glaciology*, *49*, 17–21, 2008.
- Flin, F., J.-B. Brzoska, B. Lesaffre, C. Coléou, and R. A. Pieritz, Full three-dimensional modelling of curvature-dependent snow metamorphism: First results and comparison with experimental tomographic data, *Journal of Physics D: Applied Physics*, *36*(10A), A49, 2003.
- Flin, F., J.-B. Brzoska, B. Lesaffre, C. Coléou, and R. A. Pieritz, Three-dimensional geometric measurements of snow microstructural evolution under isothermal conditions, *Annals of glaciology*, *38*, 39–44, 2004.
- Flin, F., B. Lesaffre, A. Dufour, L. Gillibert, A. Hasan, S. Rolland du Roscoat, S. Cabanes, and P. Pugliese, On the computations of specific surface area and specific grain contact area from snow 3D images, *Physics and chemistry of ice*, pp. 321–328, 2011.
- Flin, F., R. Denis, C. Mehu, N. Calonne, B. Lesaffre, A. Dufour, and R. Granger, Isothermal Metamorphism of Snow, *Image*, *10*(11), 14–14, 2018.
- Flin, F., et al., An adaptative filtering method to evaluate normal vectors and surface areas of 3d objects. Application to snow images from X-ray tomography, *IEEE Transactions on Image Processing*, *14*(5), 585–596, 2005.
- Furukawa, Y., Snow and ice crystal growth, in *Handbook of Crystal Growth (Second Edition)*, pp. 1061–1112, Elsevier, 2015.
- Furukawa, Y., and S. Kohata, Temperature dependence of the growth form of negative crystal in an ice single crystal and evaporation kinetics for its surfaces, *Journal of crystal growth*, *129*(3-4), 571–581, 1993.
- Furukawa, Y., and J. Wettlaufer, Snow and Ice Crystals, *Physics Today - PHYS TODAY*, *60*, doi:10.1063/1.2825081, 2007.
- Good, W., Thin sections, serial cuts and 3-D analysis of snow, *IAHS Publ*, *162*, 35–48, 1987.
- Greenwood, M., K. Shampur, N. Ofori-Opoku, T. Pinomaa, L. Wang, S. Gurevich, and N. Provatas, Quantitative 3D phase field modelling of solidification using next-generation adaptive mesh refinement, *Computational Materials Science*, *142*, 153–171, 2018.

- Hagenmuller, P., G. Chambon, B. Lesaffre, F. Flin, and M. Naaïm, Energy-based binary segmentation of snow microtomographic images, *Journal of Glaciology*, 59(217), 859–873, 2013.
- Hammonds, K., and I. Baker, Investigating the thermophysical properties of the ice–snow interface under a controlled temperature gradient Part II: Analysis, *Cold Regions Science and Technology*, 125, 12–20, 2016.
- Hammonds, K., R. Lieb-Lappen, I. Baker, and X. Wang, Investigating the thermophysical properties of the ice–snow interface under a controlled temperature gradient: Part I: Experiments & Observations, *Cold Regions Science and Technology*, 120, 157–167, 2015.
- Hobbs, P. V., and B. J. Mason, The sintering and adhesion of ice, *Philosophical Magazine*, 9(98), 181–197, 1964.
- Kaempfer, T. U., and M. Plapp, Phase-field modeling of dry snow metamorphism, *Physical Review E*, 79(3), 031,502, 2009.
- Kaempfer, T. U., and M. Schneebeli, Observation of isothermal metamorphism of new snow and interpretation as a sintering process, *Journal of Geophysical Research: Atmospheres*, 112(D24), 2007.
- Karma, A., Phase-field formulation for quantitative modeling of alloy solidification, *Physical Review Letters*, 87(11), 115,701, 2001.
- Karma, A., and W.-J. Rappel, Quantitative phase-field modeling of dendritic growth in two and three dimensions, *Physical review E*, 57(4), 4323, 1998.
- Ketcham, W. M., and P. V. Hobbs, Step growth on ice during the freezing of pure water, *Philosophical Magazine*, 18(153), 659–661, 1968.
- Kingery, W. D., Regelation, surface diffusion, and ice sintering, *Journal of Applied Physics*, 31(5), 833–838, 1960.
- Knight, C. A., Ice growth from the vapor at- 5° C, *Journal of the Atmospheric Sciences*, 69(6), 2031–2040, 2012.
- Knight, C. A., and N. C. Knight, " Negative" Crystals in Ice: A Method for Growth, *Science*, 150(3705), 1819–1821, 1965.
- Kobayashi, R., Modeling and numerical simulations of dendritic crystal growth, *Physica D: Nonlinear Phenomena*, 63(3-4), 410–423, 1993.
- Kobayashi, T., The growth of snow crystals at low supersaturations, *The Philosophical Magazine: A Journal of Theoretical Experimental and Applied Physics*, 6(71), 1363–1370, doi:10.1080/14786436108241231, 1961.

- Kossel, W., Zur theorie des kristallwachstums, *Nachrichten von der Gesellschaft der Wissenschaften zu Göttingen, Mathematisch-Physikalische Klasse*, 1927, 135–143, 1927.
- Krol, Q., and H. Löwe, Analysis of local ice crystal growth in snow, *Journal of Glaciology*, 62(232), 378–390, 2016.
- Kuroda, T., and R. Lacmann, Growth kinetics of ice from the vapour phase and its growth forms, *Journal of Crystal Growth*, 56(1), 189–205, doi:10.1016/0022-0248(82)90028-8, 1982.
- Kuroiwa, D., A study of ice sintering, *Tellus*, 13(2), 252–259, 1961.
- Legagneux, L., and F. Domine, A mean field model of the decrease of the specific surface area of dry snow during isothermal metamorphism, *Journal of Geophysical Research: Earth Surface*, 110(F4), 2005.
- Legagneux, L., A.-S. Taillandier, and F. Domine, Grain growth theories and the isothermal evolution of the specific surface area of snow, *Journal of applied physics*, 95(11), 6175–6184, 2004.
- Lehning, M., P. Bartelt, B. Brown, and C. Fierz, A physical SNOWPACK model for the Swiss avalanche warning: Part III: Meteorological forcing, thin layer formation and evaluation, *Cold Regions Science and Technology*, 35(3), 169–184, 2002a.
- Lehning, M., P. Bartelt, B. Brown, C. Fierz, and P. Satyawali, A physical SNOWPACK model for the Swiss avalanche warning: Part II. Snow microstructure, *Cold regions science and technology*, 35(3), 147–167, 2002b.
- Lehning, M., I. Völksch, D. Gustafsson, T. A. Nguyen, M. Stähli, and M. Zappa, ALPINE3D: A detailed model of mountain surface processes and its application to snow hydrology, *Hydrological Processes: An International Journal*, 20(10), 2111–2128, 2006.
- Libbrecht, K. G., Diffusion limited growth, <http://www.snowcrystals.com>.
- Libbrecht, K. G., A critical look at ice crystal growth data, *arXiv preprint cond-mat/0411662*, 2004.
- Libbrecht, K. G., The physics of snow crystals, *Reports on Progress in Physics*, 68(4), 855–895, doi:10.1088/0034-4885/68/4/R03, 2005.
- Libbrecht, K. G., Modeling Diffusion-Limited Crystal Growth from Vapor using a Commercial Finite-Element Analysis Code, *arXiv:cond-mat/0610584*, 2006.
- Libbrecht, K. G., On the Equilibrium Shape of an Ice Crystal, *arXiv:1205.1452 [cond-mat]*, 2012.

- Libbrecht, K. G., Toward a comprehensive model of snow crystal growth: 5. measurements of changes in attachment kinetics from background gas interactions at -5 °C, *arXiv preprint arXiv:1602.08528*, 2016.
- Libbrecht, K. G., Physical Dynamics of Ice Crystal Growth, *Annual Review of Materials Research*, 47(1), 271–295, doi:10.1146/annurev-matsci-070616-124135, 2017.
- Libbrecht, K. G., and M. E. Rickerby, Measurements of surface attachment kinetics for faceted ice crystal growth, *Journal of Crystal Growth*, 377, 1–8, 2013.
- Libbrecht, K. G., and H. Yu, Crystal growth in the presence of surface melting: Supersaturation dependence of the growth of columnar ice crystals, *Journal of crystal growth*, 222(4), 822–831, 2001.
- Ludwig, W., P. Reischig, A. King, M. Herbig, E. M. Lauridsen, G. Johnson, T. J. Marrow, and J. Y. Buffière, Three-dimensional grain mapping by x-ray diffraction contrast tomography and the use of Friedel pairs in diffraction data analysis, *Review of Scientific Instruments*, 80(3), 033,905, doi:10.1063/1.3100200, 2009a.
- Ludwig, W., et al., New opportunities for 3D materials science of polycrystalline materials at the micrometre lengthscale by combined use of X-ray diffraction and X-ray imaging, *Materials Science and Engineering: A*, 524(1-2), 69–76, doi:10.1016/j.msea.2009.04.009, 2009b.
- Maeno, N., and T. Ebinuma, Pressure sintering of ice and its implication to the densification of snow at polar glaciers and ice sheets, *The Journal of Physical Chemistry*, 87(21), 4103–4110, 1983.
- Magono, C., and C. W. Lee, Meteorological classification of natural snow crystals, *Journal of the Faculty of Science, Hokkaido University. Series 7, Geophysics*, 2(4), 321–335, 1966.
- Marbouty, D., An experimental study of temperature-gradient metamorphism, *Journal of Glaciology*, 26(94), 303–312, 1980.
- Miller, D., and E. Adams, A microstructural dry-snow metamorphism model for kinetic crystal growth, *Journal of Glaciology*, 55(194), 1003–1011, 2009.
- Miller, D., E. Adams, and R. Brown, A microstructural approach to predict dry snow metamorphism in generalized thermal conditions, *Cold regions science and technology*, 37(3), 213–226, 2003.
- Mullins, W. W., and R. F. Sekerka, Stability of a planar interface during solidification of a dilute binary alloy, *Journal of applied physics*, 35(2), 444–451, 1964.

- Nagata, Y., T. Hama, E. H. G. Backus, M. Mezger, D. Bonn, M. Bonn, and G. Sazaki, The Surface of Ice under Equilibrium and Nonequilibrium Conditions, *Accounts of Chemical Research*, 52(4), 1006–1015, doi:10.1021/acs.accounts.8b00615, 2019.
- Nakaya, U., *Snow Crystals: Natural and Artificial*, Harvard University Press, 1954.
- Nakaya, U., Snow Crystals and Aerosols, *Journal of the Faculty of Science, Hokkaido University*, p. 17, 1955.
- Nelson, J., and C. Knight, Snow crystal habit changes explained by layer nucleation, *Journal of the atmospheric sciences*, 55(8), 1452–1465, 1998.
- Oura, K., M. Katayama, A. V. Zotov, V. G. Lifshits, and A. A. Saranin, Structural Defects at Surfaces, in *Surface Science: An Introduction*, edited by K. Oura, M. Katayama, A. V. Zotov, V. G. Lifshits, and A. A. Saranin, Advanced Texts in Physics, pp. 229–260, Springer Berlin Heidelberg, Berlin, Heidelberg, doi: 10.1007/978-3-662-05179-5_10, 2003.
- Palenstijn, W. J., K. J. Batenburg, and J. Sijbers, The ASTRA tomography toolbox, in *13th International Conference on Computational and Mathematical Methods in Science and Engineering, CMMSE*, vol. 2013, pp. 1139–1145, 2013.
- Palenstijn, W. J., J. Bédorf, and K. J. Batenburg, A distributed SIRT implementation for the ASTRA toolbox, *Proc. Fully Three-Dimensional Image Reconstruct. Radiol. Nucl. Med*, pp. 166–169, 2015.
- Pfeffer, W. T., and R. Mrugala, Temperature gradient and initial snow density as controlling factors in the formation and structure of hard depth hoar, *Journal of Glaciology*, 48(163), 485–494, 2002.
- Pinzer, B. R., and M. Schneebeli, Snow metamorphism under alternating temperature gradients: Morphology and recrystallization in surface snow, *Geophysical research letters*, 36(23), 2009.
- Pinzer, B. R., M. Schneebeli, and T. U. Kaempfer, Vapor flux and recrystallization during dry snow metamorphism under a steady temperature gradient as observed by time-lapse micro-tomography, *The Cryosphere*, 6(5), 1141–1155, 2012.
- Plapp, M., Phase-Field Models, in *Multiphase Microfluidics: The Diffuse Interface Model*, edited by R. Mauri, CISM Courses and Lectures, pp. 129–175, Springer Vienna, Vienna, doi:10.1007/978-3-7091-1227-4_4, 2012.
- Ramirez, J., C. Beckermann, A. Karma, and H.-J. Diepers, Phase-field modeling of binary alloy solidification with coupled heat and solute diffusion, *Physical Review E*, 69(5), 051,607, 2004.

- Reischig, P., A. King, L. Nervo, N. Viganó, Y. Guilhem, W. J. Palenstijn, K. J. Batenburg, M. Preuss, and W. Ludwig, Advances in X-ray diffraction contrast tomography: Flexibility in the setup geometry and application to multiphase materials, *Journal of Applied Crystallography*, *46*(2), 297–311, doi: 10.1107/S0021889813002604, 2013.
- Riche, F., M. Montagnat, and M. Schneebeli, Evolution of crystal orientation in snow during temperature gradient metamorphism, *Journal of Glaciology*, *59*(213), 47–55, 2013.
- Ridler, T. W., and S. Calvard, Picture thresholding using an iterative selection method, *IEEE transactions on Systems, Man and Cybernetics*, *8*(8), 630–632, 1978.
- Rolland du Roscoat, S., A. King, A. Philip, P. Reischig, W. Ludwig, F. Flin, and J. Meyssonier, Analysis of Snow Microstructure by Means of X-Ray Diffraction Contrast Tomography, *Advanced Engineering Materials*, *13*(3), 128–135, 2011.
- Sazaki, G., S. Zepeda, S. Nakatsubo, M. Yokomine, and Y. Furukawa, Quasi-liquid layers on ice crystal surfaces are made up of two different phases, *Proceedings of the National Academy of Sciences*, *109*(4), 1052–1055, 2012.
- Schneebeli, M., and S. A. Sokratov, Tomography of temperature gradient metamorphism of snow and associated changes in heat conductivity, *Hydrological Processes*, *18*(18), 3655–3665, 2004.
- Schweizer, J., J. B. Jamieson, and M. Schneebeli, Snow avalanche formation, *Reviews of Geophysics*, *41*(4), 2003.
- Sei, T., and T. Gonda, The growth mechanism and the habit change of ice crystals growing from the vapor phase, *Journal of Crystal Growth*, *94*(3), 697–707, 1989.
- Seligman, G., *Snow Structure and Ski Fields: Being an Account of Snow and Ice Forms Met with in Nature, and a Study on Avalanches and Snowcraft*, Macmillan and Company, limited, 1936.
- Shreve, R., Migration of air bubbles, vapor figures, and brine pockers in ice under a temperature gradient, *Journal of Geophysical Research*, *72*(16), 4093–4100, 1967.
- Slavov, V., and S. Dimova, Phase-field versus level set method for 2D dendritic growth, in *International Conference on Numerical Methods and Applications*, pp. 717–725, Springer, 2006.
- Sommerfeld, R. A., A branch grain theory of temperature gradient metamorphism in snow, *Journal of Geophysical Research: Oceans*, *88*(C2), 1484–1494, doi:10.1029/JC088iC02p01484, 1983.

- Srivastava, P. K., P. Mahajan, P. K. Satyawali, and V. Kumar, Observation of temperature gradient metamorphism in snow by X-ray computed microtomography: Measurement of microstructure parameters and simulation of linear elastic properties, *Annals of Glaciology*, 51(54), 73–82, doi:10.3189/172756410791386571, 2010.
- Staron, P. J., E. E. Adams, and D. A. Miller, Formation of Depth Hoar Resulting from Thermal Optimization of Snow Microstructure, in *International Snow Science Workshop. Anchorage, Alaska*, pp. 186–193, 2012.
- Staron, P. J., E. E. Adams, and D. A. Miller, Nonequilibrium thermodynamics of kinetic metamorphism in snow, *Cold Regions Science and Technology*, 97, 60–71, 2014.
- Stranski, I. N., Zur theorie des kristallwachstums, *Zeitschrift für physikalische Chemie*, 136(1), 259–278, 1928.
- Sturm, M., and J. B. Johnson, Thermal conductivity measurements of depth hoar, *Journal of Geophysical Research: Solid Earth*, 97(B2), 2129–2139, 1992.
- Takahashi, Y., and K. Fujino, Crystal orientation of fabrics in a snow pack, *Low Temp. Sci., Ser. A*, 34, 71–78, 1976.
- Uehara, T., and R. F. Sekerka, Phase field simulations of faceted growth for strong anisotropy of kinetic coefficient, *Journal of crystal growth*, 254(1-2), 251–261, 2003.
- Vionnet, V., E. Brun, S. Morin, A. Boone, S. Faroux, P. Le Moigne, E. Martin, and J. M. Willemet, *The Detailed Snowpack Scheme Crocus and Its Implementation in SURFEX v7. 2*, *Geosci. Model Dev.*, 5, 773–791, Doi: 10.5194, gmd-5-773-2012, 2012.
- Wang, X., and I. Baker, Observation of the microstructural evolution of snow under uniaxial compression using X-ray computed microtomography, *Journal of Geophysical Research: Atmospheres*, 118(22), 12,371–12,382, doi:10.1002/2013JD020352, 2013.
- Wang, X., and I. Baker, Evolution of the specific surface area of snow during high-temperature gradient metamorphism, *Journal of Geophysical Research: Atmospheres*, 119(24), 13,690–13,703, doi:10.1002/2014JD022131, 2014.
- Wiese, M., and M. Schneebeli, Snowbreeder 5: A Micro-CT device for measuring the snow-microstructure evolution under the simultaneous influence of a temperature gradient and compaction, *Journal of Glaciology*, 63(238), 355–360, 2017.

- Wilson, C. J. L., D. S. Russell-Head, K. Kunze, and G. Viola, The analysis of quartz c-axis fabrics using a modified optical microscope, *Journal of Microscopy*, 227(1), 30–41, doi:10.1111/j.1365-2818.2007.01784.x, 2007.
- Wulff, G., Zur frage der geschwindigkeit des wachsthums und der auflösung der krystallflächen, *Zeitschrift für Kristallographie-Crystalline Materials*, 34(1-6), 449–530, 1901.
- Yokoyama, E., and T. Kuroda, Pattern formation in growth of snow crystals occurring in the surface kinetic process and the diffusion process, *Physical Review A*, 41(4), 2038, 1990.
- Yosida, Z., et al., Physical Studies on Deposited Snow. I.; Thermal Properties., *Contributions from the Institute of Low Temperature Science*, 7, 19–74, 1955.

Résumé

L'objectif principal de la thèse est d'améliorer la compréhension des phénomènes de facettage observables lors des métamorphoses de la neige sèche. La thèse se concentre sur les couplages entre la cinétique de croissance cristalline et la diffusion de la vapeur et de la chaleur. Pour la première fois, la tomographie par contraste de diffraction (DCT) a été utilisée pour suivre l'évolution d'un échantillon de neige sous gradient de température contrôlé. La technique permet de mesurer l'orientation cristalline des grains constituant la microstructure de l'échantillon. Les relations entre l'orientation cristalline et les échanges de matière ont été analysés. L'étude montre que les différences de cinétique entre les faces basales et prismatiques des cristaux de glace influencent les flux de matière à l'interface air/glace. Sur le plan de la simulation numérique, une forte anisotropie du coefficient cinétique a été prise en compte dans l'évolution de l'interface air/glace. Le modèle développé utilise la méthode du champ de phase et couple le changement de phase à la diffusion de la vapeur et de la chaleur. Le modèle a été comparé d'une part à une expérience de migration d'une cavité d'air dans un monocristal de glace sous gradient de température, observée par microtomographie à rayons X et d'autre part, à la croissance d'un cristal négatif de glace lors d'une expérience de pompage suivie par microscopie optique. L'anisotropie prise en compte permet de reproduire le facettage observé. Enfin, le potentiel du modèle numérique proposé pour décrire les métamorphoses de la neige est mis en évidence.

Mots-clé: Neige, métamorphoses, croissance cristalline, coefficient cinétique, orientation cristalline, champs de phase, tomographie RX, DCT

Abstract

The main objective of the thesis is to improve our understanding of faceting occurring during dry snow metamorphism. The thesis focuses on the interplay between heat and mass diffusion, and kinetic effects in the context of snow. For the first time, Diffraction Contrast Tomography has been performed to monitor an experiment of temperature gradient metamorphism. The technique permits us retrieval of the crystalline orientation of the grains constituting the microstructure of the sample. Links between orientation of crystals and mass fluxes were analysed. The study shows that kinetic differences between basal and prismatic faces have effects on phase change fluxes at the ice/air interface. From a numerical modeling point of view, a highly anisotropic kinetic coefficient has been taken into account for the evolution of the ice/air interface. The model uses the phase-field approach and couples phase changes to heat and water vapor diffusion. The model was compared to an experiment of air cavity migration under a temperature gradient in a monocrystalline ice block monitored with X-ray microtomography, and to the growth of a negative crystal during a pumping experiment followed with optical microscopy. Such anisotropy permits us reproduction of the observed faceting. Finally, the potential of the proposed model to describe snow metamorphism is highlighted.

Keywords: Snow, metamorphism, crystal growth, kinetic coefficient, phase-field, crystalline orientation, X-rays tomography, DCT

